COMPOSITION AND STRUCTURE IN FLOCCULATED MINERAL SYSTEMS

by

Michael Ryan MacIver

B.Sc., The University of Western Ontario, 2006
M.A.Sc., The University of British Columbia, 2016

A THESIS SUBMITTED IN PARTIAL FULFILLMENT
OF THE REQUIREMENTS FOR THE DEGREE OF

DOCTOR OF PHILOSOPHY

in

THE FACULTY OF GRADUATE AND POSTDOCTORAL STUDIES
(Mining Engineering)

The University of British Columbia
(Vancouver)

December 2022

The following individuals certify that they have read, and recommend to the Faculty of Graduate and Postdoctoral Studies for acceptance, the thesis entitled:

COMPOSITION AND STRUCTURE IN FLOCCULATED MINERAL SYSTEMS

submitted by **Michael Ryan MacIver** in partial fulfillment of the requirements for the degree of **DOCTOR OF PHILOSOPHY** in **Mining Engineering**.

Examining Committee:

Marek Pawlik, Professor, Mining Engineering, UBC
Supervisor

Sanja Miskovic, Assistant Professor, Mining Engineering, UBC
Supervisory Committee Member

Ian Frigaard, Professor, Departments of Mechanical Engineering & Mathematics, UBC
Supervisory Committee Member

Dharma Wijewickreme, Professor, Geotechnical Engineering, UBC
University Examiner

Scott Dunbar, Professor, Mining Engineering, UBC
University Examiner

Abstract

An investigation of model quartz floc structure and composition was made using X-ray computed tomography to understand how floc breakage could contribute to consolidation in the dewatering process.

It was concluded that floc macro-structure, defined by the connectivity and arrangement of sub-units in medium- and large-sized flocs plays an important role in the formation and breakage of flocs. Sub-units in flocs were found to be connected by lower solids concentration regions and the shared surface area between sub-units was found to decrease as a function of distance from the floc centroid. These observations indicated a tendency for flocs to break in a large-scale deformation mode (i.e. rupture along sub-unit boundaries), rather than smaller-scale fragmentation or attrition.

From compression tests evaluated with CT scans and correlated with the gravimetric method, it was found that negligible changes in the solids concentration of flocs occurred at low applied pressures ($<$ 3 kPa), which indicated that dewatering at lower applied pressures was dominated by breakage and removal of intra-aggregate fluid. These observations support the proposed model that floc breakage and re-organization of the sediment packing structure plays an important role in the thickening process.

This research demonstrated two different methods of calibrating computed tomography (CT) images for solids concentration: using watery mineral suspensions of varying solids concentration for micro-CT images; and using air, water, and solid quartz for calibration of synchrotron-source CT. In Appendix A, the interpretation of X-ray CT data in a multiphase system was considered

using phosphate particles. In that case, calibration of the X-ray signal was achieved by identifying the apatite phase using correlative tomography, followed by calibration of the apatite phase mineral concentration using standards of varying apatite content.

Lay Summary

In mineral processing, it is necessary to crush and grind ore in preparation for the extraction or separation of the target mineral. Often, water is added to the ground ore to form a slurry that is sent downstream for separation or extraction processes. At the end of many of these processes, however, it is necessary to remove the water from the waste or product streams, to recycle the water and convert the slurry into a manageable, high-solids content form. Flocculation is a key chemical treatment in the dewatering process which causes the fine particles of a slurry to collect into small clusters called flocs. Compression and mixing of the flocs causes further dewatering, but there is no explanation about what happens to the flocs on a microstructural scale during this stage of the dewatering process. This research developed an approach to analyzing 3D X-ray images of flocs and sediments to provide new insights into how floc structure and composition change during the dewatering process.

Preface

This dissertation is based on experimental work that was designed by me with the input of my research supervisor, Dr. Marek Pawlik. The body of this thesis has been published or presented as follows.

Parts of Chapter 2 and Chapter 3 were published as: [M.R. MacIver] and M. Pawlik (2022), A floc structure perspective on sediment consolidation in thickened tailings, Chem. Eng. Sci., vol. 263, p. 118095. I wrote and revised the manuscript, M. Pawlik edited and revised the manuscript.

A version of Chapter 3 has been published as: [M.R. MacIver], M. Pawlik, and H. Hamza (2019), Aggregate density changes during the compression of flocculated silica. Powder Technol. vol. 350, pp. 43–50. I conceived this study with co-author M. Pawlik. I conducted the experimental design, data collection, analysis, and prepared the manuscript. Fabrication of research apparatus was conducted with the assistance of Mr. Aaron Hope. Co-author H. Hamza (a collaborator from an industrial research partner) reviewed the final manuscript.

A part of Chapter 3 was included in a conference proceedings as: [M.R. MacIver], M. Pawlik, H. Hamza, H., and L. Malin (2018). Networked structure analysis with micro-CT method. 30th International Mineral Processing Congress Proceedings. Moscow, Russia. Co-authors M. Pawlik and H. Hamza reviewed and approved the submission, respectively.

A version of Chapter 4 was published as: [M. R. MacIver], H. Alizadeh, V. K. Kuppusamy, H. Hamza, and M. Pawlik, The macro-structure of quartz flocs, Powder Technol., vol. 395, pp. 255–266, 2022. I conceived the research design with M. Pawlik. I conducted the data collection, designed the image analysis software, conducted the formal analysis, and prepared the manuscript.

Co-authors H. Alizadeh and V.K. Kuppusamy contributed to X-ray image data collection and reviewed the journal manuscript.

A version of Chapter 6 was presented as an extended abstract: M.R. MacIver, M. Pawlik, and C. Chassagne, Floc volume estimates from 2D compared with 3D in Proceedings of the 60th Conference of Metallurgists, COM 2021: The Canadian Institute of Mining, Metallurgy and Petroleum. Co-authors M. Pawlik and C. Chassagne contributed to reviewing the extended abstract.

A version of Chapter 6 was prepared for submission to an academic journal. I conceived of this research, collected the X-ray image data, designed the video analysis software, conducted the formal analysis, and prepared the journal manuscript. Co-author A. Shakeel contributed by collecting floc settling videos and reviewing the manuscript. C. Chassagne and M. Pawlik contributed to the research concept and reviewed the manuscript.

A version of Appendix A was published as: [M. R. MacIver], A. Sablok, and M. Pawlik, Apatite content and distribution in organic-rich particles, Miner. Eng., vol. 170, p. 107049, 2021. I conceived of this research with co-author M. Pawlik. I designed the experimental program, designed the image analysis software, completed the formal analysis, and prepared the manuscript. Co-author A. Sablok contributed to image data collection. Co-author M. Pawlik reviewed and revised the manuscript.

Part of Appendix A was presented at a conference and included in the proceedings as: [M. R. MacIver] and P. Pawlik, Correlative tomography for 3D multi-phase structure in a phosphate ore, in MineXchange 2020 SME Annual Conference and Expo, 2020. I prepared the paper and revised it with co-author M. Pawlik.

Table of Contents

List of Tables

List of Figures

Abbreviations

APAM anionic polyacrylamide

BFE binary image fraction error

CLSM confocal laser scanning microscopy

CPAM cationic polyacrylamide

CR compressive rheology

CT computed tomography

FIB focused ion beam (tomography)

FOV field of view

HCP hexagonal close packing

HU Hounsfeld Units

LIN linear packing structure

MBWT marker-based watershed transform

MSSE mean structural image similarity error

NIST National Institute of Standards and Technology

RMSE root mean square error

SE structuring element

SEM scanning electron microscopy

SEM-EDX scanning electron microscopy with energy dispersive X-ray

SLS solid-liquid separation

TEM transmission electron microscopy

Symbols

A_2	Area [μm^2]
$A_{3,s}$	Floc surface area [μm^2]
A_i	Area of phase i [μm^2]
A_{int}	Internal shared surface area [μm^2]
AR	Aspect ratio [$-$]
B_T	Target binary image
B_S	Source binary image
C	Image similarity cost function
C_i	Concentration of phase i [g/cm^3]
c_i	Centroid of object i [$-$]
D	Diameter ratio [$-$]
d_{50}	particle size, 50 % passing [μm]
d_{90}	particle size, 90 % passing [μm]
d_{agg}	aggregate diameter
$D_{bc,2}$	Box counting dimension, 2D [$-$]
$D_{bc,3}$	Box counting dimension, 3D [$-$]
D_f	Fractal dimension [$-$]
d_I	Box size in box counting [μm]
$D_{lav,2}$	Perimeter-area fractal dimension, 2D [$-$]
$D_{lav,3}$	Perimeter-area fractal dimension, 3D [$-$]

d_{mean}	Mean floc size [μm]
d_{rms}	Root-mean-square distance [μm]
E_a	Apparent micro-computed tomography energy [keV]
H	Intersection of B_T and B_S
I	Energy intensity of transmitted photons [keV]
I_0	Energy intensity of incident photons [keV]
I_S	Source grayscale image
I_T	Target grayscale image
k_{a}	Structure pre-factor [$-$]
L	Linear size of fractal objects [$-$]
L_{p}	Linear size of primary particles [$-$]
M	Affine transform
N	Number of particles or objects
P_{a}	Applied pressure [kPa]
P_{i}	Perimeter of phase i [μm^2]
r_0	Radius
t_i	Translation along axis i [μm]
V_{i}	Volume of phase i [μm^3]
w_{i}	Mass fraction of phase i [$-$]
$\delta_b(X_i)$	Morphological binary image dilation
ε	Porosity
ζ	Structural packing factor
θ_i	Angle of rotation about axis i [$^\circ$]
μ_{i}	Linear attenuation coefficient of phase i [cm^{-1}]
$\mu_{\text{i}}/\rho_{\text{m}}$	Mass attenuation coefficient [cm^2/g]
μ_{v}	Dynamic viscosity of water [Pas]
ξ	Shape factor

ξ_2	Shape factor, 2D
ρ_f	Mass density of floc [g/cm^3]
ρ_m	Mass density [g/cm^3]
ρ_w	Mass density of water [g/cm^3]
ϕ, ϕ_s	Average solids volume fraction [−]
ϕ_g	Gel point [−]
ϕ_i	Solids volume fraction of phase i [−]
φ_cp	Close-packing fraction limit of flocs [−]
φ_i	Volume fraction of phase i [−]
X_i	Set of indices in image of component i

Acknowledgements

I am grateful for the deep and multi-faceted support of Dr. Marek Pawlik. His sustained interest and guidance in this work were critical to the outcome.

Thank you to Sally Finora for introducing me to the lab several years ago and showing me more than one way to clean glassware. Mr. Aaron Hope's contributions to at least three prototypes were priceless. Thank you to Dr. Claire Chassagne of TU Delft for hosting me in her lab for a term.

The assistance and company of Vinoth Kumar Kuppusamy, Han Baisui, and Hamid Alizadeh during two field trips to Canadian Light Source (CLS) in Saskatchewan were much appreciated. The technical support of Sergei Gasilov from CLS during proposal writing and while on site were helpful.

The support of Richard Pilon from Albatross Environmental LTD and Hassan Hamza from BC Research LTD are appreciated. Both companies provided funding for this work over multiple years through MITACS Accelerate Internships. Support by Natural Sciences and Engineering Research Council through a CGS-D scholarship and a Michael Smith Foreign Study Supplement is gratefully acknowledged.

Sophie, my partner, suggested that I start a PhD. Much later, she also suggested that I finish the PhD. Her support through the middle was unwavering. Our two daughters are a continuous source of inspiration and happiness.

Chapter 1

Introduction

It has been observed that an improved understanding of the link between microscopic material properties and macroscopic fluid transport properties is a key barrier to the improvement of dewatering technologies (Wang et al., 2014). While flocculation is widely used as a pre-treatment in solid liquid separation processes (e.g. for gravitational settling, thickening, filtration, and centrifugation), and the principles for design and operation of the flocculation process are well known, limited knowledge is available about the micro-scale processes that govern the response of flocculated sediments to dewatering processes. For example, models and empirical test work exist to predict and describe the thickening process (Lester et al., 2005), but these lab-scale tests have been shown to underestimate the performance of a real thickener by almost two orders of magnitude (Usher and Scales, 2005). To account for this discrepancy, aggregate density and size factors have been added to the unified theory of thickening (Usher et al., 2009) and a modified-Kynch settling model (van Deventer et al., 2011) to infer changes in aggregate structure as a result of the densification process. While these adjustment factors have been shown to improve the modelling of large scale thickening processes (Spehar et al., 2015), the physical validity of these parameters has not been confirmed through direct measurement of changes in aggregate structure.

1.1 Problem statement

X-ray computed tomography (CT) images can provide powerful insights into the structure and composition of flocculated mineral sediments. CT instrumentation has developed at a rapid pace in recent years with improvements in scan acquisition time, field-of-view size, and spatial and linear attenuation resolution. Yet, the application of X-ray CT to the quantitative study of fine particulate systems has been limited by the software tools available for analysis of the 3D images that CT produces. Currently available software tools include general image analysis frameworks and closed-source commercial software packages. Any specialized analysis of structure or composition beyond the stock algorithms available in such software requires detailed knowledge of computer programming. A further hindrance to quantitative analysis of CT images of particulate mineral systems is the absence of pre-existing calibration standards. X-ray CT can be used to generate 3D models of physical structures, but there is no explicit chemical or mineral information in a CT dataset. Without calibration, chemical or mineral composition information cannot be obtained.

1.2 Research objectives

The high-level objective of this thesis was to demonstrate a quantitative approach to the analysis of 3D CT images to obtain floc structure and composition information.

The sub-objectives of this thesis were to:

1. Develop and apply CT calibration methods suitable for particulate mineral systems.

2. Determine which sediment bed consolidation mechanisms are most significant during low-pressure dewatering of flocculated sediment beds

3. Relate properties measured from flocculated sediments by CT data to traditional dewatering property measurements and models of the thickening process.

1.3 Thesis outline

The remainder of the body of this thesis comprises a background section and three studies. The studies are related to each other and to the objectives described in Section 1.2 as follows.

Chapters 3 and 4 address the first sub-objective listed in Section 1.2. A different approach to CT calibration was taken in each study. In Chapter 3, a novel formulation of dilute, watery standards of varying quartz content was described for the calibration of a micro-CT instrument. Chapter 4 describes the use of a three point calibration and comparison to literature attenuation values for synchrotron-source CT. Appendix A describes the use of X-ray CT to obtain quantitative composition information in a multi-phase system. Two calibration steps were applied in that case study of low-grade apatite-containing particles. First, an image registration step was applied by quantitatively aligning scanning electron microscopy (SEM) and CT images obtained on the same volume in the sample. This allowed the phosphate-bearing regions in the samples to be identified. Then, a calibration for hydroxyapatite content of the phosphate-bearing region was applied to permit a full determination of the apatite distribution in the samples.

Chapters 3 and 4 relate to the second and third sub-objectives listed in Section 1.2. In Chapter 3, micro-CT was used to study the response of flocculated sediment beds (quartz flocs) to various levels of applied pressure. In the low applied pressure range ($\leq$ 75 kPa), it was deduced from relative changes in the floc solids volume fraction, $\phi_{\text{agg.}}$, and floc volume fraction, $\varphi_{\text{agg.}}$, that increases in the average bed solids volume fraction, ϕ, are caused by the removal of inter-floc water rather than densification of the flocs themselves. Chapter 4 provided a detailed account of the macro-structure of flocs. In that study, an image analysis method was developed to discern the sub-units that comprise the top-level or macro-structure of the flocs. It was suggested that breakage and re-organization of the floc macro-structure may occur during low applied pressure compressive dewatering. If the floc sub-units (or fragments) are packed into a smaller volume, then an increase in the bed ϕ may be achieved by a decrease in inter-floc water and a consequent increase of $\varphi_{\text{agg.}}$.

Chapter 5 addresses sub-objective three. Information about floc structure from the CT results in Chapters 3 and 4, along with some additional analysis, were compared with a popular mechanism

used to explain shear-enhanced dewatering in the literature. It was deduced that breakage and re-organization of the flocs and sediment bed could play a dominant role in the consolidation process in the shear zone of a thickener, based on the macro-floc structure and how the sediment bed structure changed as a function of applied pressure.

Chapter 6 compares the estimation of floc volume from 2D and 3D images. That chapter contributes to the third objective of this thesis because it provides an understanding of the limitations of the widely used settling column test for estimating floc volume.

In Appendix A, the application of X-ray CT in a multi-phase system is described using phosphate ore particles as an example. That section highlights how multiple sources of information can be combined with CT images to obtain a detailed description of the location and variation of the mineral content in a sample.

Chapter 2

Background

Flocculation is the combination of small solid particles from an aqueous suspension into larger solid-fluid aggregates called flocs. Flocculation is applied in the mineral, chemical, food, and agricultural industries in the solid-liquid separation (SLS) process, often as a pre-treatment, to improve the settling rate and permeability of fine particulate suspensions. In the thickening process, flocs are formed in a feed-well then permitted to settle and form a sediment bed, as shown in Figure 2.1. The key properties that determine the rate and extent of SLS in the sediment bed are the viscous drag and network stress that develop in the sediment bed (Buscall and White, 1987). For example, in a high-throughput operation, the sediment bed permeability may limit the fluid up-flow; while in a lower throughput operation, the network strength may limit the solids concentration achieved in the underflow (Usher and Scales, 2005). Yet the structural changes in the sediment that contribute to consolidation during thickening, especially in the low applied shear and compression regimes, are poorly understood. This means that the link between the micro-scale properties of the sediment and its macro-scale dewatering response is missing, and this is a major barrier to the development of a robust and physically-based model of the thickening process.

This thesis suggests, based on direct measurements of floc structure using X-ray CT images, that the breakage of floc macro-structure may contribute significantly to sediment bed consolidation, including during breakage and re-organization of the bed structure in the thickening process.

The link between small-scale lab studies of flocs in a compression cell and the zone of interest in a full-scale thickener is indicated in Figure 2.1. A background in several topics related to most or all of the studies conducted for this thesis include a brief explanation of: the role of flocculation in mineral processing, the sediment consolidation process, the role of imaging technology in floc structure research, and X-ray CT theory and calibration.

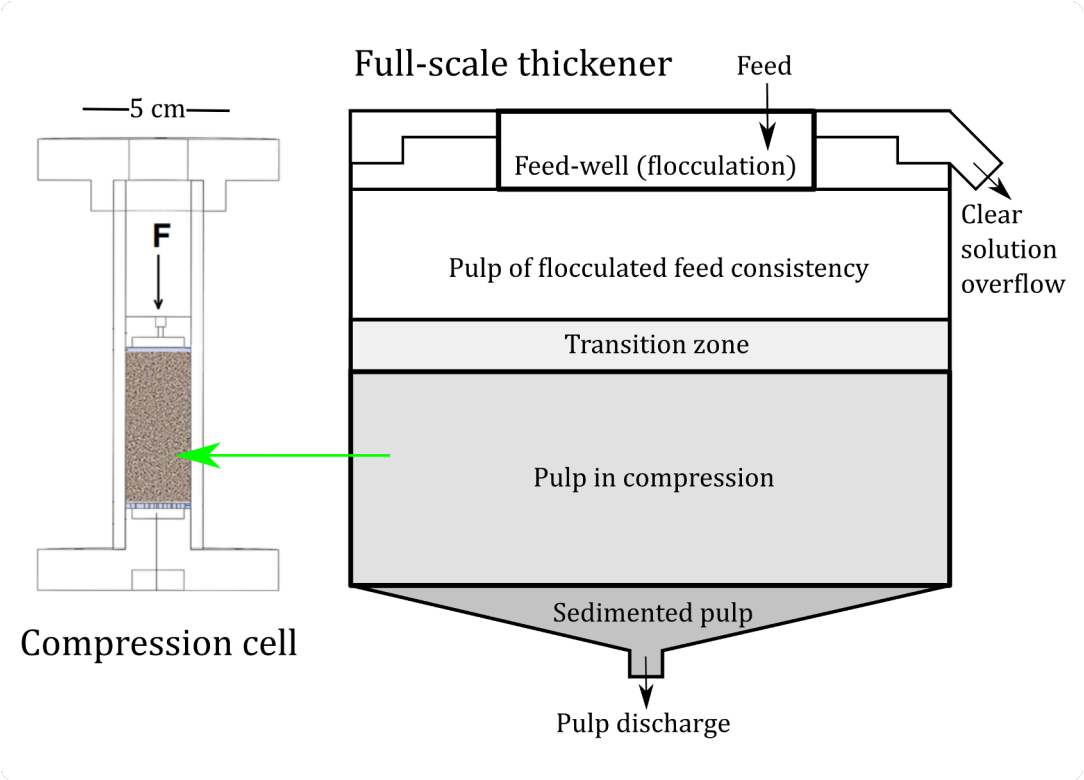

Figure 2.1: Schematic of a thickener, adapted from Concha (2013), and compression cell to indicate the relation between compression testing of flocculated sediment beds and a thickener compression zone.

2.1 Flocs in mineral processing

While this thesis focuses on floc structure and its role in the thickening process, it is worthwhile to consider the necessity and broader context of flocculation. In mineral processing, ore is crushed and ground to liberate the target mineral for downstream treatment. Separation processes, including size classification, gravity, flotation, and leaching circuits are typically carried out with the fine particulate solids in water, referred to as a suspension or slurry. The concentrate and tailings

streams of these processes are also in the form of a suspension, which must often be dewatered to meet the process requirements. Dewatering allows water to be recovered from waste streams or it may be an intermediate step toward increasing the solids content of a final product. A variety of dewatering equipment and processes exist, although final dewatering is typically assisted by sedimentation and/or filtration (Hogg, 2000).

2.1.1 Flocculation

Sedimentation will naturally increase the solids concentration at the lower portion of a suspension by the deposition of solid particles under the force of gravity. However, particulate suspensions may settle slowly due to small particle size ($< 10\ \mu$m) and inter-particle repulsion. Additionally, in mineral processing, the sediment thus formed is often difficult to pump, filter, or wash. For these reasons, flocculation may be applied as a pre-treatment to improve the settling rate (by aggregation of fine particles) and filterability (by improved porosity and permeability) of the sediment for onward processes, such that SLS will not be the rate limiting step in the mineral processing plant.

To induce flocculation in a slow-settling suspension, it is necessary that the inter-particle repulsion is reduced. Destabilization of the suspension may be achieved in some cases, depending on the composition of the suspension, by modification of the pH, addition of an electrolyte, or by addition of a chemical coagulant. Most often in mineral processing, though, flocculation is achieved by the addition of a high molecular weight polymeric flocculant while mixing the suspension. Outside of mineral processing, it should be noted that flocculation is a general term used to describe the accumulation of fine solid particles of almost any type into flocs. The widely accepted view is that natural polymers may associate with mineral surfaces either through adsorption on the solid mineral surface or through an acid-base type interaction (Liu et al., 2000), which reduces the inter-particle repulsion and joins particles into clusters. After flocculation, other treatment steps may be required to form and consolidate the sediment, such as settling, thickening, filtering, pumping, storage, or drying.

2.1.2 Floc structure

Floc formation is a dynamic process of growth and breakage (Klimpel and Hogg, 1991; Gorczyca, 2000) that produces a porous, irregular structure (Jarvis et al., 2005b) with three identifiable levels (Klimpel and Hogg, 1986). With reference to Figure 2.2, flocs produced by polymeric flocculation may range in size from a few microns to over one millimetre. During flocculation, the primary particles of a suspension aggregate to form small clusters called flocculi (Gorczyca, 2000) or floc nuclei. These flocculi aggregate to form micro-flocs, which may then aggregate to form a macro-floc (Klimpel and Hogg, 1991).

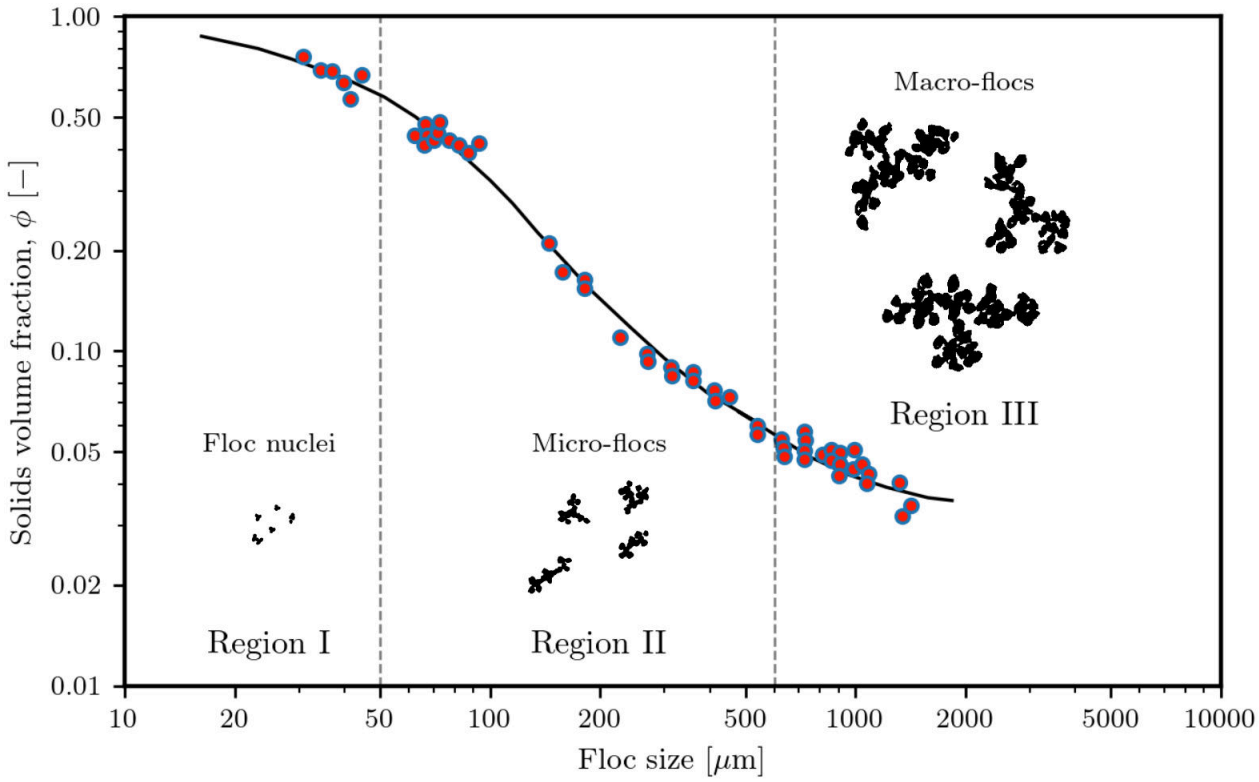

Figure 2.2: Change in floc solids concentration as a function of floc size to demonstrate the multi-level structure of flocs with data from (Klimpel and Hogg, 1986) (vertical bars and floc illustrations added by the author.)

Aggregates produced by the first two stages of growth (flocculi and micro-flocs) are held together by strong (surface) forces, while larger macro-flocs are mostly held together by mechanical entanglement (Vold, 1963). Franks and Zhou (2010) concluded based on atomic force microscopy

measurements that the inter-particle adhesion force played a primary role in floc strength in flocculi and micro-flocs. For macro-flocs, a more open floc structure will have fewer bonds that need to be broken; while more force is required to cause breakage in compact structures with a higher coordination number of sub-units and primary particles within flocs. As a result, macro-flocs are quite weak and they tend to break preferentially at points of contact between the smaller, denser micro-flocs (Klimpel and Hogg, 1986; Eisma et al., 1990) by two main mechanisms: large scale fragmentation (due to tensile stress) and surface erosion (due to shear stress) (Jarvis et al., 2005a).

Evidence for the multi-level structure of flocs has been obtained through empirical experiments and image analysis. Klimpel and Hogg (1986) deduced a multi-level floc structure from the data in Figure 2.2, which shows three distinct slopes on a plot of floc solids volume fraction, ϕ_s (determined by applying Stokes' Law to size-velocity data from settling experiments), versus floc size in polymer-flocculated quartz aggregates. At small floc sizes (< 50 μm), the ϕ_s-size slope was lower because the addition of primary particles to tight clusters causes a negligible change in floc size and density. At intermediate floc sizes (between 50 μm and 600 μm) the ϕ_s-size slope was larger because the aggregation of flocculi, at decreased packing efficiency, leads to a rapid increase in floc size and decreasing density. Above 600 μm, the ϕ_s-size slope levels off, which indicates that floc density is constant as a function of size, because growth by addition of more micro-flocs does not significantly alter the macro-floc density.

By applying varying amounts of mixing energy to sludge flocs, followed by measuring floc porosity using image analysis, Gorczyca and Ganczarczyk (1999) found that the sludge flocs contained three levels of structure based on the different size, density, resistance to shear, and porosity at each sub-level. Similarly, Snidaro et al. (1997) found that successive sonication of flocs produced sub-populations of different sizes starting with 125 μm macro-flocs, 13 μm micro-flocs and down to the 2.5 μm size of the primary particles.

Sharma et al. (2017) used SEM and X-ray CT to show that tightly packed nano- and micro-scale aggregates of clay particles were associated into clusters in the SEM images; while larger scale aggregates – presumably macro-flocs due to their millimetre size scale – were observable in the X-

ray CT images. Such changes in compactness at different structural levels was also demonstrated using 3D confocal laser scanning microscopy (CLSM) to study the effect of mixing on floc structure (Govedarica et al., 2020). Most recently, a multi-scale imaging approach was developed by Wheatland et al. (2020), using X-ray CT, 2D SEM, 3D focused ion beam (tomography) (FIB), and transmission electron microscopy (TEM), to permit the complete visualization of the multi-level floc structure, from the nano- to millimetre scale.

Whereas qualitative and quantitative analyses of primary and secondary floc structure have been carried out in the literature, there does not appear to be any attempt to identify and quantify the macro-structure of flocs.

2.2 Mechanisms of sediment consolidation

The main objective in dewatering is to separate the liquid from the solids, thereby producing a volume of relatively clear fluid and a volume of suspension with increased solids content. The solids volume fraction, ϕ, of a region of interest in a sample may be defined as

$$\phi = \frac{V_s}{V_t}, \tag{2.1}$$

where V_s is the volume of solids and V_t is the reference volume. For reference, in a fine tailings thickening process, the feed may be on the order of ϕ = 0.02 to 0.05 (approximately 5.22 to 12.4 wt. % with ρ_s=2.7 g/cm^3). However, the feed is often diluted in the feed-well before flocculation occurs. Although flocculation and settling cause a rapid increase in ϕ by aggregation, settlement, and sediment bed formation, further consolidation is usually required.

In this thesis, the relative changes in the average ϕ of the sediment bed and the ϕ of the flocs are investigated, so it is necessary to distinguish between these two properties. For the sediment bed, the symbol ϕ_s will be used to indicate that V_t includes the solids in the flocculated material, and the fluid between and inside the flocs in the sediment bed. For flocs, the symbol ϕ_{agg} will be used to indicate that V_t is the floc volume. A detailed discussion on how the choice of floc volume impacts the ϕ_{agg} is given in Chapter 6. The relative values of ϕ_s and ϕ_{agg} are related through (Usher

et al., 2009),

$$\phi_s = \phi_{agg}\varphi_{agg}, \tag{2.2}$$

where φ_{agg} is the aggregate volume fraction in the sediment bed. In a flocculated suspension, the solids are predominantly contained in the volume fraction occupied by the aggregates, φ_{agg}, at a solids concentration of ϕ_{agg}, so the average solids volume fraction of the suspension, ϕ_s, can be determined with Equation 2.2.

Equation 2.2 indicates that sediment consolidation (increased ϕ_s) may be caused by two main pathways: an increase in the aggregate solids volume fraction, ϕ_{agg}, or by an increase in the aggregate volume fraction, φ_{agg} (i.e. by the expulsion of intra-aggregate fluid). While this description is relatively simplistic, it may be surprising how little is known about the sediment consolidation process on the microscopic level in a flocculated sediment bed. Studies have focused on the impact of the pore network structure on sediment bed permeability (Jiao et al., 2021) and demonstrated the ability to simulate fluid flow on flocculated sediment structures (Selomulya et al., 2005). A very recent study showed how dewatering affects filter cake structure, but only examined the final structure produced using X-ray CT (Löwer et al., 2021). Other recent studies have given insights into floc structure, including a correlative tomography approach (Spencer et al., 2021), the measurement of moisture content in flocs (Sharma et al., 2017), and the effect of changing pH and applied polymer dosage on characteristic floc size (Dong et al., 2018). However, such studies have not been used to help explain the consolidation processes within flocculated sediments.

The compressive rheology (CR) model combines a theoretical model of sedimentation and consolidation with empirical dewatering parameter measurements (Buscall and White, 1987; Landman and White, 1994) to permit modelling and estimation of dewatering design parameters (Stickland and Buscall, 2009). Examples include steady-state (Usher and Scales, 2005) and time-dependent models of thickening (Zhang et al., 2013a). A desirable feature of this approach is that the physically-based theoretical model is parameterized by laboratory measurements of the system under study, making it amenable to engineering approaches that include test work on the mate-

rial and conditions at the laboratory scale. Historically, CR treated flocculated suspensions as a continuous medium (Concha, 2013), rather than comprised of distinct fluid and flocculated solids phases. As such, no properties of the aggregates were included in the models. A notable drawback of earlier CR models was that they underestimated the actual throughput of full-scale thickeners by several orders of magnitude in some cases (van Deventer et al., 2011). Many factors contribute to the discrepancies between full-scale thickener performance and the predictions based on lab tests. Floc, and hence sediment bed, structure is affected by particle size and type, flocculant dosage and type, aqueous chemistry, and the hydrodynamic conditions in the flocculation feed-well (Scales et al., 2012). In addition to rake shear, shear is also imparted by the sloped thickener base.

To account for the discrepancy between the modelled and actual sediment consolidation, a modified version of the CR model has been developed which assumes that aggregate densification takes place in the sediment. This is accounted for by the inclusion of parameters to describe the flocculated phase, including floc size, ϕ_{agg} and φ_{agg}, in the CR model. Aggregate densification is an increase in ϕ_{s} caused by an increase in the aggregate solids volume fraction, ϕ_{agg}, from the original value, $\phi_{\text{agg,0}}$, by the expulsion of fluid from the aggregates (Zhang et al., 2013b). An explanation given for aggregate densification is that the development of local pressure gradients in the shear zone of a thickener cause the water to be essentially massaged out of the flocs (Gladman et al., 2005). The modified CR model assumes that the aggregates are spherical and of equal size, so a decrease in aggregate size by densification causes an increase ϕ_{agg} by the following proportionality (Usher et al., 2009):

$$\phi_{\text{agg}} = \phi_{\text{agg,0}} \frac{d_{\text{agg,0}}^3}{d_{\text{agg}}^3}, \tag{2.3}$$

where $\phi_{\text{agg,0}}$ is the solids volume content of the aggregate before densification, $d_{\text{agg,0}}$ is the initial aggregate diameter, and d_{agg} is the aggregate diameter after densification. Densification increases the gel point, ϕ_{g} (i.e. the ϕ_{s} value at which a touching network of particles is formed), because the aggregates have a higher solids content (i.e. increased ϕ_{agg}), but φ_{agg} is assumed to be constant. Traditionally, the gel point was defined in terms of ϕ_{s} because the φ_{agg} and ϕ_{agg} parameters were

not available.

Justification of the aggregate densification mechanism seems to be based primarily on two literature sources: Mills et al. (1991) and Farrow et al. (2000). Mills et al. (1991) showed that coagulated latex particle networks re-arranged to form discrete, tightly packed aggregates in response to applied shear. However, the sediment in Mills et al. was initially a space-filling structure connected by interacting chains formed by diffusion-limited cluster-cluster aggregation. Those researchers stated that application of shear to the initial structure produced an "equilibrium form" of the sediment, which suggests that the energy input from applied shear enabled the hydrophobic latex particles to re-organize and reduce the surface area exposed to water. As such, the observations of aggregate densification in Mills et al. are based on hydrophobic surface interactions and should perhaps not be applied to flocs formed by polymer-bridging or electrostatic patch reduction.

Although flocs formed by coagulant and polymer flocculant demonstrate varying degrees of restructuring and re-growth (Yukselen and Gregory, 2004), the evidence for increased floc density as a result of applied shear is inconclusive. Hogg suggested that certain types of floc structures could be subject to "compaction" (Hogg, 2000) under shear, a term which suggests increased density or concentration. However, Hogg's observation was that open, extended structures of polymer-flocculated aggregates were prone to re-structuring. Perhaps a better term could have been "more compact structure" rather than "compaction." A more compact structure, rather, is produced by a re-arrangement of sub-units of the same ϕ_{agg} into a smaller volume produces an apparently higher average ϕ_s. Likewise, a more compact structure would be expected to experience less drag while settling, which would result in a higher settling velocity and calculated floc density from settling column experiments.

To illustrate the effect of restructuring on ϕ_{agg}, φ_{agg} and ϕ_s, the two theoretical floc structures in Figure 2.3 were generated by re-arranging the same set of primary shapes into extended and compact, non-overlapping, structures. It was assumed that the solids concentration of each fragment is 0.1. This simple example shows that the choice of enclosing volume has a significant effect on the floc solids volume fraction and that floc restructuring can produce an apparent increase in solids

volume fraction when the chosen volume is based on an external diameter.

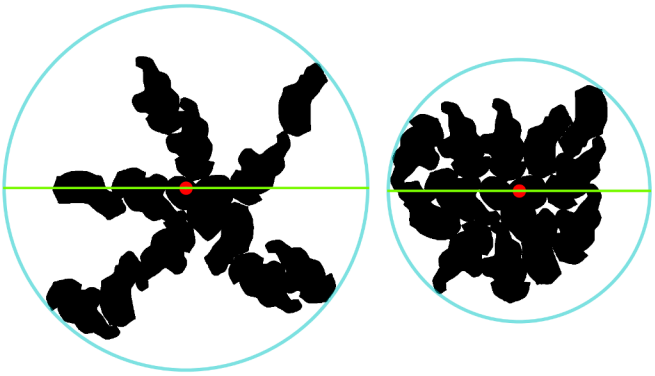

	Extended floc	Compact floc
occupied floc area [μm^2]	14140.0	14140.0
ϕ_{agg}	0.10	0.10
φ_{agg}	0.29	0.56
Ferret diameter [μm]	250.0	179.5
ϕ_s	0.029	0.056

Figure 2.3: Illustration that compares the effective ϕ_s value in extended and compact flocs when the Ferret diameter was used to calculate effective floc area.

In Figure 2.3, the aggregate solids volume fraction (ϕ_{agg}=0.1) and the occupied area (14140 μm^2, black regions) is the same for both flocs. If the image is assumed to be 1 μm thick, then the volume that encloses the region of the image occupied by solid material (total occupied volume) and solids in each floc are also the same. However, if an external diameter, such as principle axis length or Ferret's diameter is used to measure floc volume, the enclosing volume of the two flocs will differ. As such, the actual flocculated material will only occupy part of the calculated volume, designated by φ_{agg} in Figure 2.3. When the ϕ_s (average) value of the enclosed region is calculated according to Equation 2.2, the ϕ_s value of the extended floc (0.029) is almost one half of the compact floc value (0.056). Note that elsewhere in this paper, the average ϕ_s value refers to the average sediment bed solids volume fraction.

Farrow et al. (2000) studied the effect of shear on suspension consolidation in pilot- and full-

scale thickeners. Effective floc density was measured using the settling speed and size of flocs with an image analysis method (floc density analyzer) and converted to ϕ_{agg} here for consistency. Floc density measurements indicated an increase of ϕ_{agg}=0.02 to 0.03, before and after shear on the pilot scale, respectively, while in a full-scale thickener, an increase of ϕ_{agg}=0.04 to 0.147 was recorded from floc feed-well samples and the underflow, respectively. While these results indicate an increase in effective floc density, an alternative interpretation is that applied shear has produced more compact structures (as described in the paragraph above), such that they experience less drag, which would raise their effective density measured in settling velocity experiments.

The effective density of individual flocs, ρ_{eff} [g/cm^3], can be calculated from Stokes' Law if the floc diameter, d_{agg} [cm], and settling velocity, v [cm/s], are known from experiment (Nasser, 2014):

$$\rho_{eff} = \rho_f - \rho_w = \frac{3v^2 C_D \rho_w}{4g d_{agg}} \tag{2.4}$$

where ρ_f [g/cm^3] and ρ_w [g/cm^3] are the mass density of the floc and fluid phase, g is the gravitational constant, and C_D is the drag coefficient. It has been shown that flocs usually have $R_e < 10^6$ and sphericity of around 0.8, so C_D can be set to $45/R_e$, although alternate models may be used. From Equation 2.4, it is expected that floc density decreases with increased floc size. Furthermore, there are several variants of Equation 2.4 that use alternative drag coefficients or use fractal dimension model to model the effective density-size scaling relationship (Winterwerp, 2002). Nonetheless, Lee and Kramer (2004) have shown that the apparent trend of decreased density with increased size is an effect of the drag coefficient expression used.

The two structures in Figure 2.3 are a simple expression of this principle: that two flocs with the same solids concentration can have a significantly different structure, external surface area, and presumably would experience different amounts of drag. This indicates that structural re-organization, without an increase in mass density could also produce the measured increase in effective floc density in the study of Farrow et al. (2000). Measurement of floc structure along with the settling velocity data before and after applied shear helpful to identify the cause of increased

effective density. For example, the relative compactness of flocs has been shown to change as a result of applied shear during growth (Chakraborti et al., 2003) and breakage (He et al., 2012) by calculating the fractal dimension of flocs after varying amounts of applied shear. Such an increase in relative compactness would change the drag coefficient and diameter of the flocs, and if all else was held equal in the calculation of effective density from Stokes' Law, an increase in effective density would be determined; although this would not equate with an increase in floc mass density.

Although the aggregate densification mechanism is widely described in the literature and is a useful concept for the purpose of theoretical models of consolidation, the physical basis of the mechanism is not well supported by direct measurements at this time. Alternatively, the enhanced consolidation observed in full-scale thickeners may be explained by aggregate breakage and structural re-organization due to the application of shear. In that case, mixing the sediment causes breakage of the aggregates into smaller, more structurally compact sub-units that have an improved packing efficiency. With reference to Equation 3.2, an increase in ϕ_s may be achieved through increased, φ_{agg}, rather than by an increase in aggregate solids volume fraction from $\phi_{agg,0}$. Partial support for this mechanism may be found in the general observation that flocs are one to two orders of magnitude stronger under compression than shear (Buscall et al., 1987). If that is so, then it may be suggested that mixing of a suspension of flocs is more likely to first cause the breakage of aggregates rather than densification of the aggregates. Yet, there is little physical evidence for this model either, which serves to highlight the need to support the mechanisms of consolidation with direct measurements of floc structure and composition. Part of the historic lack of knowledge in this area was caused by a lack of instrumentation and analytical methods to measure such properties. The next section describes how the understanding of floc structure has co-evolved with improvements in measurement technology, and most significantly, with imaging technology.

2.3 Role of imaging technology in floc structure research

In the early years of floc structure study, linear measures were widely reported in the literature, due to the technology available, while later a more advanced analysis was made possible with digital

images.

2.3.1 Inferred properties and linear measures

In the late 1950's until late 1970's, attempts to define floc size and structure were typically achieved by deduction from empirical results and theoretical simulation; although a few studies using images and various scattering methods were reported during this period. One of the earliest images, in 1963, of aggregated particulate material in the literature was of thorium oxide flocs in a SEM micrograph (Thomas, 1963). Slightly later, Mueller et al. used a planimeter and map measurer to obtain what is now called the major and minor axis of the floc (Mueller et al., 1967). The morphology of carbon black aggregates in SEM images was achieved by counting the number of particles and measuring the projected area in 1970 (Medalia, 1970). Otherwise, during this period, the majority of advances in understanding floc structure were made by deduction from empirical experiments.

The early era of empirical tests and theoretical models laid the groundwork for appreciating the irregular, multi-layer nature of floc structure. Relative changes in floc size have been inferred from changes in sediment settling rate (Slater and Kitchener, 1966), filtration rate (Smellie and La Mer, 1958), and changes in sediment volume ratio (Thomas, 1963). Vold reported the earliest simulation of floc structure, which suggested that flocs were formed by the successive addition of primary particles (Vold, 1963). However, Vold could not reconcile the presented model with the observation of significantly lower density in the sediments that formed in settling column tests. Soon after, a cluster-cluster simulation model of aggregation was proposed by Sutherland to account for extended, low density floc structures observed in sediment beds (Sutherland, 1967; Lagvankar and Gemmell, 1968). Simulations continued to be the dominant tool in the literature to understand floc structure in the 1970's (Goodarz-Nia, 1975).

In the late 1970's and early 1980's, electromagnetic scattering methods became and remained popular (including optical, neutron, and X-ray) for the characterization of small aggregate formation and structures. Total intensity light scattering (Munro et al., 1979), dynamic light scattering

(Feenstra and de Bruyn, 1980), and optical backscattering (Johnson and Wangersky, 1985) typically permit the measurement of hydrodynamic radius and shape factor of smaller (< 10 μm) aggregates. In the late 1970's, images of flocs were still being analyzed using enlarged, projected film by some researchers (Tambo and Watanabe, 1978). However, by the mid-1980's the era of digital image analysis had begun.

2.3.2 Fractal analysis

Images have become somewhat of a general purpose tool to analyse the features of aggregated suspensions, including changes in floc size and density (Klimpel and Hogg, 1986), the effect of flocculant and coagulation conditions (Shen and Maa, 2016), the position of flocs using stereoscopic methods (Syvitski et al., 1991), sediment transport in natural waters (Syvitski and Hutton, 1997; Curran et al., 2007), floc size monitoring in the sludge treatment process (Koivuranta et al., 2015), the relationship between floc solids concentration and applied shear (Tran et al., 2018), and floc deformation in flowing systems (Sun et al., 2016), to name but a few studies published on the image analysis of flocs.

Most of the measures used to analyze floc size and shape in this thesis are introduced in the chapter they are required. However, fractal theory, introduced by Mandelbrot (1975) to describe irregular and infinitely repeating mathematical patterns, has been so widely used to describe floc structure that the topic will be given more attention here. Based on the journal articles and proceedings papers published during the period 1990 to 2021, at least 11072 sources used the term floc; 932 sources used the term floc and fractal (about 1 in 12 of all papers on flocs); and 216 sources used the term floc, fractal, and image (about 1 in 4 of the papers that contained the term floc and fractal).

Application of fractal theory to flocs permits a description of the seemingly chaotic and varied structure of a floc, or a population of flocs, with a single parameter, the fractal dimension. The general concept of fractal scaling in flocs is based on the relationship between the number of particles in a floc and floc size according to (Bushell et al., 2002):

$$N = k_a \left(\frac{L}{L_p} \right)^{D_f}, \tag{2.5}$$

where N is the number of primary objects (particles or micro-flocs), L is some measure of linear size (characteristic diameter, length, or radius of gyration), L_p is the primary length scale (which may be particles or micro-flocs), D_f is the fractal dimension, and k_a is the exponential or structural pre-factor. D_f and k_a are inter-related parameters that may be plainly defined as the change in complexity with scale (D_f) and relative compactness or looseness of the structure (k_a). Fractal dimension may be measured from size-settling velocity measurements, optical scattering, or by image analysis.

Flocs may be considered natural fractals or rough approximations of fractals (Shenker, 1994) although several studies show that there are some practical and theoretical concerns with applying fractal analysis of flocs. Wong et al. (1988) showed that silica aggregates produced by polymeric flocculation have a highly ordered short-range structure that is incompatible with fractal theory. Fractal dimension has been found to vary with floc size, such that multiple fractal dimensions are required to characterize a population during growth and at equilibrium size (Chakraborti et al., 2003), which is incompatible with the concept that a single fractal dimension can be used to describe a sample of flocs across all size scales. Further, Heinson et al. (2015) found that it was necessary to include the scaling pre-factor and shape of the aggregates to completely describe the floc morphology. Such an approach has been confirmed by theoretical models which show that D_f and k_a are inter-dependent and also related to floc size (Gmachowski, 2002; Lapuerta et al., 2010). Most recently it was shown that the aggregation mechanism and composition contribute significantly to floc shape such that strong deviations from fractal behaviour are evident (Spencer et al., 2021). In these cases, it may be appropriate to describe observed size-property relationships as power-law scaling, rather than fractal scaling, as pointed out much earlier by Klimpel and Hogg (1986). Despite these issues with applying fractal theory to flocs, fractal dimension has remained a popular way to conceptualize floc structure and to justify and interpret the parameters of Equation 2.5.

While many studies have applied fractal analysis to 2D images, only a handful of studies to date apply the method to 3D images. The length-area-volume relationship and box-counting fractal analysis methods were popularized by Mandelbrot et al. (1984). The 2D length-area-volume estimate of fractal dimension, $D_{2,\mathrm{lav}}$, is often referred to as the perimeter-area method and may be determined from a binary 2D image according to:

$$A_\mathrm{c} \propto P_\mathrm{s}^{2/D_{2,\mathrm{lav}}}, \tag{2.6}$$

where P_s is the object perimeter, A_c is the object area, and $D_{2,\mathrm{lav}}$ is the fractal dimension of the object's perimeter. $D_{2,\mathrm{lav}}$ can take on values between 1 (for a perfect circle) and approaching 2 (as the shape approaches a straight line). Equation 2.6 is correctly applied to tomograms (slices) of material surfaces (Meakin, 1987) but has also been widely applied to projections of flocs in 2D (Spicer and Pratsinis, 1996; Chakraborti et al., 2003; Chu et al., 2004; Fan et al., 2017).

The 3D analogue of Equation 2.6 is

$$V \propto A_{3,\mathrm{s}}^{3/D_{3,\mathrm{lav}}}, \tag{2.7}$$

where V is the volume of the floc and $A_{3,\mathrm{s}}$ is the surface area of the floc. Although Mandelbrot (1982) made a passing reference to this approach in his 3D model of "flakes" produced by salting a soap solution, the method has not been reported elsewhere in the literature. Despite the name "perimeter-area fractal dimension", a serious drawback of this method is that $D_{2,\mathrm{lav}}$ and $D_{3,\mathrm{lav}}$ have an inverse relationship with the true fractal dimension (Florio et al., 2019). Two reports have been made that describe methods for determining the true 3D fractal dimension from the perimeter-area method (Maggi and Winterwerp, 2004; Expósito et al., 2017). Such a conversion is necessary such that the fractal dimension values may be used to correctly model the porosity, permeability, or volume of flocs. So, despite the ease of calculating the perimeter-area fractal dimension, a direct calculation of fractal dimension from images should be preferred.

Box counting can be applied to calculate fractal dimension directly from 2D or 3D images. In

that method, a count is made of the number N_b of boxes (in 2D) or cubes (in 3D) of size d_I required to completely cover the floc in the image at various values of d_I. The slope of the log-log plot of N_b versus d_I is the box-counting dimension, according to (Bushell et al., 2002):

$$D_{n,bc} = \lim_{d_I \to 0} -\frac{\log(N_b)}{\log(d_I)}, \tag{2.8}$$

where the sub-script n refers to the dimensionality of the image. $D_{bc,3}$ may take on values between 1 and 3 whereas $D_{bc,2}$ may take on values between 1 and 2. In each case, the lower limit (1) indicates a compact structure while the upper limit (2 for 2D; 3 for 3D) represents an object with a rugged and open structure that completely fills the volume. Box counting has been applied to measure the fractal dimension of maltodextrin agglomerates (Pashminehazar et al., 2018) and oil sands tailings structure (Govedarica et al., 2020).

While the acquisition of images of flocs in a settling column or stirred vessel is probably the simplest, least destructive means of assessing floc structure, 2D images have been shown theoretically (Hunt and Kaloshin, 1997) and experimentally (Orhan et al., 2016) to cause the loss or distortion of spatial information contained in a 3D image of an object. As such, the acquisition and analysis of 3D images represents an important way to obtain the deepest insights into floc structure.

2.3.3 Three-dimensional images

The advent and improvement of 3D imaging technology has provided remarkable new insights into floc structure, although many questions remain about how to best quantify flocs in 3D. An early attempt to obtain 3D information on internal floc structure was carried out in 1987 by Somasundaran et al. (1987), when that group scanned what appears to be a $>$ 5 cm polymer-flocculated kaolin floc at 0.75 mm image resolution. Although not specifically developed for surface reconstruction, the development of 3-camera optical arrays for stereoscopic measurement of flocs may also be seen as an early attempt at the measurement of 3D floc images (Syvitski et al., 1991). Those simpler methods are in contrast to the more sophisticated methods being developed currently, such as the image

correlation method demonstrated by Wheatland et al. (2020), which permitted a remarkable visualization of floc structure from the nano- to the millimetre scale, using several image technologies including micro-CT, TEM and SEM.

Three-dimensional images can be produced by thin section, scanning, or volumetric imaging methods. Flocs are fragile objects and handling them for sample mounting, even gently, will introduce some degree of rupture or breakage. Furthermore, the potential impact of freezing, drying, or mounting on the floc structure must be considered when choosing a sample preparation method. In the thin section method, the specimen is immobilized and thinly sliced using a microtome. Each thin section is imaged using the desired modality and the 3D image is reconstructed from the slices. Examples include cryo-SEM, cryo-TEM, and optical microscopy. SEM-FIB can produce a 3D image of small volumes of interest by successive imaging and milling the surface of a specimen. CLSM produces the 3D image by profiling the surface of the specimen with a laser. A limitation is that CLSM is a surface imaging method, so the full features of a folded or tortuous structure cannot be imaged. Nonetheless, several CLSM variants exist and stains can be used to enhance features of interest in the specimen (Liss et al., 1996). X-ray CT produces a set of 2D projections that can be reconstructed to form a 3D image, with spatial resolution typically on the order of 1 μm to 1 mm (Cnudde and Boone, 2013), although nano-CT is becoming more common in materials science. In CT, each voxel is related to the local composition of the specimen such that a complete determination of the structure and composition of the specimen can be made.

Immobilization of flocs is critical to obtaining 3D images with currently available thin-section, scanning-based or X-ray CT technology, as it is required that the specimen is stationary for the preparation of thin sections or for the duration of scanning. Mueller et al. (1967) reported the use of agar to immobilize flocs for optical microscopy, while Droppo et al. (1996) reported the use of agarose, a purified form of agar. A 10 % formalin solution can be used to harden flocs (Li and Ganczarczyk, 1990), which also has the benefit of killing microbial constituents of the floc. Formalin-hardening may be a good option for preserving floc structure, but it seems like it has only been used as a pre-treatment for thin-section methods, which require further immobilization steps

including dehydration, embedding in paraffin, sectioning with micro-tome, and melting away the wax. Perhaps formalin alone could be used o immobilize flocs for scan-based imaging techniques, although no such reports have been found in the literature. Glycol methacrylate has been reported to form a hardened material from which thin sections of good optical clarity may be produced (Ganczarczyk et al., 1992). An interesting approach to evaluating the effect of sample preparation (on soil samples) by Hapca et al. (2011) was to scan the sample with 3D X-ray CT, then align chemical maps from scanning electron microscopy with energy dispersive X-ray (SEM-EDX) to permit an assessment of the geometric distortions caused by sample preparation.

A non-chemical means of floc immobilization is by the physical constraint of flocs in a sediment bed or packing structure. With this method, the flocs in the upper portion of the sediment constrain the movement of the flocs in the lower portion of the sediment while the 3D image is acquired. A requirement is that the sediment bed has reached an equilibrium height, such that flocs are stationary, relative to the duration of the scan. This is perhaps the least damaging means of immobilization, but flocs are not separated in the resultant 3D image, so post-processing is required to extract and analyze the flocs (Sharma et al., 2017). This thesis made significant use of X-ray CT, so the last section of this chapter provides a high-level background on X-ray CT theory and calibration.

2.4 X-ray computed tomography measurements

In a typical CT instrument, an X-ray beam is passed through the specimen while transmission images, or projections, are recorded at a series of small angular offsets (Cnudde and Boone, 2013). A schematic of a CT instrument showing an X-ray source, detector, and sample are shown in Figure 2.4.

For minerals, in general, the photoelectric effect is the dominant attenuation mechanism at low X-ray energies, between approximately 20-100 keV. Photoelectric absorption occurs when the total energy of an incoming X-ray photon is transferred to an inner electron, causing the electron to be ejected. Photoelectric absorption is proportional to Z^4 or Z^5 where Z is the atomic number of an

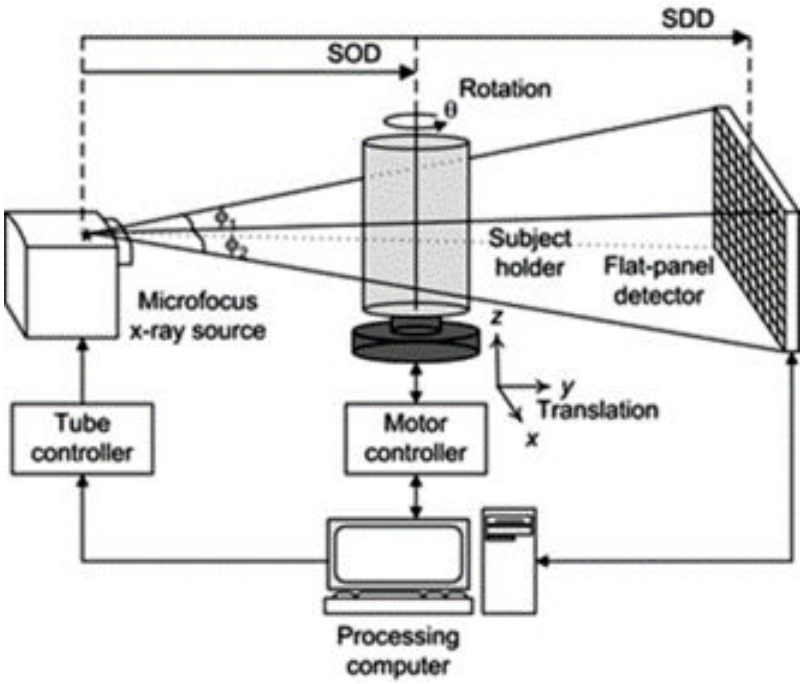

Figure 2.4: Schematic of X-ray computed tomography instrument, reproduced from Kim et al. (2011).

atom in the attenuating material (Van Grieken and Markowicz, 1993).

The Beer-Lambert Law describes the attenuation of a narrow beam of mono-energetic X-rays passing through a homogeneous medium (Baker et al., 2012),

$$I = I_0 \exp(-\mu x), \tag{2.9}$$

where I_0 [keV] is the initial X-ray intensity, μ [cm^{-1}] is the linear attenuation coefficient, x [cm] is the X-ray path length through the material, and I is the intensity of the transmitted photons. For a mixture or compound, μ is proportional to the weighted fractions of the mass attenuation coefficients of the components in the mixture according to

$$\mu = \rho_m \sum_i w_i \left(\frac{\mu}{\rho}\right)_i, \tag{2.10}$$

where w_i and $(\mu/\rho)_i$ [cm^{2}g^{-1}] are the fraction by weight and the energy-dependent mass attenuation coefficient of the i^{th} component and ρ_m is the mass density of the mixture. Mass attenuation

coefficients can be calculated for any combination or proportion of elements in a mixture using the XCOM database from National Institute of Standards and Technology (NIST) (Berger et al., 1999). Equation 2.10 implies that the μ value of a single volume element, or voxel, composed of a mixture of components is a linear combination of the μ value of those elements according to their volumetric proportions.

After acquisition of the projections, the 3D image is reconstructed. Reconstruction of an X-ray image is the process of estimating the internal spatial distribution of a parameter from its projections (Taguchi, 2013). The most common method is filtered back-projection (FBP), which was applied in this thesis through the UFO-Kit implementation by Vogelgesang et al. (2012). To achieve a good result with FBP, it is necessary to satisfy the Nyquist criterion (at minimum), which is that the sampling frequency must be at least twice the maximum spatial frequency present. If the sample rotates (i.e. rather than the X-ray source and sensor array), then the sample must be prepared to rotate perfectly on its axis, otherwise it is exceptionally challenging to apply the FBP correctly.

Researchers have employed a variety of calibration strategies to permit phase identification and evaluation of composition from CT images. Strategies include the direct measurement of samples of known composition, the measurement of samples with accurately known μ value, and image correlation. CT calibrations are system and instrument specific. Aside from changes in the sample, measured image intensity may change due to X-ray tube geometry, source energy, sample-to-detector distance, sample thickness, and detector characteristics (Wildenschild and Sheppard, 2013; Mashiatulla et al., 2017). Thus, it is important that a measured calibration is applied under similar conditions, i.e. that variables such as the sample thickness and means of containment, beam voltage and current, and detector exposure time are kept consistent.

The Hounsfeld Units (HU) scale, which makes a linear calibration of from -1000 HU (air) to 0 HU (water), is well-defined in medical research applications. The HU scale has been applied to obtain an indication of relative density change in packed powder beds (Mendez et al., 2011), but the need for photoelectric correction complicate its use in mineral systems (Duchesne et al., 2009).

Sharma et al. (2017) calibrated CT images for floc water content using a series of clay in water standards. In the medical application of bone density measurement, a series of samples of varying composition have been embedded in epoxy (Mashiatulla et al., 2017) or prepared in watery solutions (Prevrhal, 2005) to obtain a calibration of image intensity to hydroxyapatite concentration. Dong et al. (2018) used a multi-element calibration carousel to generate a calibration curve which permitted the expected monochromatic X-ray attenuation values to be calculated from X-ray polychromatic X-ray projection data. Calibration of CT image intensity for absolute density of mixed mineral substances has been carried out with a multi-element calibration carousel, but can only be applied if the sample composition is known (Davis et al., 2015). Similarly, Jussiani et al. (2016) used a multi-material calibration carousel to permit identification of mineral phases, but did not extend the calibration to permit determination of mineral concentration.

An alternate approach is to calibrate image intensity to μ. This can be achieved by the measurement of a series of standards of known composition and μ value (i.e. they have been measured using synchrotron source CT). The energy-dependent μ values of Equation 2.10 can be calculated using the XCOM tables from NIST (Berger et al., 1999) to validate the results obtained. For many minerals, the chemical formula and mass density are well-defined, so the XCOM tables can be used to calculate μ as a function of incident X-ray energy. This can also be used to obtain the theoretical CT response and to predict the ability to differentiate between given minerals at a specific X-ray energy (Wildenschild et al., 2002). For micro-CT measurements, the energy source is a polychromatic X-ray characterized by its peak voltage [kVp] and current [μA], rather than its energy [keV], so an indirect method must be used to predict μ values. In this case, the measured μ value (from the CT instrument) can be looked-up on a curve of energy-dependent μ values (from the NIST tables) to estimate the incident energy in keV (Mulder et al., 2004).

The use of image correlation is another means of calibrating CT images. Image registration has been gaining popularity in the past 30 years, with wide-ranging applications in the medical, engineering and scientific fields. Nonetheless, there are still uncertainties when considering the best choice of strategy and workflow for correlative experiments (Miller et al., 2018), which indicates

there is still a need for innovation and development by practitioners in this field. Relevant to the application at hand, image correlation between CT (3D) and SEM-EDX (2D) images is a means of labelling one or more phases in a CT image with chemical or mineralogical information.

While open-source and commercial options exist for 2D image registration, there is no complete commercial or publicly available software for volumetric registration (3D-3D and 2D-3D), although solutions have been outlined in the literature. Latham et al. (2008) described the development of a highly efficient method for the successive interpolation of 2D images from the CT image volume for comparison to the target SEM images. Those authors suggested (but did not carry out) the potential for mapping gray levels of the CT image to mineral phases based on the SEM-EDX data. Lau et al. (2012) made a more detailed attempt at showing how mineral phase information could be linked to the gray levels of a CT image via correlation with the gray levels of the SEM back scatter electron BSE image (but not explicit chemical or mineral information from the SEM-EDX images). A similar approach was taken by Ramandi et al. (2017), in the correlation of CT and SEM grayscale values to improve the identification of pores in rocks. Essentially, that study used SEM images as a means of determining an accurate grayscale values in the CT image that were associated with pores in the SEM images. Hapca et al. (2011) used registered CT and SEM images to evaluate the distortion caused during SEM sample preparation, rather than to assign phase information to the CT image. A study of the effect of bone scaffolds on bone porosity by Lewin et al. (2017) used CT-SEM registration to measure changes in the volume fraction of bone measured in the CT images. The foregoing studies typically used CT-SEM registration to identify a phase of interest in the CT image, which permitted the measurement of a physical property of interest on that phase.

It seems that Lewin et al. (2017) could have extended their analysis by including a calibration for bone mineral content (commonly done in medical imaging sciences), but their evaluation of bone porosity relied only on volume fraction of pores in the calibrated CT images. However, such an approach has not been demonstrated in the literature at this time. As such, multi-step calibration procedures (that identify the phase of interest and evaluate its composition) represent the state of

the art in CT-SEM registration workflows. This approach is useful where the phase of interest cannot be deduced from visual inspection or from the image histogram.

In the first study of this thesis, Chapter 3, a novel method was described for preparing ϕ_s calibration standards for binary mixtures of quartz and water. Direct measurements with CT scans at various stages of compression were used to investigate the response of flocculated quartz in the initial stage of sediment bed dewatering. Chapter 4 is the follow-up study to Chapter 3, which shows that the sediment beds studied in Chapter 3 were comprised of flocs that had a weakly bound macro-structure, held together by low-ϕ_s regions of comparatively lower strength.

Chapter 3

Aggregate density changes during compression of flocculated silica

3.1 Introduction

Flocculation is an important pre-treatment in the solid-liquid separation of fine particulate suspensions, but there is still much to be learned about the relationship between flocculated sediment structure and subsequent dewatering characteristics (Gladman et al., 2006). During flocculation, water is trapped inside flocs and as these aggregates settle, water occupies the volumes between the network of touching aggregates. Removal of both the inter- and intra-aggregate fluid is typically necessary to meet process objectives, such as increased water recovery from the waste or decreased moisture content in a product, and is often achieved in a thickener, filtration, or combination of both. Different compression strategies may change the amount of energy required per unit volume of fluid recovered (Glasgow, 2003), so the ability to measure changes in the inter- and intra-aggregate fluid content of a sample under compression would contribute to an understanding of the compressive dewatering characteristics of flocculated suspensions.

The theory of CR is a well-developed framework for describing changes in the average solids concentration of a suspension as a function of process variables during sedimentation and compression (de Kretser et al., 2003). A fundamental limitation of the explanatory power of the theory,

however, is its treatment of suspensions as homogeneous fluids, with an average solids volume fraction, ϕ, rather than as particulate suspensions with local variations in solids concentration. A more recent modification to the theory of CR involved the consideration of the fractional volume that aggregates occupy, φ_{agg}, and the addition of an inferred aggregate diameter parameter to explain changes in sediment structure due to applied shear in a thickener (Usher et al., 2009). This modification represents the first explicit inclusion of physical parameters to describe the aggregate phase in CR theory, and serves to highlight the need for a micro-scale understanding of dewatering mechanisms by the inclusion of new parameters to describe the spatial distribution of solids during suspension dewatering.

As a flocculated suspension settles, ϕ increases as water is displaced by the downward movement of aggregates. When ϕ increases to the gel point, ϕ_g, a network of touching aggregates, surrounded by fluid, forms (Landman and White, 1994). The aggregates occupy a partial volume fraction, φ_{agg}, of the total sediment volume,

$$\varphi_{agg} = \frac{V_{agg}}{V_t}, \tag{3.1}$$

where V_{agg} is the partial volume of the aggregate phase, and V_t is the total sediment bed volume. If it is assumed that all of the solids in a well-flocculated suspension are contained in the aggregate phase, the solids volume fraction of the aggregate phase, ϕ_{agg}, can be written as (Spehar et al., 2015),

$$\phi_{agg} = \frac{\phi}{\varphi_{agg}}. \tag{3.2}$$

These equations indicate that an aggregate has a volume which may contain varying ratios of solid and liquid. As a result, aggregates may be characterized by differing solids contents, and the density of aggregates can be expected to fall between the density of the liquid and the density of the solid.

In this chapter, a method is described for using micro-CT to measure φ_{agg} and ϕ_{agg} directly in

the sediment bed as a function of applied pressure during the low pressure compression of flocculated silica. A method is described for the preparation of micro-CT mass density standards to obtain quantitative ϕ_s information from CT images. A miniature compression apparatus was developed to permit compression and scanning of the samples by micro-CT without disturbing the samples. Evaluation of the calibrated images for samples at different applied pressures permitted trends in φ_{agg} and ϕ_{agg} to be observed, which revealed new insights about the low-pressure dewatering mechanisms of flocculated media.

3.2 Methods and Materials

Silica suspensions were flocculated, compressed, then imaged with a micro-CT scanner to permit calculation of aggregate properties as a function of applied pressure. A calibration of the micro-CT instrument with samples of varying silica content was carried out to permit ϕ_s calibration of the CT images. Parameters for the micro-CT scanned compression trials, including applied pressure and polymer dosage, were determined by measurement of the compressive yield stress of flocculated silica over a range of applied polymer doses. For the trials scanned with micro-CT, duplicate trials of flocculated silica, compressed with four different applied pressures, were scanned at different heights in the sediment bed to permit calculation of ϕ_s, ϕ_{agg}, and φ_{agg} from Equations 3.1 and 3.2.

3.2.1 Flocculation

Samples were prepared for the compression experiments by flocculating a suspension of fine, 99.5 % silica powder (Alfa Aesar, Ward Hill, MA), with particle size d_{50} = 2.5 μm and d_{90} = 7.4 μm. Suspensions were prepared in 1 mM KCl at 5 % w/w solids without modifying the pH in a glass beaker, by stirring with a magnetic stir bar for 15 minutes before use. A medium-high-molecular weight cationic polyacrylamide (CPAM), Cyfloc C-491 (Cytec, Woodland Park, NJ, USA), was prepared as a 1 g/L stock solution by adding 0.25 g CPAM to 250 g distilled water then stirring for 4 hours before use. The stock solution was then diluted to 0.1 g/L and the required dose of CPAM was injected into the silica suspension while it was stirred at 200 RPM with a magnetic stir bar.

The stirrer was stopped after another 5 seconds of stirring at 200 RPM. As noted by Rattanakawin and Hogg (2001), addition of a high molecular weight polymer to an unstable suspension causes rapid floc growth with essentially complete incorporation of the primary particles into flocs.

3.2.2 Compression

Low-pressure compression dewatering of the flocculated silica samples, up to 75 kPa applied pressure, was carried out with the apparatus depicted in Figure 3.1. The cell was fabricated from a modified 5 c.c. Cadence Micro-Mate (Cadence Science Inc., RI, USA) syringe. The tip of the syringe plunger was removed and replaced with a flat metal plate on one end and a small acrylic barrel was installed to act as a load support on the other end. The luer lock and tip of the syringe were removed and a custom base was fabricated by mounting a short piece of the original plunger in a piece of machined acrylic and attaching a perforated filter support. A barbed fitting was epoxied to the base of the cell and a piece of 1/16" ID PVC tubing was connected to transport fluid to a small beaker on an analytical balance.

At the beginning of a compression trial, a piece of medium flow Whatman No. 2 filter paper was placed on the filter support and the cell base was filled with water. The compression cell was then filled with flocs up to about 10 mm below the top of the cell wall, which permitted the ram to be placed in contact with the top of the sediment bed. At the beginning of each trial, the drain tube was clamped shut to prevent compression of the sediment bed. The distance between the lower tip of the ram and the top of the filter support was measured, which is referred to for the rest of the paper as the compression chamber height. The fluid drain tube was opened which caused the sediment bed to compress due to the weight of the ram. Fluid flow from the cell was collected on an analytical balance connected to a computer. After no additional drops of fluid were recorded on the mass balance for a period of 10 minutes, the compression chamber height was measured and a steel disk of the required weight was placed on top of the ram. At the end of each compression trial, the sample was removed and dried to measure the solids volume fraction, ϕ, gravimetrically. This sequence was repeated three times for each applied polymer dosage. For the compression

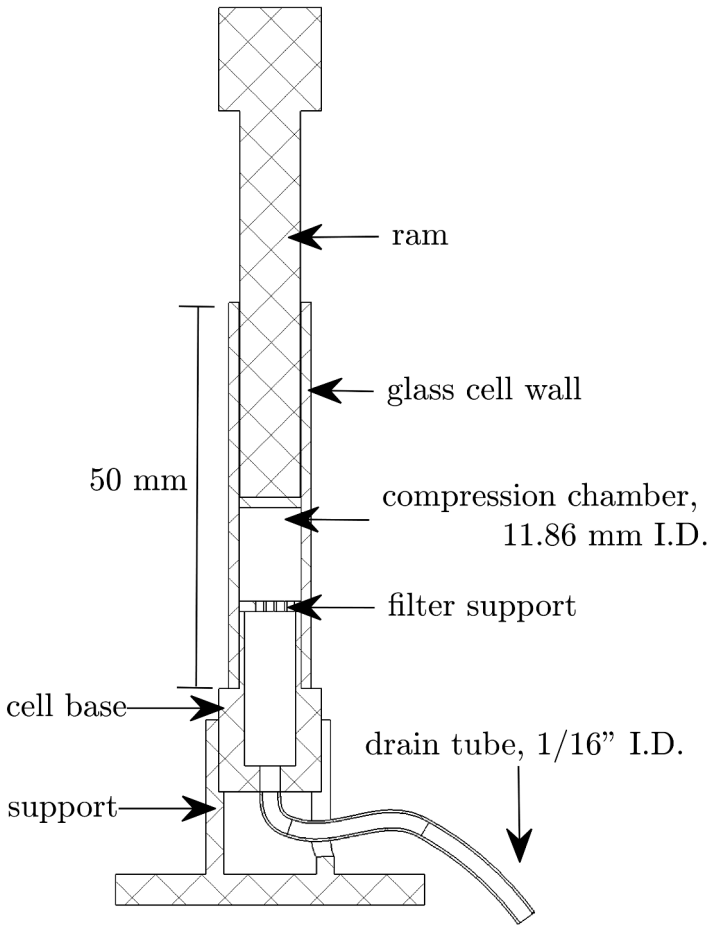

Figure 3.1: Glass-walled compression cell apparatus with removable sample cell for CT measurements.

trials that were measured with micro-CT, a single polymer dosage was selected and replicate trials were carried out at four different applied pressures.

3.2.3 Micro-CT measurement

A SCANCO μ CT100 (SCANCO Medical AG, Switzerland) was used to measure volumetric CT images of calibration specimens and compressed flocculated suspensions at 90 kVp and 200 μA with a 0.5 mm Al filter. The data were obtained in the form of a stack of 2D images in the DICOM format. A 36.7 μm voxel resolution was used for the mass density calibration scan to permit the entire calibration carousel to be scanned in a single measurement. A 7.4 μm voxel resolution was used for micro-CT scans in the compression experiments. For the compression experiments, the

images were 2048 x 2048 voxels, which resulted in a field of view field of view (FOV) of 15.15 mm x 15.15 mm x 1.51 mm for the stack of 204 images.

Calibration standards

Calibration standards were prepared to measure a calibration curve of micro-CT image intensity values to mass density. A powdered silica was added to a solution of Superfloc A-130 (Cytec, Woodland Park, NJ, USA), an anionic polyacrylamide (APAM) of moderate charge density and a viscosity average molecular weight of 4.7 x 10^6 Da (Arinaitwe and Pawlik, 2009). The polymer solution was prepared at 1 g/L by adding 0.5 g of polymer to 500 mL deionized water, then stirring at 400 rpm for one hour, followed by slower stirring for six hours. Between 15 to 30 g of APAM solution was dispensed into each 50 mL glass sample vial, followed by the addition of varying amounts of silica powder, to produce samples of varying mass density. The silica was added in three stages followed by vigorous manual shaking and 10 minutes in an ultrasonic bath. The mass density of each suspension was measured with a handheld density meter (DMA 35N, Anton Parr, Germany) after preparation and after a three-hour period.

A 4 mL aliquot of 4 different silica calibration suspensions, one deionized water sample, and one APAM solution sample were transferred to capped Micro-Mate syringe tubes, then each tube was placed in a custom fabricated PTFE sample vial holder for micro-CT measurement. Immediately prior to CT scanning, the samples were vigorously shaken and placed in the ultrasonic bath. In addition, a pure quartz crystal (Ward's Science, Rochester, New York) was CT scanned to obtain a point for $\phi = 1$ on the calibration curve. The specific gravity of the quartz crystal was measured at 2.650 by the submersion method. The total time for each micro-CT scan was approximately 70 minutes.

To obtain the micro-CT values for each sample, a 3D region-of-interest was selected that corresponded to the sample position in the images. For the suspensions, a circular region corresponding to the inner diameter of the sample vial was selected over the entire height of the CT scan. For the quartz crystals, 10 regions were selected. A single mean and standard deviation was calculated for

each sample from all of the voxels selected for each sample.

The mass density calibration for the micro-CT images may also be converted to a calibration for ϕ, by converting the ρ_m value of each voxel according to:

$$\phi_i = \frac{\rho_{m,i} - \rho_l}{\rho_s - \rho_l}, \tag{3.3}$$

where ϕ_i [–] is the solids volume fraction, $\rho_{m,i}$ [g/cm^3] is the calibrated mass density for a single voxel, i, in the image, and ρ_l [g/cm^3] and ρ_s [g/cm^3] are the mass density of water and the solid phase.

Image processing

For each flocculated, compressed silica sample, four different height positions were CT scanned for the purpose of calculating sediment properties, ϕ, ϕ_{agg} and φ_{agg}, as a function of height in the sample. An example is shown in Figure 3.2, where an image of a flocculated, uncompressed sample is positioned next to its corresponding low-resolution overview image. The overview images permitted the location of each high-resolution scan to be located in the sample relative to the bottom of the sediment bed. The sample shown in Figure 3.2 was scanned at four different heights (h1, h2, h3, and h4), and the sediment properties were calculated for each position from the measured CT images. Note that the heights (h1, h2, h3, and h4) will be different for each sample because the sediment bed height changed as the sample was compressed, although an attempt was made to obtain four evenly spaced scans for each sample.

To apply the micro-CT calibration and calculate properties from the images, it was first necessary to segment the raw images to obtain the aggregate and fluid phases. The first segmentation step was to extract the region of the images that corresponds to the inside of the cell by manually selecting the inner wall of the cell in the images. This process generates a binary image mask where 1's correspond to the region-of-interest, the cell volume, and 0's correspond to the background, the cell wall and surrounding air. A second segmentation was carried out on the region inside the cell by applying a random walker segmentation to the cell masked image.

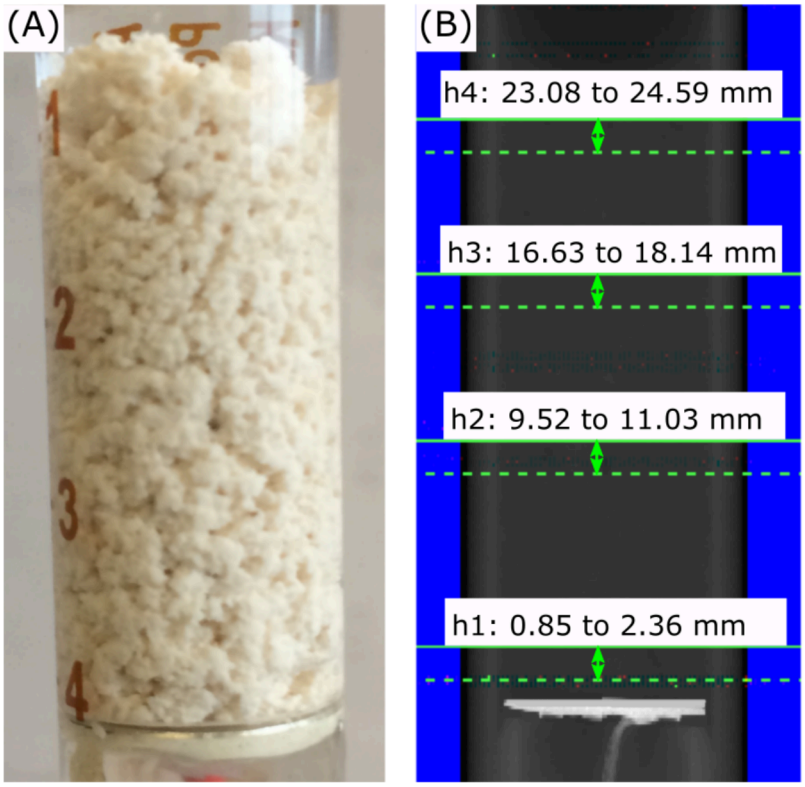

Figure 3.2: Image of (A) flocculated silica in the compression cell and (B) the corresponding low-resolution overview scan measured before each series of height scans. The white area at the bottom of the overview scan in (B) is the filter plate and the heights, h1 to h4, are the distance of the bottom, marked in a dashed green line, and top, marked with a solid green line, of the CT-scan region from the top of the filter plate.

A set of markers were generated from the measured CT calibration to initialize the random walker algorithm. Voxels with CT value < 2000 were assigned to the fluid, or background phase; while voxels with CT value > 3500 were assigned to the aggregate phase. Voxels with CT values between the foreground and background marker values remain unassigned when the algorithm is initiated. The algorithm then sends random walkers from each unassigned voxel to determine the probability that it will reach either the foreground or background first. By assigning the initially unassigned voxels to the phase that the random walker has the highest probability of reaching first, a high-quality segmentation that incorporates spatial connectivity of the phases can be obtained (Grady, 2006). After applying the cell mask and random walker segmentation, only the voxels that

correspond to the aggregate phase remained for onward calculations.

For each height position in each sample, the calibrated, masked CT images could be used to calculate φ_{agg} from Equation 3.1, ϕ_{agg} from Equation 3.2, and the average solids volume fraction, ϕ. Aggregate volume fraction, φ_{agg}, was calculated directly from the binary CT images. Each voxel represents a finite volume, based on the size resolution of the measurement, so the total aggregate volume, V_{agg}, can be calculated by a summation of the voxels with value equal to 1 while the total volume inside the cell for a given scan, V, is obtained by summing all of the voxels in the image stack that are inside of the cell.

Aggregate solids volume fraction, ϕ_{agg}, and average solids volume fraction, ϕ, were calculated from the calibrated mass density images. To obtain the volume of solids in a single voxel, the mass density value of each voxel i is first converted to a solids volume fraction with Equation 3.3, then multiplied by the metric voxel volume to obtain the mass of solids in that voxel. The mass of solids in the voxel is then divided by the mass density of the solid phase, 2.65 g/cm^3 in the case of silica, to obtain the volume of solids in the voxel. This calculation is applied to all of the voxels in the aggregate phase to obtain the total volume of solids in the scanned region, V_s. Dividing V_s by by the volume of the cell, V_t, gives the average solids volume fraction, ϕ, and dividing V_s by the aggregate volume, V_{agg}, gives the solids volume fraction of the aggregate phase, ϕ_{agg}.

At the end of each compression trial or CT-measurement, the plug of compressed material was removed and dried for measurement of ϕ by the gravimetric method for comparison to the values calculated from the CT images.

3.3 Results & Discussion

Calibration of CT number (i.e. the grayscale intensity) for ϕ in the micro-CT images permitted the calculation of aggregate solids volume fraction ϕ_{agg} and average solids volume fraction ϕ in the cell directly from the measured micro-CT images of flocculated, compressed silica.

3.3.1 Image calibration

A calibration of the CT response for solids volume fraction was obtained by measuring the three polymer-stabilized silica suspensions, deionized water, a background polymer solution, and quartz crystals. The ρ_{m} and ϕ value for each calibration standard is shown in Figure 3.3. A linear fit of the calibration measurements had a high coefficient of correlation, R^2, and root mean square error (RMSE) across the entire solids volume fraction range, from $\phi = 0$ to 1.

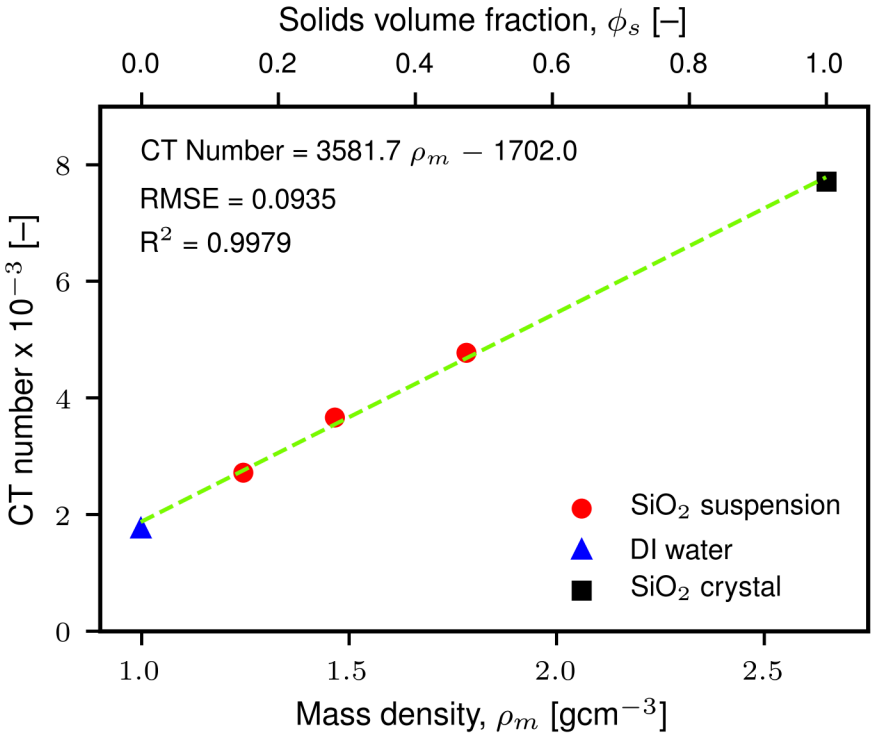

Figure 3.3: Calibration of measured CT number to mass density, ρ_m, with conversion to average solids volume fraction, ϕ. Error of one standard deviation was smaller than the marker size for each of the calibration standards.

The calibration suspensions were sufficiently stable against sedimentation and aggregation during the course of the CT measurements, as judged by the handheld mass density measurements and small standard deviation in the measured CT number for each standard. The mass density of the silica calibration standards were measured after initial preparation, then again after a three-hour period and it was found that the relative change in mass density of the suspensions was less than

0.5 % in each of two trials across the mass density range.

The trend in standard deviation for the CT number of the calibration samples indicates that aggregation was not significant in the silica suspensions. Aggregation would be visible in the CT images as local fluctuations in attenuation, or by alternation between higher and lower CT value. If there was any aggregation in the suspensions, it resulted in sub-voxel sized aggregates (calibration voxel size was 36.7 μm) that could not be discerned in the micro-CT images. The standard deviation of the CT number for the three silica suspensions was between 92.4 to 118.6 which was lower than the value for the solid crystalline silica sample, 160.0, but slightly higher than the value for deionized water, at 80.7.

The deionized water and crystal samples are expected to be the two most homogeneous samples, although they still exhibited a finite standard deviation in their measured CT values. This variation in CT values was likely caused by the differential absorption of X-rays of varying energy level throughout the material due to the polychromatic nature of the micro-CT X-ray beam (Wildenschild and Sheppard, 2013). These observations indicate that the calibration suspensions were stable at least until the calibration scans were complete. The high concentration of polymer likely results in steric dispersion of the silica particles, while the relatively high viscosity of the aqueous phase (polymer solution) slowed down the settling of the particles.

To demonstrate the image handling and mass density calibration procedures, a sub-volume of a single 2D image of flocculated, uncompressed silica is shown in Figure 3.4. In the raw grayscale image, Figure 3.4 (A), the brighter areas are volumes occupied by flocculated silica while the darker regions are those occupied by fluid. A contour line is plotted in green to indicate the interface between the aggregate and background fluid phase that was achieved by applying the random walker segmentation. The binary image in Figure 3.4 (B) is produced by setting the volumes occupied by aggregates equal to 1, shown in white, and the volumes occupied by fluid are set to 0, shown in black. This binary image can then be multiplied by the raw CT image to isolate the aggregate mass density voxels, which are then converted to ρ_m using the linear calibration shown in Figure 3.3.

There was a good agreement between the average solids volume fraction, ϕ, measured gravimetrically, and those calculated from the micro-CT images by applying the mass density calibration, refer to Table 3.1. Micro-CT scans were measured at four different places in the samples used for the compression trials, as shown in Figure 3.5 (A). To compare the ϕ from the CT data to the gravimetric values, the mean was taken of the four ϕ values, obtained at different heights in each sample.

Table 3.1: Sediment properties calculated from the gravimetric (grav.) method and from micro-CT (μCT) images and the relative error between the two values (RE).

Trial	ϕ_s, grav. [$-$]	ϕ_s, μCT [$-$]	RE [%]
1, P_0	0.152	0.138	9.21
2, P_0	0.159	0.153	3.77
3, P_1	0.187	0.197	5.35
4, P_1	0.175	0.157	10.29
5, P_2	0.290	0.304	4.83
6, P_2	0.297	0.290	2.36
7, P_3	0.401	0.454	13.21

3.3.2 Compression tests

The objective of the baseline compression tests was to select a polymer dosage and set of applied pressures for the compression trials that would be measured by micro-CT. In Figure 3.6, the averaged compression curves of samples of silica flocculated with between 200 and 800 g/t CPAM are shown. The compression curves appear to be a function of polymer dosage at lower applied pressures, but the applied dosage does not appear to impact the final solids content achieved. Toward the highest applied pressure, 75 kPa, the compression curves tended to converge on average solids volume fraction values ϕ = 0.38 to 0.4.

For CPAM doses between 200 g/t and 600 g/t, a trend of increasing resistance to compression is observable because the curves are shifting to the right, which indicates that a larger force is required to collapse the sediment bed to a higher average solids volume fraction, ϕ. At the highest dosage, 800 g/t CPAM, a decrease in resistance to compression is observed. This decrease in

resistance to compression at higher flocculant doses is consistent with the discussion of Landman and White (1994) on red mud flocculation, where they noted that there was a dosage that made the sediment easiest to compress. It is commonly thought that smaller flocculated aggregates are more resistant to compression than larger aggregates (Jarvis et al., 2005a), which is consistent with the results here for polymer doses between 200 and 600 g/t CPAM, where a decrease in resistance to compression of the sediment occurs when the polymer dosage, and consequently the aggregation state of the sediment, increases as a result of increased flocculant dosage (MacIver and Pawlik, 2017a,b).

3.3.3 Aggregate properties

In Figure 3.7, a single representative micro-CT image is shown from each applied pressure step to indicate the increase in aggregate volume fraction that occurred as the applied pressure was increased. Likewise in Figure 3.8, a set of 3D model pairs, for aggregate and fluid phases, are shown after varying levels of pressure were applied. The term "floc" was avoided here because it was not possible to clearly distinguish individual flocs in these micro-CT images. In the unstressed and lightly stressed sample, P_a = 1 kPa, it was difficult to visually discern a difference in aggregate volume content. The aggregate volume fraction, φ_{agg}, for the lower part of the unstressed samples is around 0.65; which is coincidentally the random close packing limit of hard poly-disperse spheres (Baranau and Tallarek, 2014a).

After a slight increase in applied pressure, to 3 kPa, however, a significant change in φ_{agg} occurs which greatly reduces the fluid volume surrounding the aggregate phase. At the final pressure step (75 kPa), the aggregate phase occupies the entire volume between the filter plate and the ram and there are no pores visible in the images. This reduction in pore volume and increase in φ_{agg} can explain the large increases in ϕ that occur at low applied pressures in Figure 3.6. A similar trend is observable in Figure 3.8, where a decrease in the pore volume can be seen with each pressure increase, from 0 to 3 kPa, which then disappears at 75 kPa.

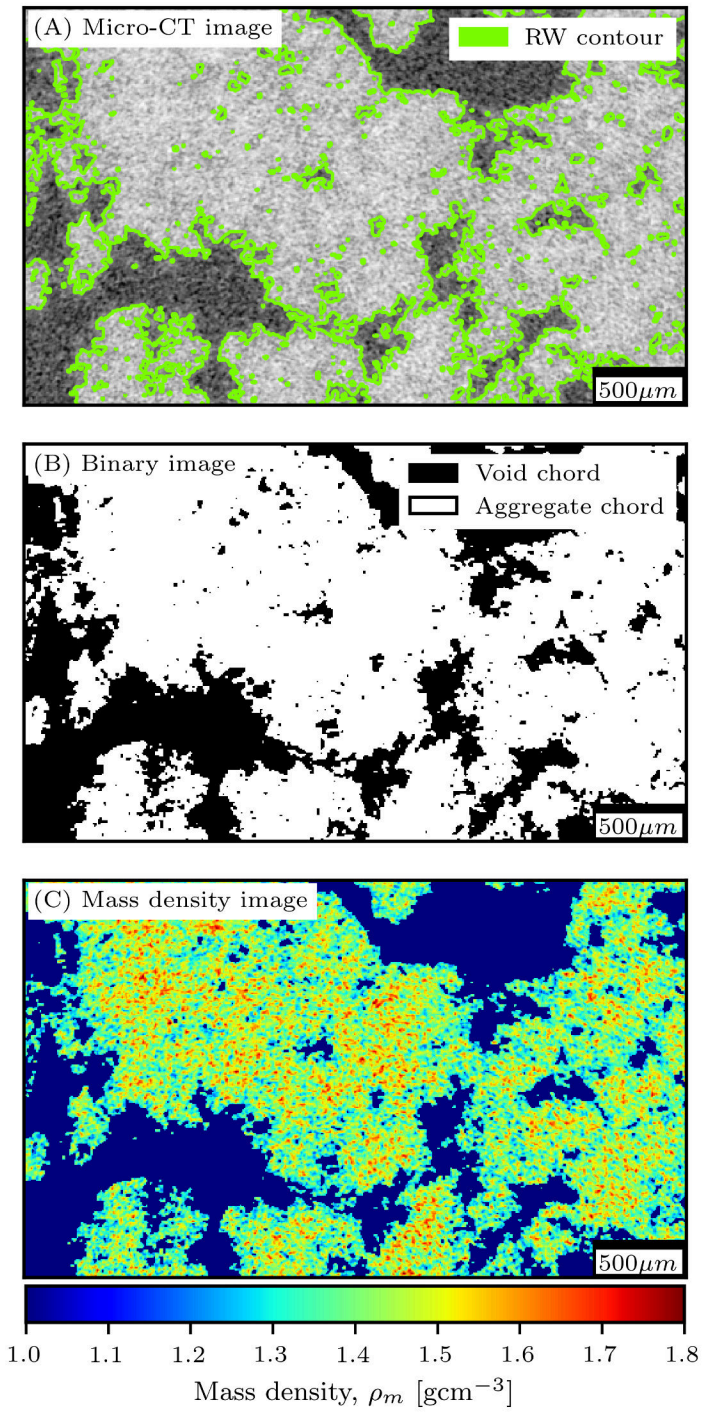

Figure 3.4: (A) Raw micro-CT image of flocculated silica with the random walker segmentation shown in green, and the corresponding (B) binary and (C) calibrated mass density, ρ_m images.

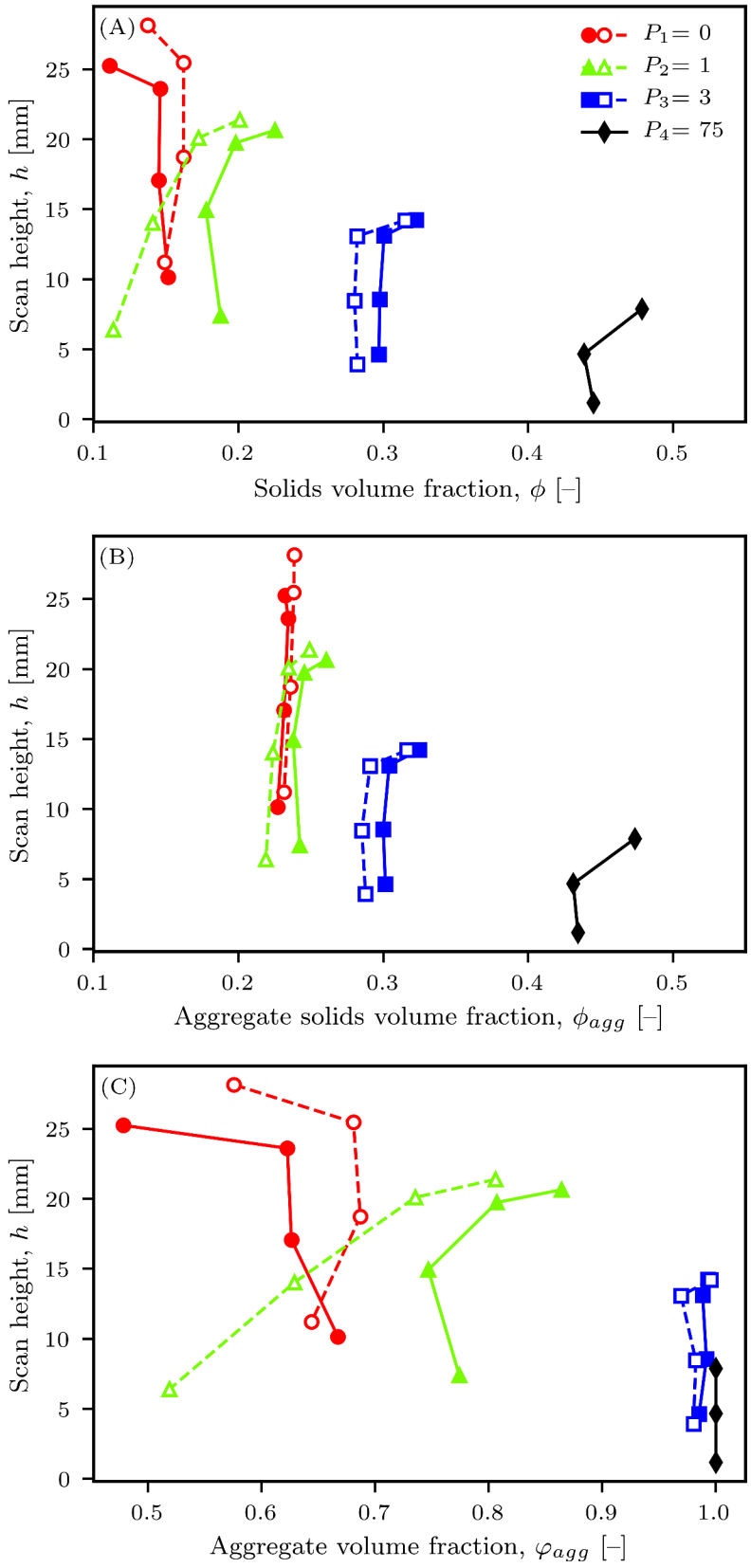

Figure 3.5: Aggregate properties calculated from micro-CT images as a function of CT-scan height in each sample and as a function of pressure across different samples in a series of stepped compression trials. The open and closed symbols indicate the repeat trial for each applied pressure, except P_4, where only one trial was completed.

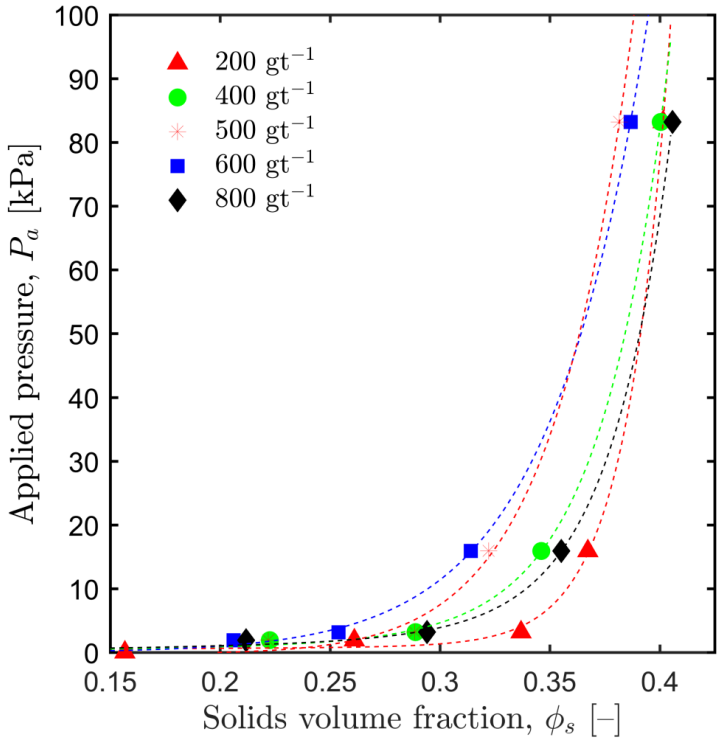

Figure 3.6: Applied pressure versus solids volume fraction after compression, ϕ for the staged compression of a 5 % w/w (1.95% v/v) silica suspension flocculated by varying dosage [g/t] of cationic polyacrylamide.

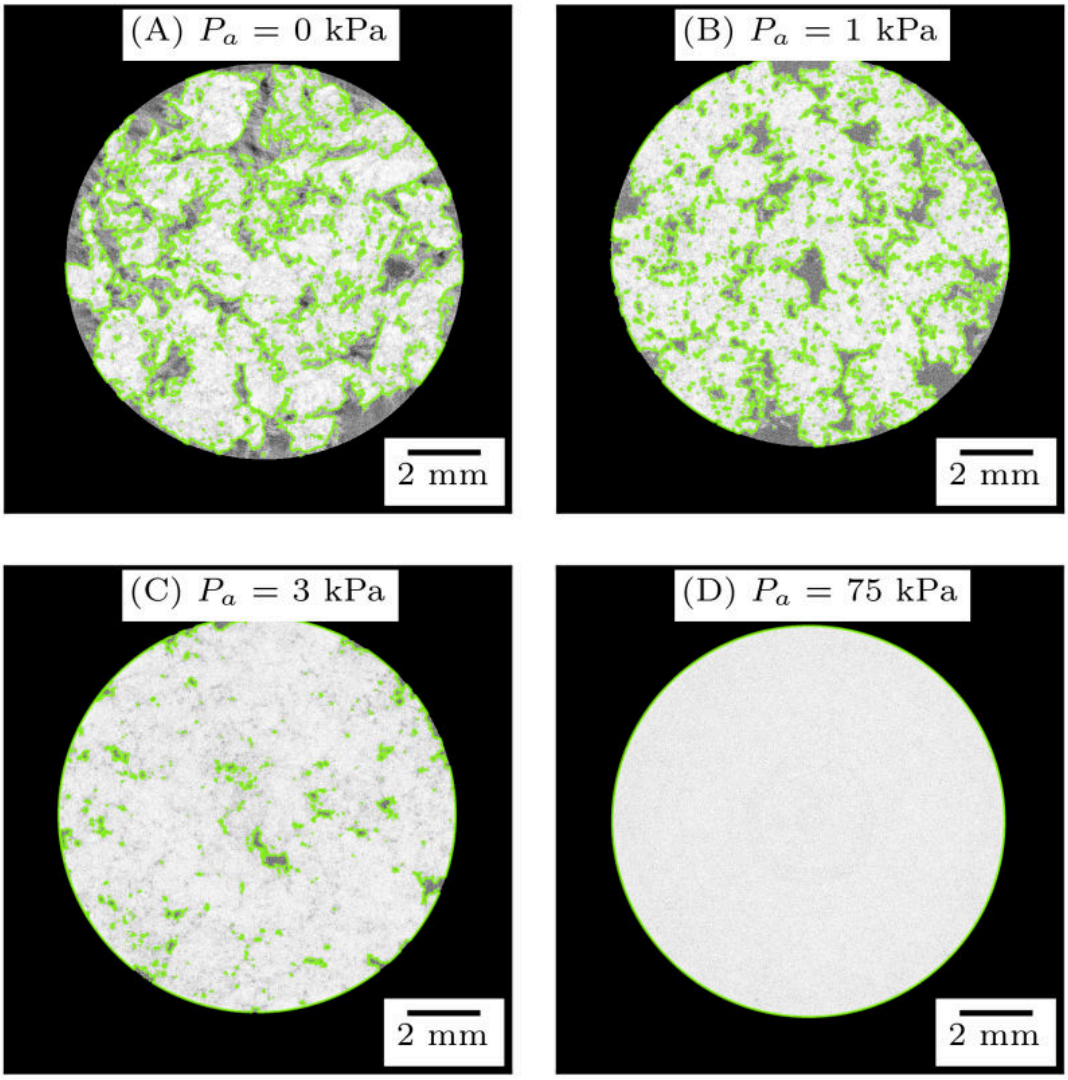

Figure 3.7: Representative grayscale micro-CT images of flocculated silica after varying levels of applied pressure, from 0 to 75 kPa. The green outline represents the boundary between the aggregate and fluid phase, which was produced by the random walker segmentation.

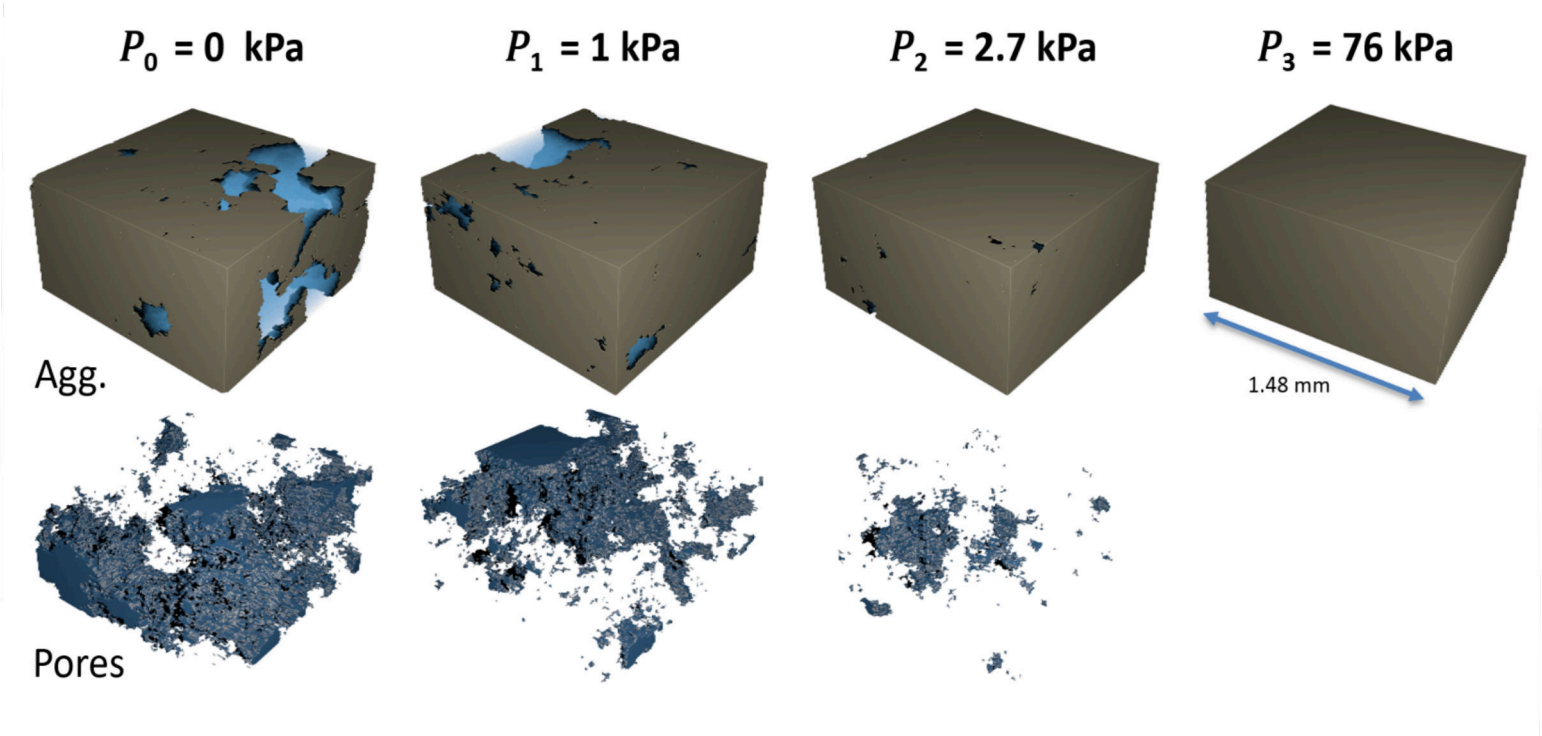

Figure 3.8: Surface mesh models generated from the binary image volumes of flocculated silica compressed by varying levels of pressure.

In Figure 3.5, the average solids volume fraction, ϕ, aggregate volume fraction, φ_{agg}, and aggregate solids volume fraction ϕ_{agg} are plotted as a function of scan height, for individual trials, and as a function of pressure, across different trials. The repeatability of P_0 and P_1 was slightly worse than at higher applied pressure due to the initially irregular packing of flocs in the sediment bed. Nonetheless, as expected, an increase in applied pressure caused an increase in the solids volume fraction, ϕ, from $P_a = 0$ to 75 kPa. In the first applied pressure step, from 0 to 1 kPa, it appears that the general increase in ϕ occurred by fluid expression rather than aggregate compression, because the aggregate solids volume fraction, ϕ_{agg}, does not change. This is supported by the increase in aggregate volume fraction, φ_{agg}, or decrease in pore volume, $1 - \varphi_{agg}$, between $P_a = 0$ and 3 kPa.

Between 0 and 3 kPa, a reorganization of the aggregate phase to a higher packing efficiency may occur but the average solids content does not increase. Increased applied pressure increases both ϕ and ϕ_{agg}, while φ_{agg} continues to increase. This slight increase in applied pressure from 1 to 3 kPa causes a large decrease in pore volume, $1 - \varphi_{agg}$, but the sediment has not fully collapsed because there is still a small fraction of pore volume remaining. Further applied pressure, from 3 to 75 kPa, causes the remaining observable pore volume to disappear. During the step 3 to 75 kPa, ϕ, increases from approximately 0.3 to 0.45, which is about equal to the change in ϕ caused by an increase of pressure from 1 to 3 kPa.

The differences in applied pressure curves at 1kPa in Figure 3.5 are likely due to differences in flocculation and sample loading. The differences are most visible in the φ_{agg} values at a height of 5 mm from the bottom of the cell, where the values were approximately 0.52 and 0.78 in the repeat trials. In this study, flocculation was carried out in a beaker with a magnetic stirrer. This method represents an improvement over less reproducible flocculation methods such as the batch jar or cylinder inversion methods (Farrow and Swift, 1996), but does not produce the regular flocculation achieved with continuous flocculation methods such as with a Couette cylinder or a turbulent pipe flow reactor (Owen et al., 2008). After flocculation, the sample was transferred by using a gentle stream of water to move the flocs into the measurement cell. Studies have modelled the impact of hydrodynamic stress (Bache, 2004) and summarized breakage mechanisms (Jarvis et al., 2005a)

on flocs, which implies for this study that it was possible some irregularity of floc size could have been caused by the manual loading of the small cell volume (3 cm^3 volume of a 5 cm^3 syringe body).

There was no apparent radial distribution of aggregate properties in the cell for φ_{agg} at lower applied pressure or for ϕ_{agg} at higher applied pressure. In the samples with no, or low, applied pressure, there could be a radial variation in the φ_{agg} or ϕ_{agg} values. For the samples compressed by 75 kPa, radial CT profiles, from the center of the cell to the edge of the cell wall were measured and the mean value of the 100 closest voxels from the center and edge were compared. The maximum variation in CT value from center to edge for all heights in the 75 kPa samples was 145, which corresponds to a change in mass density of about 0.05 g/cm^3. Distributions of local porosity in a bed of packed particles can be evaluated by changes in the mean porosity or as axially-averaged radial porosity profiles (Mueller, 2005). In the unstressed samples, with no applied pressure, there was no consistent strong trend of radial variation in mean porosity observed by measuring the void ratio of a series of concentric circles from the binary, φ_{agg}, images.

Trends in the aggregate properties as a function of height are discernible in some of the samples. The unstressed sample would be expected to have a lower solids content at the top of the sample and a higher solids content toward the bottom of the sample due to compression of the sediment bed under its own weight. In Figure 3.5 (A), at $P_a = 0$, the ϕ values decrease slightly at higher scan heights, which are closer to the top of the sediment bed. This is consistent with the self-weight compression behaviour of flocculated sediment beds. This increase in ϕ appears to be caused by an increase in φ_{agg} at lower values, possibly by the expulsion of some fluid, rather than an increase in the aggregate density, ϕ_{agg}, values. The ϕ_{agg} values are unchanged over the height of the samples which indicates that self-weight compression, in these strongly flocculated samples, does not cause an increase in ϕ_{agg}.

After the first pressure step (1 kPa), the ϕ values at the top of the sediment bed increase more than those at the bottom of the sediment bed. It appears from Figure 3.5 that this increase in ϕ is accompanied by a large decrease in φ_{agg} at the top of the sediment bed, which causes a slight

increase in ϕ_{agg} at the same height. This unequal compression of the sediment bed is possibly due a pressure gradient along the sample height, although the pore pressure was not measured in these experiments so this cannot be confirmed here. An applied pressure increase to 3 kPa appears to cause the sediment structure to collapse at the top of the sediment bed, as judged by the large reduction in φ_{agg}. An increase in applied pressure does not change φ_{agg} much, but ϕ_{agg} increases by about 0.15, which indicates that the fluid within the aggregate phase was expelled, rather than the inter-aggregate fluid that was expelled at lower applied pressures. Another explanation for this is that there was a gradient in ϕ from the top of the sediment bed (fewer flocs) therefore that part of the bed was less resistant to compression.

3.4 Conclusions

In this chapter, a novel method was described for the preparation of micro-CT calibration standards of varying mass density. The calibration was applied in a step-wise flocculated silica compression experiment to measure changes in aggregate solids volume fraction, ϕ_{agg}, average solids volume fraction, ϕ, and aggregate volume fraction, φ_{agg}, as a function of height and applied pressure.

For the calibration standards, silica suspensions were stabilized with a high concentration of APAM and used as solids concentration CT standards. An excellent linear fit for the micro-CT calibration and a good relation between the calculated and gravimetric values for ϕ was observed. The prepared standards were homogeneous, judging from the low standard deviation in the micro-CT numbers of each sample, and stable over the course of a three-hour period which was sufficient for the acquisition of the calibration scan. This approach to the preparation of micro-CT standards can be extended to other mineral systems, for example to the preparation of substitutes for moisture-absorbing natural clays. A synthetic equivalent, with the same chemical composition, could be prepared with a suitable polymer to produce a more stable standard that is resistant to swelling.

In the compression trials measured with CT, it was found that the increase in average solids volume fraction, ϕ, in flocculated sediment beds at lower applied pressures occurred as a result of fluid expression from the inter-aggregate pore space, while the increase in ϕ above as low as 3 kPa

occurs due to compression of the aggregate phase and expression of intra-aggregate fluid. These measurements and observations appear to be in line with conventional data on dewatering at low pressures, but this is the first time a detailed measurement of these mechanisms has been made in flocculated mineral sediments. The change in average solids volume fraction, ϕ, between 0 and 3 kPa is about the same as between 3 and 75 kPa, which indicates that the dewatering at very low pressures occurs mostly by reduction in the pore network, while the fluid content of the aggregates remains unaffected.

A significant increase in ϕ_{agg} only occurs once the pore network has been removed, and this requires significantly more applied force than simply expelling the inter-aggregate fluid, which is problematic for processes that start with low density flocs but hope to achieve a high density thickener underflow or as a result of self-compression in tailings ponds. Understanding these mechanisms is highly relevant to improving strategies for flocculation as a pre-treatment for solid-liquid separation by self-weight compression in a thickener or tailings pond or by applied force in centrifuge or filtration processes.

The next chapter shows how the flocs within the sediment beds of this chapter have a distinct macro-structure held together by low-ϕ boundaries. That insight will help to show that the increase in ϕ observed in low-applied pressure dewatering occurs due to floc breakage and re-organization of the sediment, and further confirms that increased ϕ, in the initial stages of consolidation, is not due to the increase in ϕ_{agg}.

Chapter 4

The macro-structure of quartz flocs

4.1 Introduction

In a dewatering process, it is often desirable that flocs have a high settling velocity (to reduce residence time) and form a sediment that exhibits a combination of high permeability and sufficient resistance to compression (to increase fluid flux). Thus, much research occurs under the umbrella term of floc structure, because such knowledge can help to explain the changes that occur to flocs during their formation, breakage or dewatering. In this study, quartz flocs were imaged with X-ray CT and a workflow for separating 3D macro-flocs into constituent sub-units was established to permit a definition of floc macro-structure in terms of the connectivity and spatial arrangement of floc sub-units.

An image analysis strategy was demonstrated for identifying the sub-units that comprise the macro-structure of medium and large sized flocs. This approach permits the spatial arrangement and connectivity of floc sub-units to be defined in terms of simple parameters and structural models. While such a detailed analysis of floc macro-structure has not been previously addressed in the literature, this knowledge is of interest because macro-flocs account for a large proportion of the total volume of population of flocs, although they are fewer in number. As a result, the breakage or re-arrangement of floc sub-units from macro-flocs is expected to play an important role in determining the response of a strongly flocculated suspension to mechanical agitation or applied

pressure.

4.2 Methods

Quartz flocs were prepared and embedded in agarose gel, then scanned with X-ray CT. Image analysis included the segmentation of flocs from the background, the segmentation of macro-flocs into sub-units, and the calculation of several statistics to describe floc shape, size and the spatial arrangement of the sub-units. Three structural models comprised of non-penetrating spheres were prepared to understand the scaling relationship between floc structure and measured properties.

4.2.1 Quartz floc preparation and embedding

The quartz flocculation method and conditions used in this study are described in Section 3.2.1. The method produced large flocs with a consistent, complete flocculation of the quartz suspensions. A 1 wt. % agarose solution was prepared with agarose LE powder (Electron Microscopy Sciences, Hatfield, PA, USA) and poured into flat-bottomed acrylic cells with 12.5 mm internal diameter, then cooled to approximately 40°C, similar to the method reported in (Droppo et al., 1996). Flocs were introduced to the agar solution by touching a small sub-sample of wet floc material to the surface of the agar. The cell was capped with a rubber stopper and submerged in a 4 °C water bath to rapidly cool and stabilize the gel. The sample cell was gently inverted during the cooling stage to ensure the flocs were well distributed in the sample cell.

4.2.2 Computed tomography image acquisition and handling

Synchrotron-source X-ray CT scans of three embedded floc samples were measured at the Canadian Light Source (Saskatoon, SK, Canada) on the Biomedical Imaging and Therapy Insertion Device beamline (BMIT-ID, 05ID-2) (Wysokinski et al., 2015). Two CT calibration scans were measured of samples that contained air, deionized water, and specimen quality quartz crystals (Ward's Science, Rochester, NY, USA). All scans were acquired with a 30 keV monochromatic beam and a 3.6 μm nominal spatial detector resolution. The raw tomograms of each scan were reconstructed to form a 3D image with UFO-KIT software (Version 0.16), a multi-threaded, graph-

ics processing unit-enabled software framework (Vogelgesang et al., 2012). Image processing and handling steps were carried out with the Python programming language (Version 3.6, Python Software Foundation) using NumPy, SciPy, and scikit-image for numerical calculations and Mayavi for 3D visualizations.

Floc segmentation

The segmentation strategy was developed to fit the data into memory ($>$ 50 GB images) and to conduct a fast, high quality segmentation of the low-contrast images. Each image volume contained 1000's of flocs, so the images were first processed slice-by-slice to identify regions that contained flocs. This step was used to mark regions of interest in the image for segmentation using the watershed transform algorithm.

A Gaussian filter was applied to de-noise the image, followed by a threshold (at a level to ensure flocs were marked but the background was not). A series of morphological operations were applied to improve the accuracy of the floc labels: a binary morphological dilation; a filter to remove small objects less than 25 voxels in size; a second binary morphological dilation; then a filter to fill holes less than 25 voxels in size. Then, the full binary image volume was re-loaded and unique objects in the image were labelled with a unique integer number. Further noise and artifact reduction was achieved by removing labelled objects that were touching the edge of the image, fewer than 5 voxels in height, or less than 100 voxels in size. While the 100 voxel size threshold eliminated many smaller flocs, by visual inspection it was found to significantly reduce the number of instances of artifacts or noise being labelled as flocs. The coordinates of the bounding box of each remaining object were determined, padded by 25 voxels, then used to crop the raw image. Finally, each floc image was re-segmented with the watershed algorithm. For this step, each floc image was input as an intensity image, with no marker image, no mask image, and using a connectivity parameter of one. The final output of this step was a set of floc intensity images and corresponding binary floc masks.

Sub-unit segmentation

Each 3D floc image was processed using a variant of the marker-based watershed transform (MBWT) to identify whether it could be separated into floc sub-units. The MBWT was applied to over-segment the ϕ-calibrated floc image, then a post-processing step was applied to selectively merge segments to produce a set of final segments (floc sub-units) separated by low-ϕ boundaries.

The MBWT proceeds by "flooding" regions of an intensity image from seed points in a marker image analogously to a watershed filling with water (Soille and Vincent, 1990; Neubert and Protzel, 2014). The intensity input was calculated from the floc mask by taking the negative of the Euclidean distance transform (EDT), where each voxel is assigned a value based on its distance to the edge of the object. The marker image input was generated from the ϕ calibrated floc image. A threshold was applied to retain the top 10 % of intensity values. This ensured that no background (agar) was contained in the marker image. Seeds (single voxels) were identified by calculating the local maxima of the marker image using a sphere-shaped structuring element (SE). By using closely spaced seeds (controlled by the SE size) and the negative of the EDT, the MBWT produces an over-segmented label image (i.e. with more segments than floc sub-units).

A post-processing step was then applied to selectively merge segments based on the average ϕ values located at the boundary between segments. Each segment in the label image may be considered a set of indices X_i, where i is a unique integer value. To identify the boundary region between segments, a morphological binary dilation of each segment, $\delta_b(X_i)$, was calculated. The set difference $X_i \setminus \delta_b(X_i)$ was then used to index the label image to extract the integer values (labels) of any neighboring segments. If, for example, X_j is a neighbor of X_i, then the set intersection $\delta_b(X_i) \bigcap X_j$ represents the boundary indices of the region between the two segments. If the average ϕ value of the boundary was above a preset threshold, segments i and j would be merged (i would be re-labelled j or vice versa). After segment-merging, the identified floc sub-units are now separated by low-ϕ boundaries. This segment-merging step also permitted calculation of the shared surface area between floc sub-units, denoted $A_{\text{int.}}$.

4.2.3 Shape and size properties

Each 3D floc and floc sub-unit was measured along its three principal axes (d_1, d_2, and d_3) and floc size, d_{mean}, was calculated according to (Jarvis et al., 2005b):

$$d_{\text{mean}} = (d_1 d_2 d_3)^{1/3}. \tag{4.1}$$

Aspect ratio was calculated from the largest and smallest axes (d_1 and d_3) according to:

$$AR = \frac{d_1}{d_3}. \tag{4.2}$$

The root-mean-square distance between sub-units in each floc were calculated according to:

$$d_{\text{rms}} = \left(\frac{1}{N} \sum_{i=1}^{N} (c_i - c_0)^2 \right)^{1/2}, \tag{4.3}$$

where c_i is the centroid position of sub-unit i, N is the number of sub-units in the floc, and c_0 is the centroid of the floc according to:

$$c_0 = \frac{1}{N} \sum_{i=1}^{N} c_i. \tag{4.4}$$

Three structural models comprised of non-penetrating spheres (representing floc sub-units) were generated to contextualize the scaling relationship between d_{mean}, AR, and d_{rms} and macro-floc structure. The procedure is provided in Section 4.4.4. Briefly, a fully compact structure was obtained with a 3D hexagonal close-packing arrangement of spheres (hexagonal close packing (HCP) 3D), a fully extended structure was obtained by the linear placement of spheres (linear packing structure (LIN)), and a structure between compact and extended was obtained by a 2D hexagonal close-packing arrangement of spheres (HCP 2D).

4.3 Results

Nearly 10 000 floc images were extracted from three ϕ-calibrated CT image volumes. Floc size, shape and structure were extracted for each floc. Medium- and large-sized macro-flocs were found to be comprised of connected sub-units that were distinctly separated by low-ϕ boundaries.

4.4 Calibration for solids volume fraction

A calibration was made between the X-ray CT signal and quartz ϕ. Two CT scans were recorded of samples that contained distilled water, air, and a quartz crystal. Figure 4.1 shows the grayscale intensity histogram of one CT calibration scan. To check the linearity of the CT response, the theoretical photon mass attenuation coefficients, μ/ρ [cm^2g^{-1}], of air, water and quartz at 30 keV were obtained from the NIST X-ray attenuation databases (Berger et al., 1999; Hubbell and Seltzer, 2004). The μ values in Table 4.1 were fitted to the grayscale intensity values of the three calibrants. A highly linear relation was obtained (r^2 = 0.999 and standard error of 0.0082) which indicated that a linear mapping between the intensity values for water and quartz could be made to ϕ values of 0 and 1, respectively.

Table 4.1: Verification of linearity between X-ray CT signal response (GS intensity) and theoretical mass attenuation values.

Substance	Mass attenuation μ/ρ [cm^2g^{-1}]	Mass density ρ [kgm^{-3}]	Linear attenuation μ [cm^{-1}]	GS intensity [10^7]
air	0.3538	1.225	0.0004334	4.42
water	0.3756	998	0.3748	4.68
quartz	0.8726	2650	2.312	5.97

4.4.1 Floc volume and solids volume fraction

Figure 4.2 shows the floc volume frequency and cumulative probability distributions for the flocs extracted from each CT scan. The collection of flocs in each 6 mm x 6 mm x 6 mm FOV may be considered a sub-sample of flocs in the agar-filled cell (which is in turn a sub-sample of the flocculated sediment), so local variations in the number and size of flocs were expected. Scan A

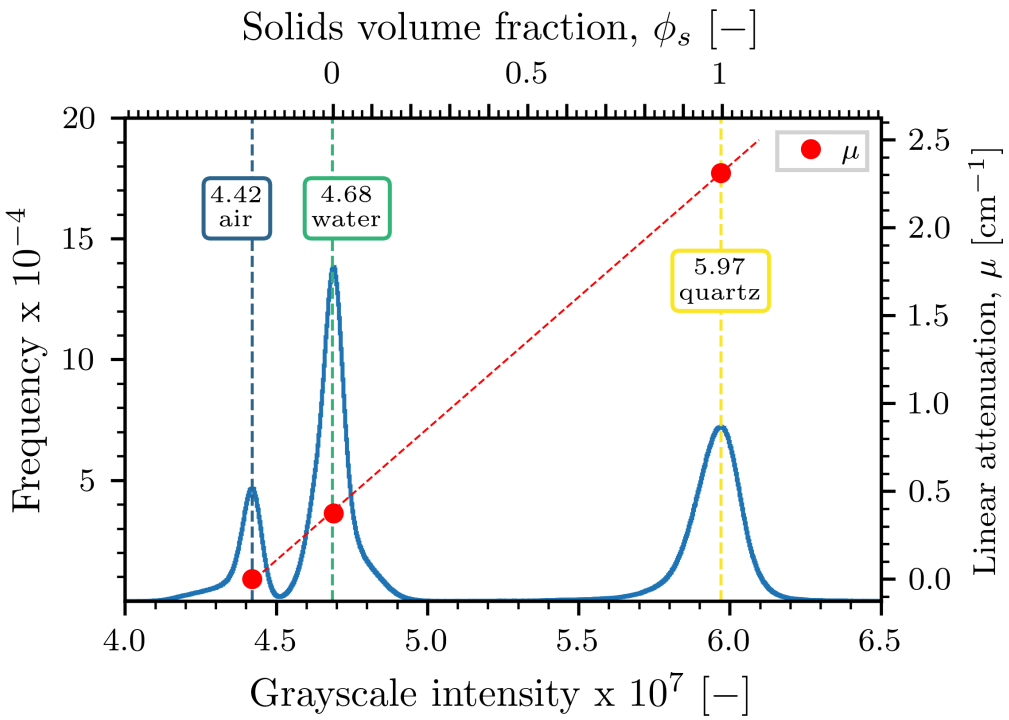

Figure 4.1: Calibration of the X-ray CT signal for quartz solids volume fraction, ϕ, using air, distilled water, and quartz crystal as calibration standards.

had more flocs (4465) that were on average of smaller volume (9 x 10^5 μm^3) compared to scan B (2713 flocs with mean volume of 14 x 10^5 μm^3) or scan C (2151 flocs with mean volume 15 x 10^5 μm^3). This could indicate that the state of aggregation in scans B and C was higher (on average), because there were many fewer flocs of intermediate size, between 1 x 10^4 μm^3 and 1.2 x 10^5 μm^3. In any case, the cumulative distributions and sample preparation were similar, so onward analyses were made by considering the floc images in the three data sets as one population of flocs produced under the same conditions.

The abrupt transition of the distributions at smaller floc size ($< 10^4 \mu m^3$), in Figure 4.2, is caused by the removal of smaller flocs during image processing. This choice was made to remove artifacts and noise, in order to retain a high quality image set of medium- and large- sized flocs. In limited cases, the objects removed could have been very large, unflocculated individual particles of the quartz sample (d_{90} = 7.4 μm), which would have an equivalent volume approaching that of the smallest flocs (about 1700 μm^3). However, such particles would be associated with high solids

concentration values because they would fill the full voxel, which was not observed in the data. A higher resolution CT (1 μm) and smaller FOV (1 mm^3) could have been used, but that would severely limit the number of medium- and large-sized flocs imaged.

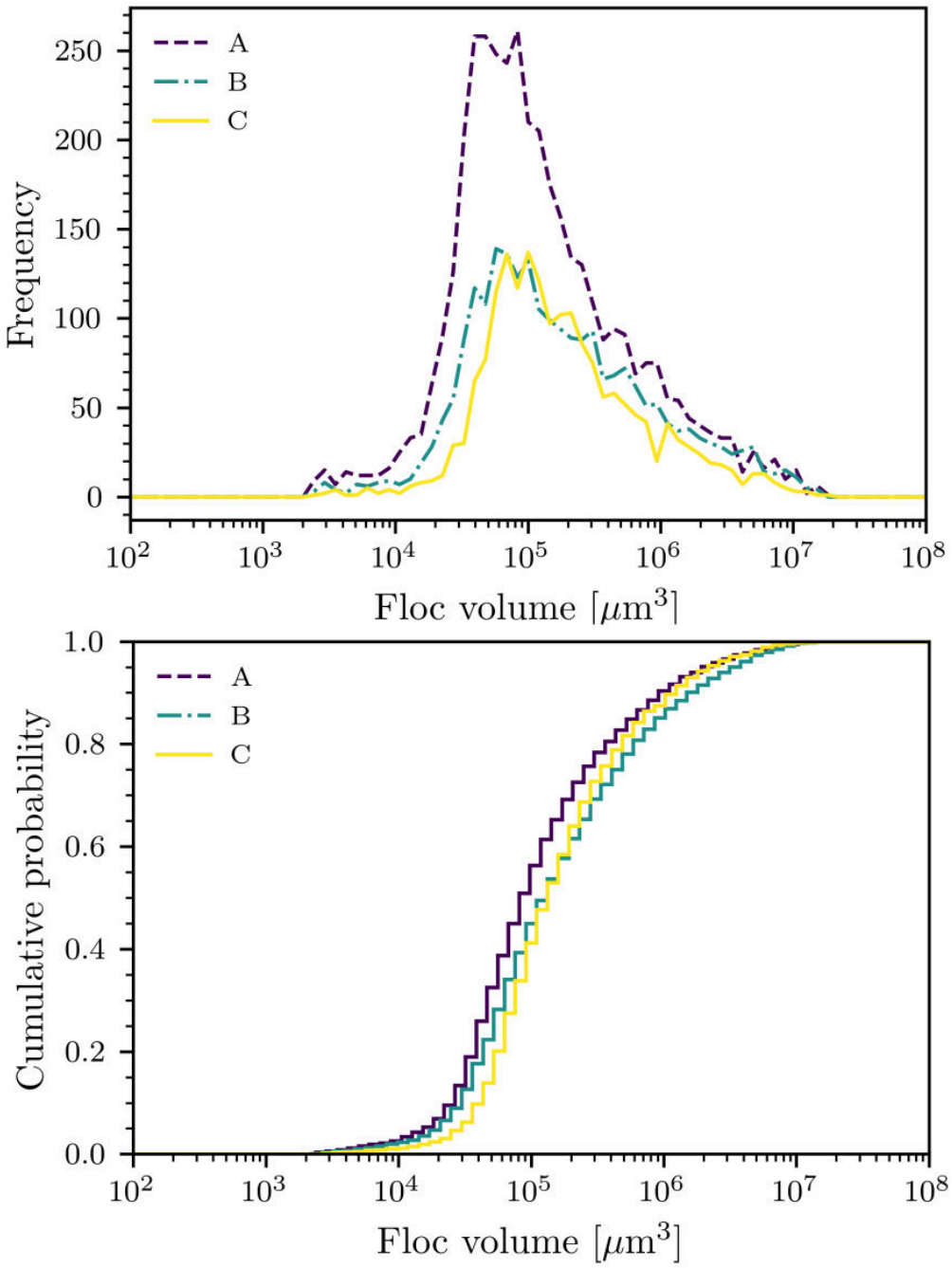

Figure 4.2: Number and cumulative size distributions for volume of quartz flocs extracted from three different X-ray CT image volumes.

Figure 4.3 shows a 2D histogram of floc volume versus ϕ. A detailed account of the ϕ-calibration for the CT images is provided in Section 4.4. The volume-weighted $\overline{\phi}_s$ value (0.21) gives a better indication of the average value in the assembly than the number-weighted mean (0.17); because, although there are far fewer very large flocs, they represent a significantly larger proportion of the total floc volume (1 floc of $10^8 \mu m^3$ = 1000 flocs of $10^5 \mu m^3$ each). The volume-weighted value (0.21) is also in good agreement with the range of values reported in Chapter 3, where the average solids volume fraction of the aggregate phase in the unstressed beds of quartz flocs was between 0.21 and 0.24.

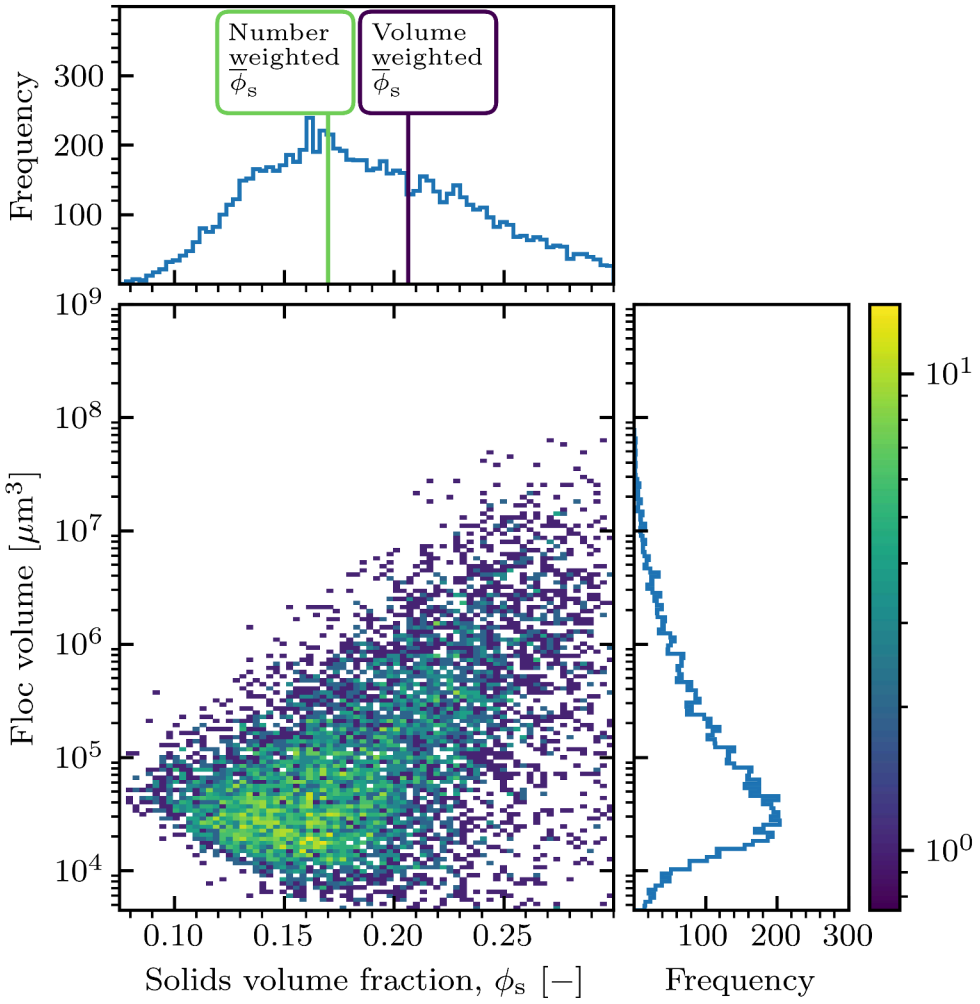

Figure 4.3: Histogram of floc volume and solids volume fraction, ϕ (composite of three data sets).

4.4.2 Floc sub-unit segmentation

Floc images were segmented to identify floc sub-units separated by low-ϕ boundaries. This approach was rationalized by descriptions of macro-floc structure in the literature: that macro-flocs are comprised of loose packing of sub-units of tightly packed particles (floc nuclei and micro-flocs). As such, the boundaries between sub-units in the macro-flocs are expected to occur at lower ϕ values. Visual inspection of the floc images in this study supported that description. While an image resolution of 3.6 μm would be insufficient to characterize the shape or structure of the primary particles used in this study (with d_{50} = 2.5), the average linear size of a single sub-unit flocs was 90 μm, as described in more detail in Section 4.4.3.

In Figure 4.4, three example flocs are shown in ϕ-calibrated and segmented images. In the ϕ-calibrated images, by the unaided eye, a gradient can be observed from low-ϕ values to high-ϕ values near the center of clusters. For 2D test images it was relatively easy to obtain a good segmentation and define a suitable set of parameters; but far poorer segmentation results were achieved with the MBWT in 3D unless careful attention was paid to the initial segmentation conditions (ϕ threshold and SE size) and application of the sub-unit merging step.

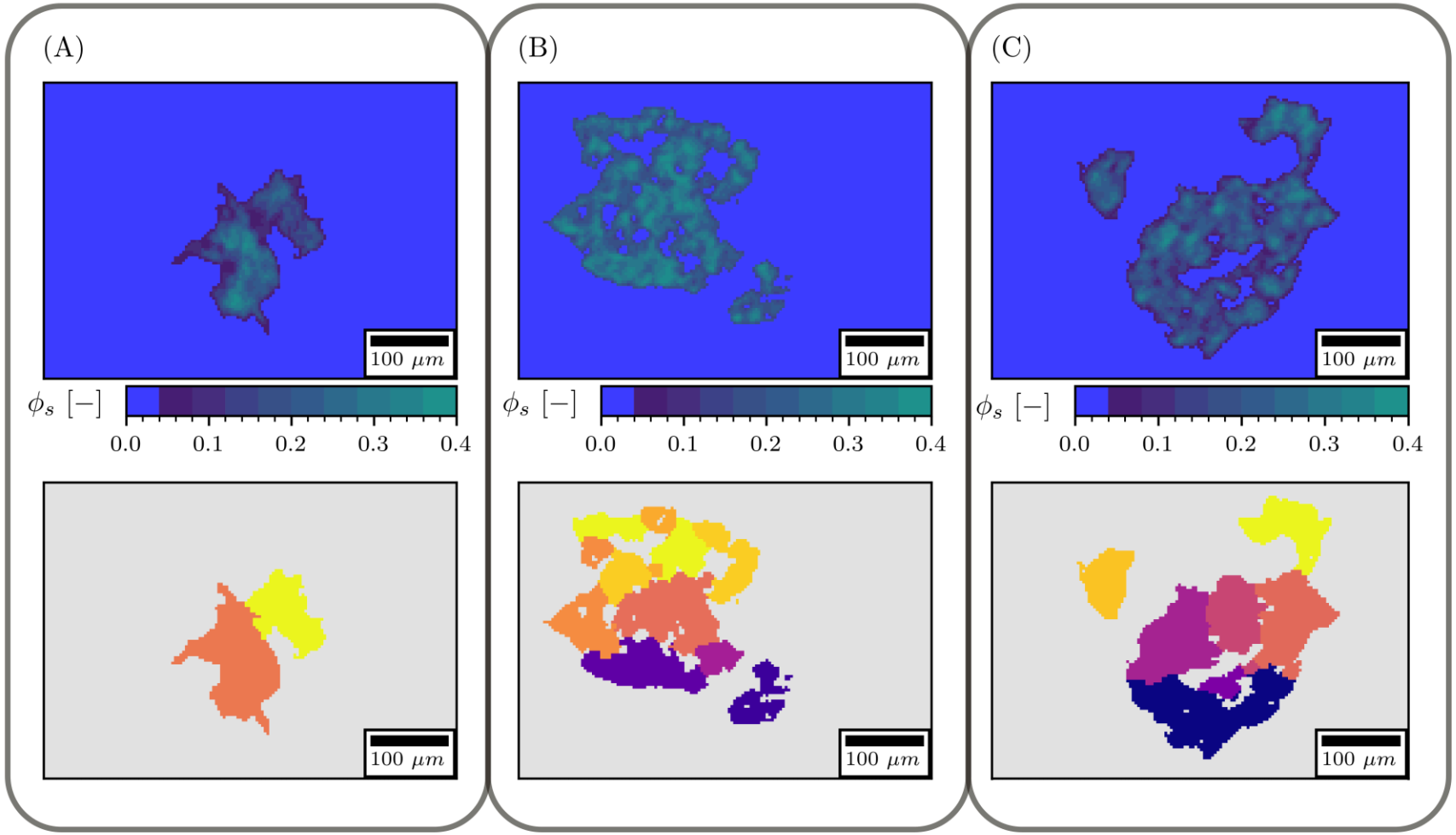

Figure 4.4: Segmentation of flocs into sub-units. A ϕ-calibrated image was used as the basis to separate regions to produce a label-map

The MBWT and post-merging steps produced a good segmentation of floc sub-units. As shown in Figure 4.5 and Figure 4.6, the initial MBWT over-segmentation identified more sub-units with a relatively higher ϕ. This initial over-segmentation ensures that all potential sub-unit edges are identified, but the merge step removes edges that are higher than the ϕ threshold. The post-merge step reduced the number of segments and decreased the average ϕ of edges between sub-units by nearly 20 %. As a conservative measure, the threshold for edge removal was set as the mean ϕ of the aggregate, which ensured that any edges identified are lower relative to the aggregate mean. In contrast, the original label map (with no sub-units merged) would be returned if the threshold was set to 1 and a completely merged label map would be returned if the threshold were set to 0.

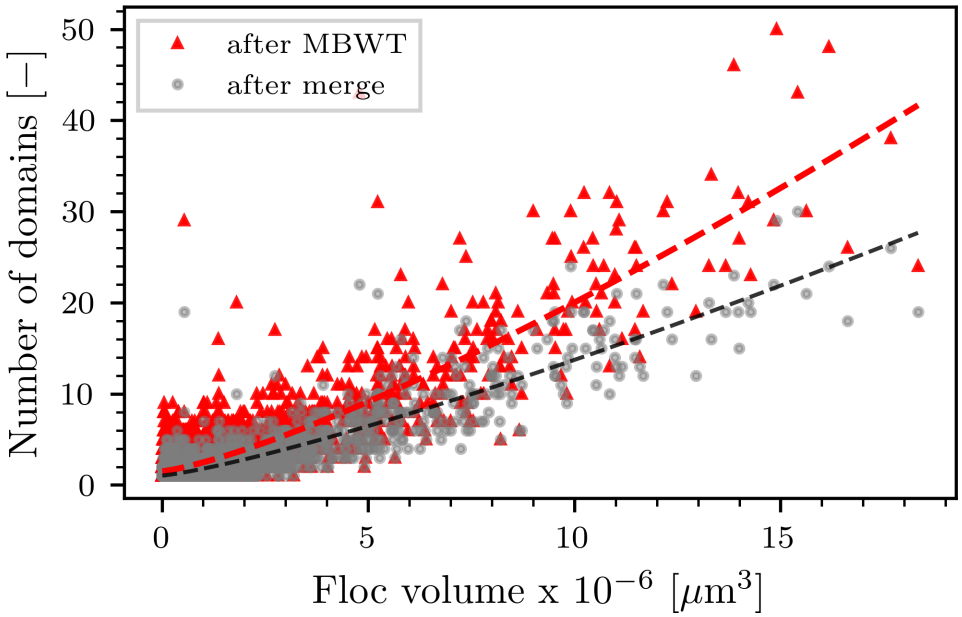

Figure 4.5: Number of sub-units as a function of floc volume before and after the merge step

In general, the number of sub-units per floc increased with floc size, which is expected from floc structure theory that larger flocs are formed by the aggregation of smaller flocs. From Figure 4.5 it is apparent that the number of sub-units merged was also a function of floc size. This implies that the largest flocs were over-segmented to a greater extent than the smallest flocs. Intuition suggests that this trend would be a function of the SE size, which controls the minimum distance between seeds in a sphere-shaped region. However, trials (not shown) with SE of various sizes

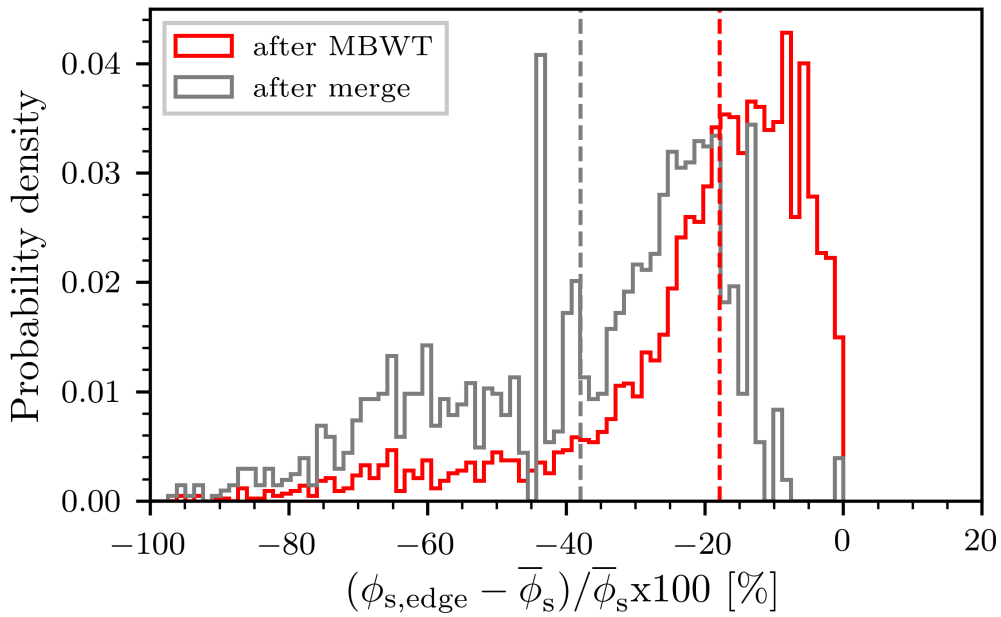

Figure 4.6: Relative ϕ values of the sub-unit edges in segmented flocs before and after the domain merge step

(radii of 10, 15, and 20 voxels) as well as a dynamically-sized SE radius (set to 1/5 and 1/10 of the floc size) indicated that the over-segmentation extent in the largest floc sizes was more or less consistent. With a suitable segmentation procedure established, the next two sub-sections deal with the relative size and connectivity of floc sub-units.

4.4.3 Floc size versus sub-unit size

The relative size of flocs and the sub-units that comprise them indicates that sub-unit size controls floc macro-structure. In Figure 4.7, each floc was broken into its component sub-units, then the volume of the sub-units in that floc were plotted against the floc volume; i.e. each domain contributes one binned value to the overall 2D histogram. For example, if a floc with volume of 1 x 10^6 μm^3 contained five sub-units each of 0.2 x 10^6 μm^3, then that floc would contribute a frequency of five to the bins that intersect at 1 x 10^6 μm^3 (floc volume) and 0.2 x 10^6 μm^3 (sub-unit volume). Although a wide range of sub-unit sizes were encountered, 99 % of all sub-units had a volume below 2.5 x 10^6 μm^3 (the average sub-unit size was around 0.17 x 10^6 μm^3). The line labelled “1 sub-unit per floc” highlights flocs that were not segmented (i.e. identified to have

one sub-unit, although they could be labelled simply as “flocs”). This indicates that many large flocs could not be segmented into multiple sub-units and they may be seen as simply very large micro-flocs.

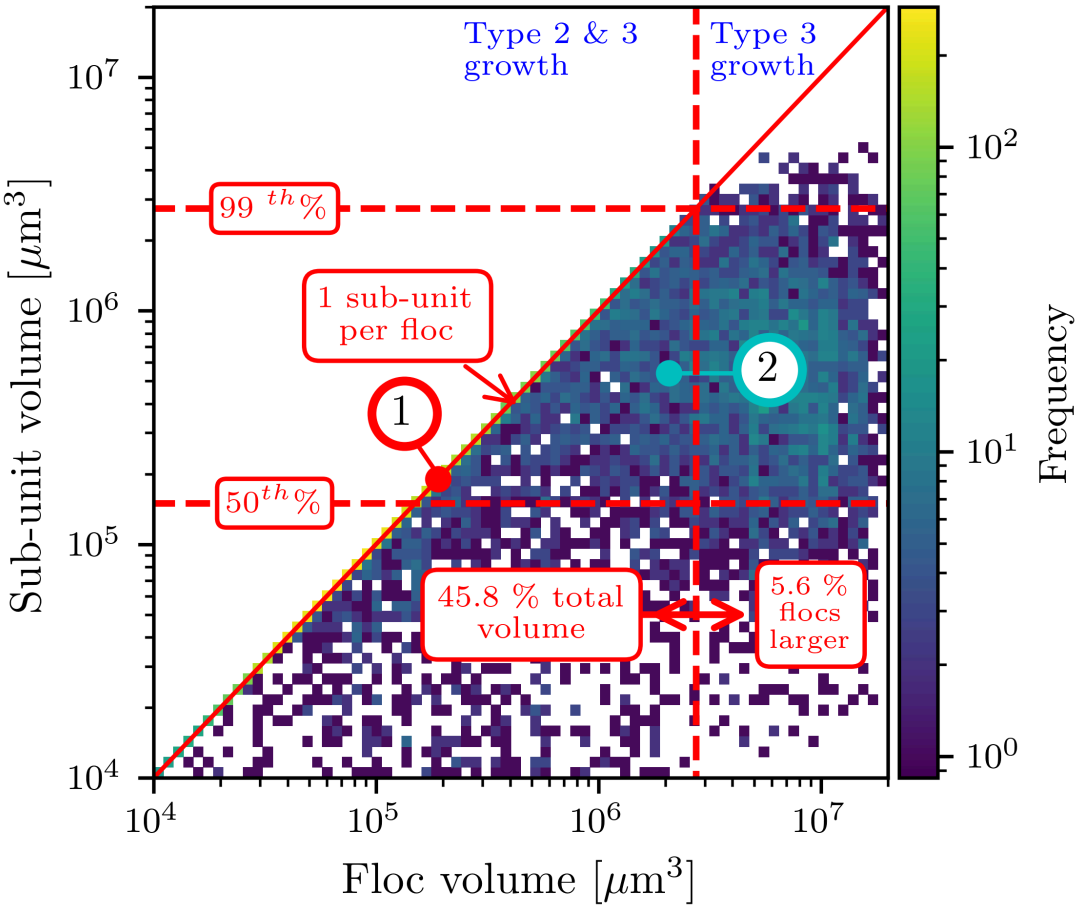

Figure 4.7: Volume of sub-units versus the volume of the floc that contains them. The label “1” indicates the mean size of single sub-unit flocs and the label “2” indicates the mean sub-unit size in flocs containing multiple sub-units.

While floc growth may occur by increased micro-floc size or aggregation of smaller flocs below 2.75 x 10 ^{6} μm^3 (red, dashed vertical line in Figure 4.7), almost all flocs are comprised of multiple sub-units above that size. The floc growth regime above 2.75 x 10 ^{6} μm^3 is thus labelled as Type 3, which occurs by the aggregation of flocs (sub-units), whereas below this size, floc growth may occur by the aggregation of micro-flocs or floc nuclei (Type 2 or Type 3 growth). The aggregation of primary particles, Type 1, is not shown. The average particle size in the quartz sample (2.5 μm)

is smaller than the CT image resolution used in this study (3.6 μm), so it would not be possible to analyze clusters comprised of only a few particles. In any case, clusters of that size were removed during image pre-processing.

In Figure 4.7, flocs may be grouped into single and multiple sub-unit flocs. The average size of single sub-unit flocs was about 0.2 x $10^6 \mu m^3$ (at point 1 in red) while the average sub-unit size in multiple sub-unit flocs was 0.6 x $10^6 \mu m^3$ (at point 2 in cyan). In terms of a linear size (Equation 4.1), the average size of single sub-unit flocs was 90 μm while the average size of multiple sub-unit flocs was 200 μm. This difference can be seen more clearly in Figure 4.8, where the single- and multiple sub-unit flocs have been grouped into separate histograms.

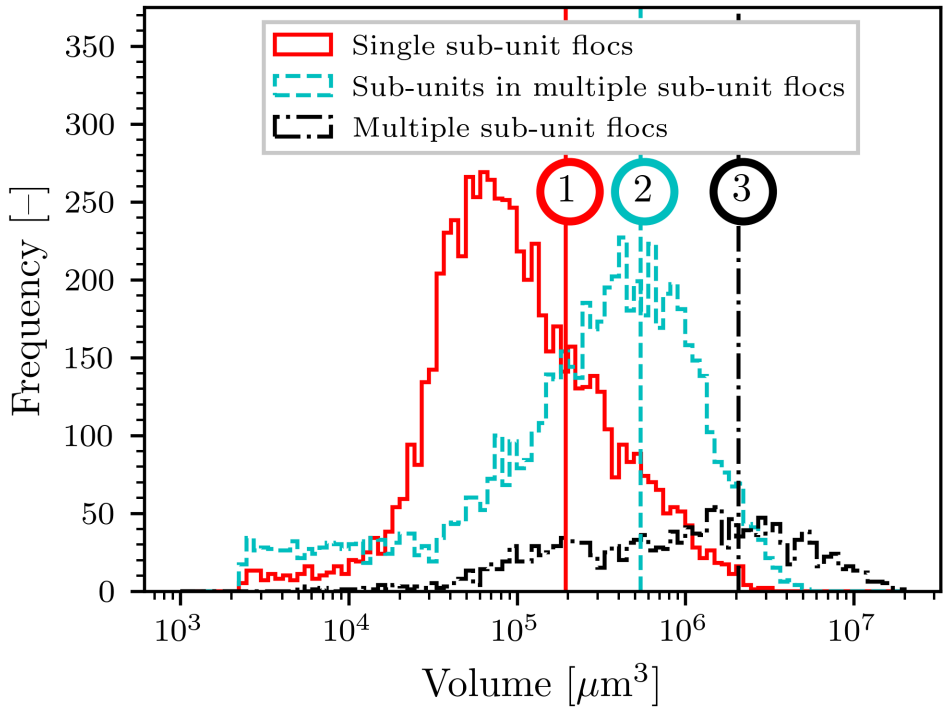

Figure 4.8: Domain volume distribution for single- and multi-domain flocs.

This difference suggests that the largest flocs in Figure 4.8 (point 3 in black) are more likely to be formed by the aggregation of fewer, larger sub-units than by many, smaller sub-units. This could be explained by the probability of collision during the aggregation process. Initially, large sub-units may be more likely to collide, and thus more likely to aggregate into even larger flocs. Growth will be counteracted by breakage at a certain point, so a maximal floc size is also observed

at almost 20 x $10^6 \mu m^3$. Moreover, while the largest flocs ($>$ 2.75 x 10^6 μm^3) represent only 5.6 % of the floc population by number (refer to Figure 4.7), they account for 54.2 % of the total floc volume.

4.4.4 Arrangement and connectivity of sub-units in macro-structure

Floc structure was examined in plots of d_{rms}, AR, and $A_{\text{int.}}$ versus d_{mean} in the context of three model structures comprised of spheres in point contact.

Model packing structures

Model structures comprised of uniformly sized, non-penetrating spheres were used to understand the scaling relationship of various floc properties with floc size and number of domains.

Three structures were considered that represent a range of form factors. A fully extended structure was modelled by the linear placement of spheres, LIN, which was constructed by sequentially placing touching spheres on a straight line. A fully compact structure was modelled by placing spheres in a 3D arrangement on the coordinates of a hexagonal close-packing structure (HCP 3D). A planar structure, (HCP 2D), representing a form factor between fully open and fully compact, was formed by placing spheres on a plane on the HCP coordinates in 2D.

The coordinates of the HCP structure are:

$$\begin{bmatrix} 2i + ((j+k) \bmod 2) \\ \sqrt{3}\left[j + \frac{1}{3}(k \bmod 2)\right] \\ \frac{2\sqrt{6}}{3}k \end{bmatrix} r_0, \tag{4.5}$$

where i, j, and k are the indices starting at 0 for the $x-$, $y-$ and $z-$ coordinates, mod is the modulus operator, and r_0 is sphere radius. A grid of available positions in 3D is generated by inputting a range of sequential integer values for i, j and k, whereas to produce the planar HCP 2D structure, $k = 0$. In both HCP structures, the first sphere was added to the HCP structure at [0,0,0], with the centroid c_0=[0,0,0]. Then the distances between c_0 and the available positions in the HCP grid were calculated. The position that corresponded to the smallest distance to c_0 was added to the

HCP structure, and c_0 was recalculated. In this way, the structures grown with a minimum root-mean-square distance, d_{rms} using Equation 4.3, between the spheres. The first five growth steps of each structure are shown in Figure 4.9.

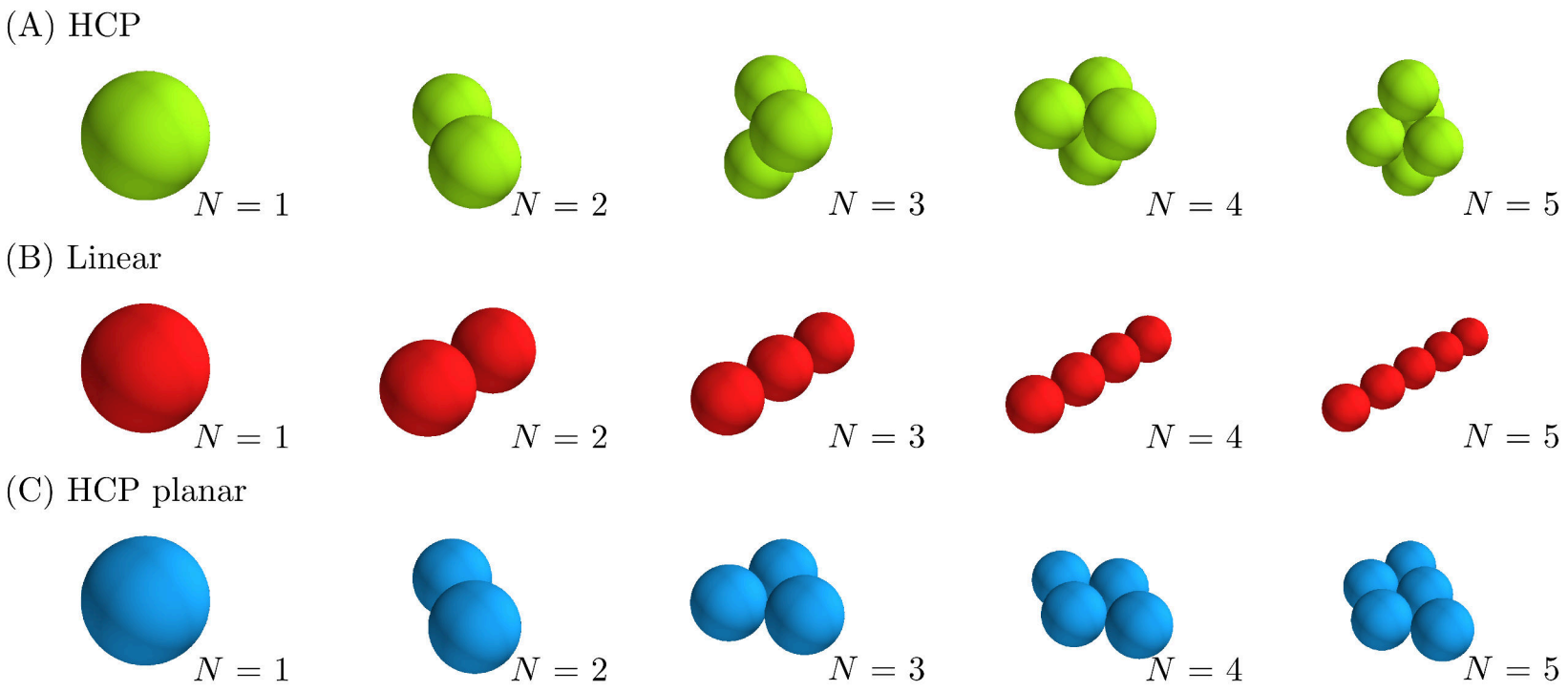

Figure 4.9: The first five growth steps of three model structures comprised of equally-sized, non-penetrating spheres in 3D: the hexagonal close-packed (HCP), planar HCP, and linear structures.

After each growth step, the following properties of the structure were calculated. Root-mean-square distance between spheres and the centroid (d_{rms} with Equation 4.3), size of the structure (d_{mean} with Equation 4.1), and aspect ratio of the structure (AR with Equation 4.2). In Figure 4.10, the scaling of these properties by number of spheres (N) and structure size (d_{mean}) is shown for spheres of unit-size (i.e. $r_0 = 1$ in Equation 4.5).

Application of models to floc structure

The trends in Figure 4.10 may be scaled by adjusting the sphere radius, r_0, to account for difference in sub-unit size. For example, in the case of analyzing the spatial arrangement and structure of domains in a floc, r_0 may be set to the average domain size to provide an an estimate of how the properties of an equivalent HCP 3D, HCP 2D or LIN structure will scale compared to the properties measured from the domains within a floc.

Figure 4.11 shows several representative flocs with d_{mean} of about 250 μm and with varying d_{rms}, AR, and N. Those flocs were selected to compare the properties of flocs with a more extended structure to flocs with a more compact structure. Although the properties of these categories overlap, the more extended structures tend to have a higher shared surface area, $A_{\text{int.}}$, and larger d_{rms}, while the more compact structures tend to have a lower $A_{\text{int.}}$ and smaller d_{rms}.

While a model system of spheres cannot represent the varied nature of irregular floc structures, the approach permits an intuitive understanding of how changes in the measured properties relate to changes in floc structure. By using the average sub-unit size from the floc measurements (90 μm) as the sphere size (r_0) in the models, it is possible to determine how d_{rms}, AR, and N with d_{rms} will scale with floc size for different structures. In Figure 4.12, three structures with 20 spheres each are shown, in order of decreasing compactness: HCP 3D, HCP 2D, and LIN.

In Figure 4.13, d_{rms}, AR, and N were plotted against d_{mean}. For a constant sub-unit size, smaller d_{rms} and lower AR values indicate a compact structure, whereas larger d_{rms} and higher AR values indicate a more open structure with domains further from the core, although the scale of the trends in these two properties with d_{mean} differ. For this reason, it is helpful to place these trends in the

context of the model structures.

From Figure 4.13, it is apparent that the majority of flocs follow the HCP 3D model line in A and B. This indicates that these flocs tends toward a more compact structure, although the average aspect ratio was about 1.5, which indicates they are somewhat elongated. About 25 % of flocs have an aspect ratio between 2 and 3, with an increased d_{rms}. However, the d_{rms} values are broader at smaller floc sizes but tend toward the HCP 3D trend line at larger floc size ($> 500\ \mu$m). A similarly decreasing trend in *AR* is also observed over the same floc size range. These changes indicate that the structure of smaller flocs is on average more variable, whereas large flocs tend to have a more compact structure. One explanation for this trend is that larger flocs could have undergone more breakage and restructuring events, which was observed by Spicer and Pratsinis (1996) to produce less open, more regular structures as a result of shear-induced breakage and restructuring.

In Figure 4.14 the total and mean area shared by sub-units, $A_{\mathrm{int.}}$, are plotted as a function of floc volume. The mean $A_{\mathrm{int.}}$ value is the average surface area between sub-units in a floc. Note that only flocs that contained two or more sub-units were included in the analysis, so this plot reflects the trend in growth of the macro-floc by sub-unit aggregation. The structures of model spheres cannot be used to interpret these trends as spheres in point contact, by definition, have no shared surface area.

While the total $A_{\mathrm{int.}}$ increases with floc size in a well-defined power law relationship, the mean $A_{\mathrm{int.}}$ (fitted with a logistic growth model) plateaus around a floc volume of 1.5 x 10^6 μm^3. This plateau occurs at a slightly lower value than the average sub-unit volume in flocs that contained multiple sub-units in Figure 4.7 (2 x 10^6 μm^3). This suggest that the increase in total $A_{\mathrm{int.}}$ occurs by the addition of similarly sized sub-units with a similar shared surface area.

Growth rate of $A_{\mathrm{int.}}$ (total and mean) is expected to be a trade-off between sub-unit size and floc shape. A larger sub-unit size would push the logistic growth curve to the right (i.e. V_0, the mid-point of the growth region would be larger), while a floc with a more extended structure would be expected to have more tenuous connectivity, with fewer sub-unit neighbours touching and a lower mean $A_{\mathrm{int.}}$.

4.5 Discussion

An image segmentation workflow was established to permit the analysis of quartz macro-floc structure and connectivity in terms of the number and relative size of sub-units, and by assessment of trends in AR, d_{rms}, and $A_{\text{int.}}$ with d_{mean}. This development supports and provides a direct quantification of the top-level in a multi-level floc structure described in the literature. Application of this knowledge helps to explain the response of the compressive dewatering of a flocculated quartz suspension, described in Chapter 3.

4.5.1 Sub-unit segmentation and analysis

The MBWT was applied at two stages: to separate flocs from the background, then to separate sub-units within individual flocs. The second MBWT stage (MBWT over-segmentation and sub-unit merging) differentiates the current approach, whereas the first MBWT stage in this study was similar to that used by Sharma et al. (2017) to segment the floc and water phases in the images. Other strategies applied during the development phase of this study did not yield such good results, including those based on: the random walker algorithm, WEKA segmentation (CPU-based machine learning), and holistically-nested edge detection (GPU-based machine learning).

The method used by Pashminehazar et al. (2018), to separate sub-units within maltodextrin agglomerates is conceptually closer to the second stage MBWT employed in the current study. In Pashminehazar et al. (2018), it was evident that the agglomerates were comprised of more extended structures of sub-units than those observed in this study. As such there was a lower shared surface area and the direct application of the MBWT would produce a high quality segmentation. In this study, the flocs were more compact with more shared surface area between sub-units and the image intensity gradients between sub-units were weak. These factors cause the marker image and EDT inputs to be more sensitive to the parameters used and to be more prone to poor segmentation results.

Floc structure and connectivity was assessed by the relative sizes of sub-units within flocs, and by trends in AR, d_{rms}, and $A_{\text{int.}}$ with d_{mean}. Perhaps the structural models of uniformly sized

spheres oversimplify macro-floc structure (e.g. sub-units measured in this study had a wide variety of shapes and sizes), but they do permit a means of identifying the expected trends (in the absence of related studies) in the measured parameters versus floc size.

Bushell et al. (2002) described the calculation of fractal dimension using micro-flocs as the primary length scale (rather than the primary particles). However, the micro-floc sizes described therein (10 to 100 μm) suggest that those authors were discussing what are referred to as floc nuclei or flocculi in this paper, which are an order of magnitude smaller than the floc sizes assessed here (100 to 1000 μm range). In this size domain, the formation of macro-flocs by sub-unit aggregation is likely controlled to a greater extent by hydrodynamic forces, rather than surface forces, so the application of fractal scaling on the scale of the sub-units in the quartz macro-flocs was avoided.

4.5.2 Implications for floc structure and dewatering

The results here demonstrate that medium- and large-scale quartz flocs have a macro-floc structure which results from the aggregation of smaller flocs or sub-units. Although sub-unit size varied significantly between flocs, analysis of the relative sizes of sub-units within the flocs (Figure 4.7) permitted a distinction between growth by sub-unit aggregation from growth by mixed micro-floc and sub-unit aggregation. Interestingly, the largest flocs (i.e. the 6 % by number above 2.5 x $10^6 \mu$m) represented a significant 54 % of the total volume in the flocs measured. This upper limit of floc size likely corresponds to the tail of the size-density relationship demonstrated by Klimpel and Hogg (1986). The structure of flocs in that size range were assumed by Klimpel and Hogg to be strongly affected by their prior growth history where multiple aggregation and breakage events lead to flocs comprised of a wide distribution of sub-unit sizes.

Floc macro-structure is expected to have a significant effect on downstream dewatering treatments. For example, rapid changes in the solids concentration of flocculated suspensions are observed to occur at low applied pressures (i.e. during the test onset) in filtration (de Kretser et al., 2001) and compressive yield strength tests (Usher and Scales, 2005). In Chapter 3, the average ϕ of the aggregates was around 0.21 (similar to the values in this Chapter), but the average bed

ϕ was much lower. At low applied pressure, increases in the bed ϕ occurred without an increase in aggregate ϕ. That change may be attributed (based on the results here) to increased packing efficiency attained by breakage of the floc macro-structure. This conclusion is supported by the work of Jarvis et al. (2005b), where it was determined that floc breakage occurs by large-scale fragmentation into smaller pieces (referred to as sub-units here) without an increase in primary particle concentration. Further, this is in agreement with the commonly held view that the floc macro-structure is weak, relative to the lower levels of floc structure, which are characterized by the stronger bonds that occur between the polymer and primary particles (Vold, 1963; Klimpel and Hogg, 1991). Thus, the macro-structure dominates the dewatering behaviour of large flocs during the initial stages, at low applied or experienced pressures. At higher applied pressure, dewatering is still controlled by the primary particle concentration and compression behaviour of the floc sub-units.

The concept of floc macro-structure also supports explanations of the throughput improvements achieved in real thickeners due to aggregate densification versus theoretical predictions (Zhang et al., 2015; Spehar et al., 2015). In Section 4.4.4 it was noted that floc structure was affected by the shared surface area between sub-units in the macro-floc structure. Assuming that the strength of the floc macro-structure is related to the amount of shared surface area between sub-units, extended flocs would be weaker and have a lower packing efficiency. In contrast, compact flocs should pack more efficiently and be stronger, because there is more shared surface area between their sub-units. While these changes may not affect the ultimate solids concentration (at very high applied pressures), the results suggest that modification of the floc macro-structure (by control of the chemical and hydrodynamic conditions of floc formation) could be a strategy to tune the compression response of a networked bed of flocs at low applied pressures.

4.6 Conclusions

An image analysis workflow was described for extracting the macro-structure of quartz flocs from X-ray CT images. The key difference in this workflow, compared to previous reports, was the

initial over-segmentation of floc sub-units followed by sub-unit merging to ensure a physically realistic result; i.e. of sub-units separated by low ϕ boundaries. The arrangement and connectivity of macrofloc structure was then described using simple parameters, including d_{rms}, d_{mean}, $A_{\text{int.}}$, and AR, which permitted a comparison with model structures comprised of solid spheres.

Although a wide range of sub-unit sizes was observed, a limiting size was identified, beyond which flocs are formed predominately by the aggregation of smaller sub-units. As a result, there were only a few very large flocs (> 2.5 x 10^6 μm^3) that represented a significant amount of the total floc volume (54 %). The flocs in this study were observed to be relatively compact and characterized by a large shared surface are between sub-units in the macro-structure. It should be noted that these sizes and structural characteristics are specific to the system studied and are likely related to the type of primary particles and conditions of aggregation. A comparison with Chapter 3 indicated that the floc macro-structure was relatively weak compared to the lower levels of floc structure, which are dominated by the bonds between the polymer and primary particles.

Further steps in this work would be to produce flocs with varying macro-structure by control of the chemical or hydrodynamic conditions of floc formation and to study the flocs at higher X-ray CT resolution. The latter would permit a segmentation of macro-structure in smaller floc sizes that were filtered out of images in this study due to a resolution limitation. Additionally, working at a higher resolution could permit the differentiation of floc nuclei within micro-flocs using the same technique reported here. These steps, in addition to the results of the current study, would help to provide a more complete picture of floc macro-structure and its role in the dewatering response of flocculated suspensions.

This chapter provided strong evidence that the quartz flocs studied exhibit a fragile macro-structure that could be easily broken. As such, a it is likely that the initial consolidation of a sediment bed comprised of such flocs would occur due to breakage and re-organization of the flocs. In Chapter 5, that argument is made with support from the results in the current chapter and Chapter 3, in light of the dominant theory of sediment consolidation used to describe the thickening process.

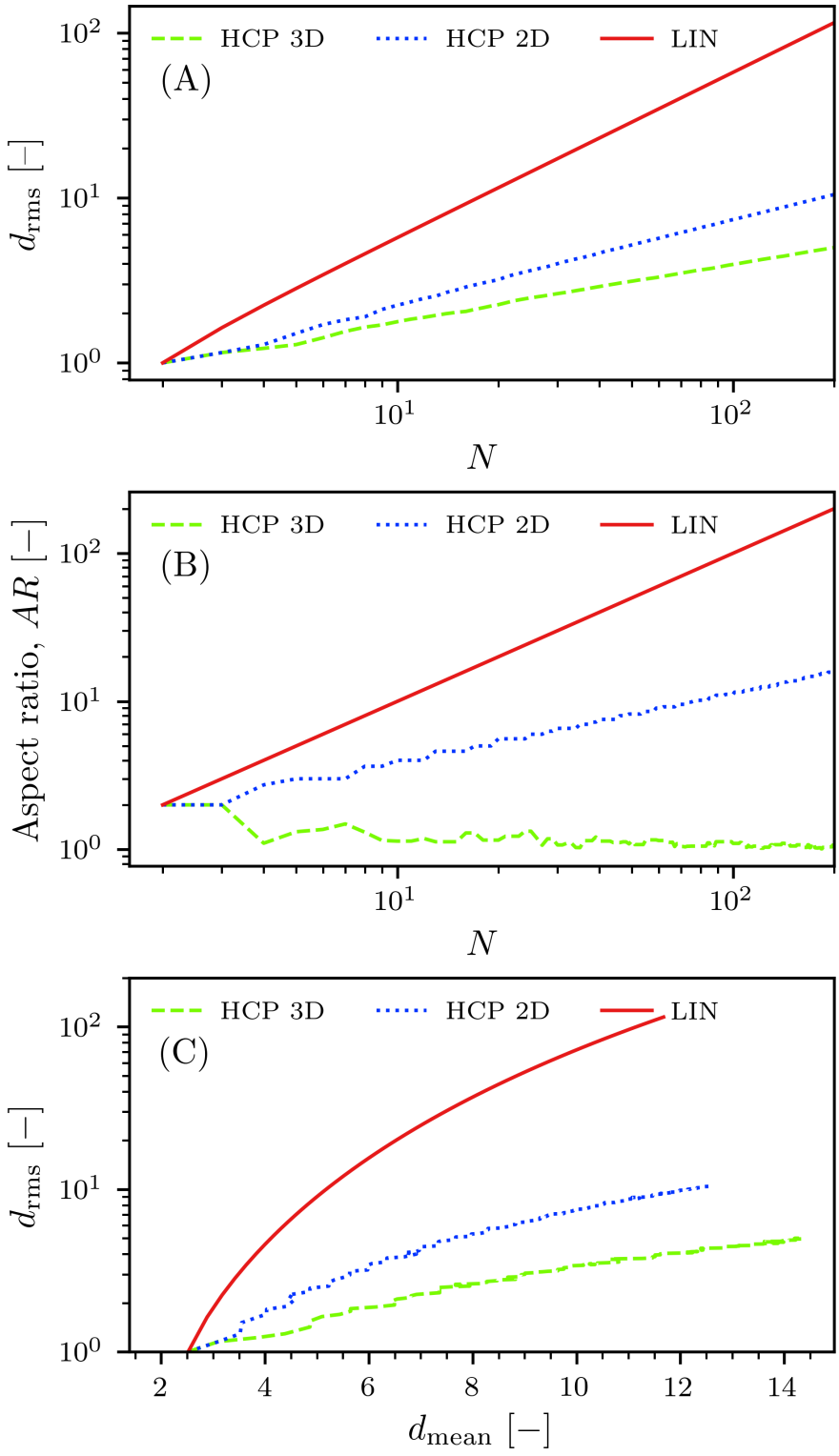

Figure 4.10: Scaling relationship between number of spheres (N) and the root-mean-square distance between spheres and (A) the centroid (d_{rms}), (B) the aspect ratio (AR) and (C) the mean size (d_{mean}) for three structures: a 3-dimensional hexagonal close packed structure (HCP 3D), a 2-dimensional or planar HCP structure (HCP 2D) and a linear structure (LIN).

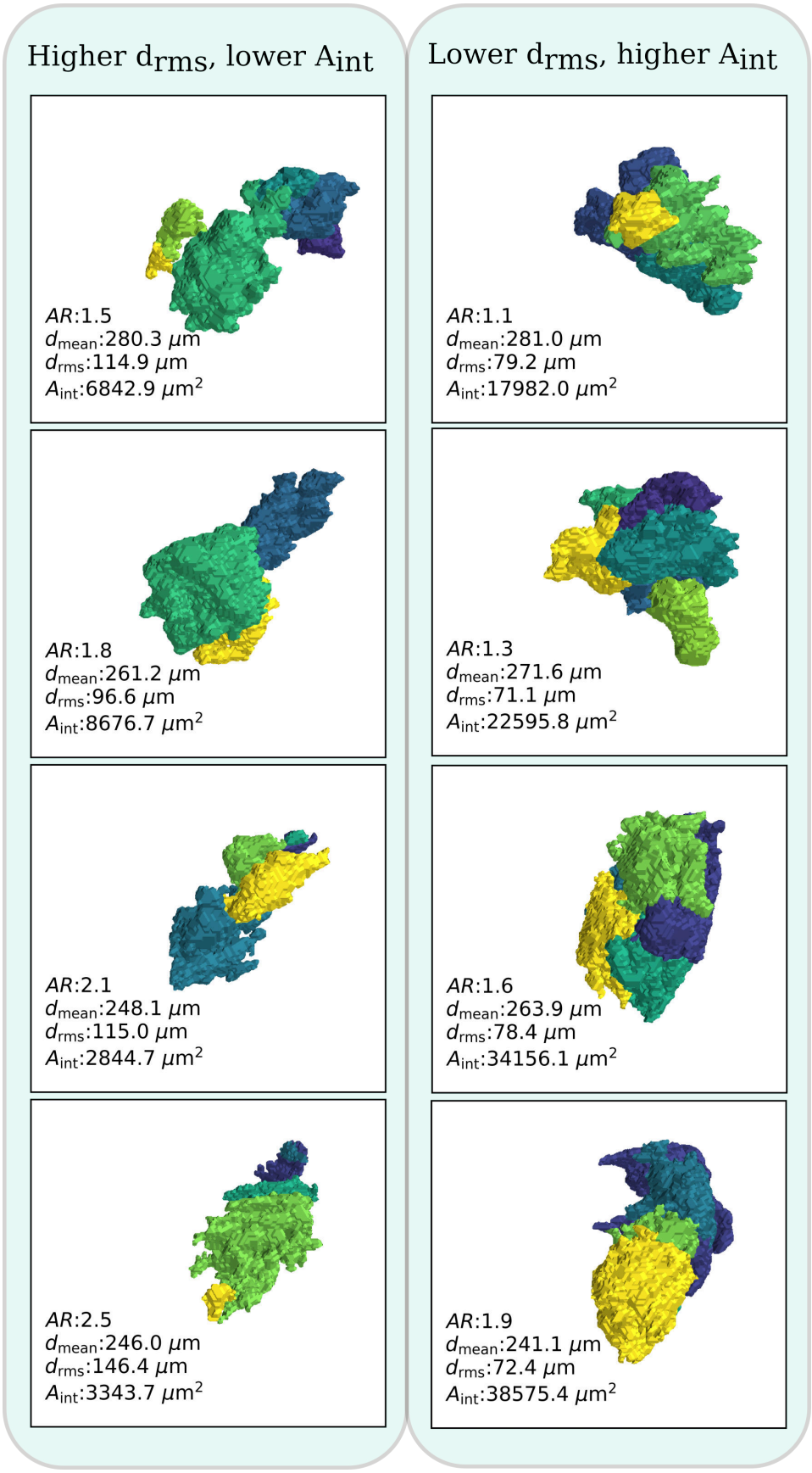

Figure 4.11: Representative flocs of constant d_{mean} (about 250 μm) with varying d_{rms}, AR, and $A_{int.}$.

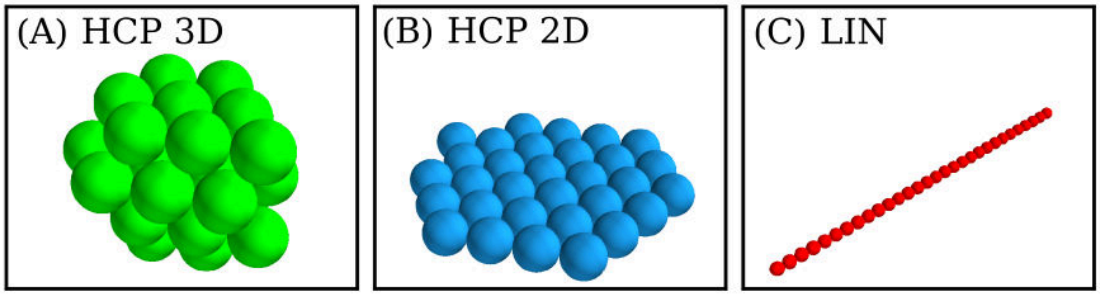

Figure 4.12: Three model structures comprised of 20 spheres each.

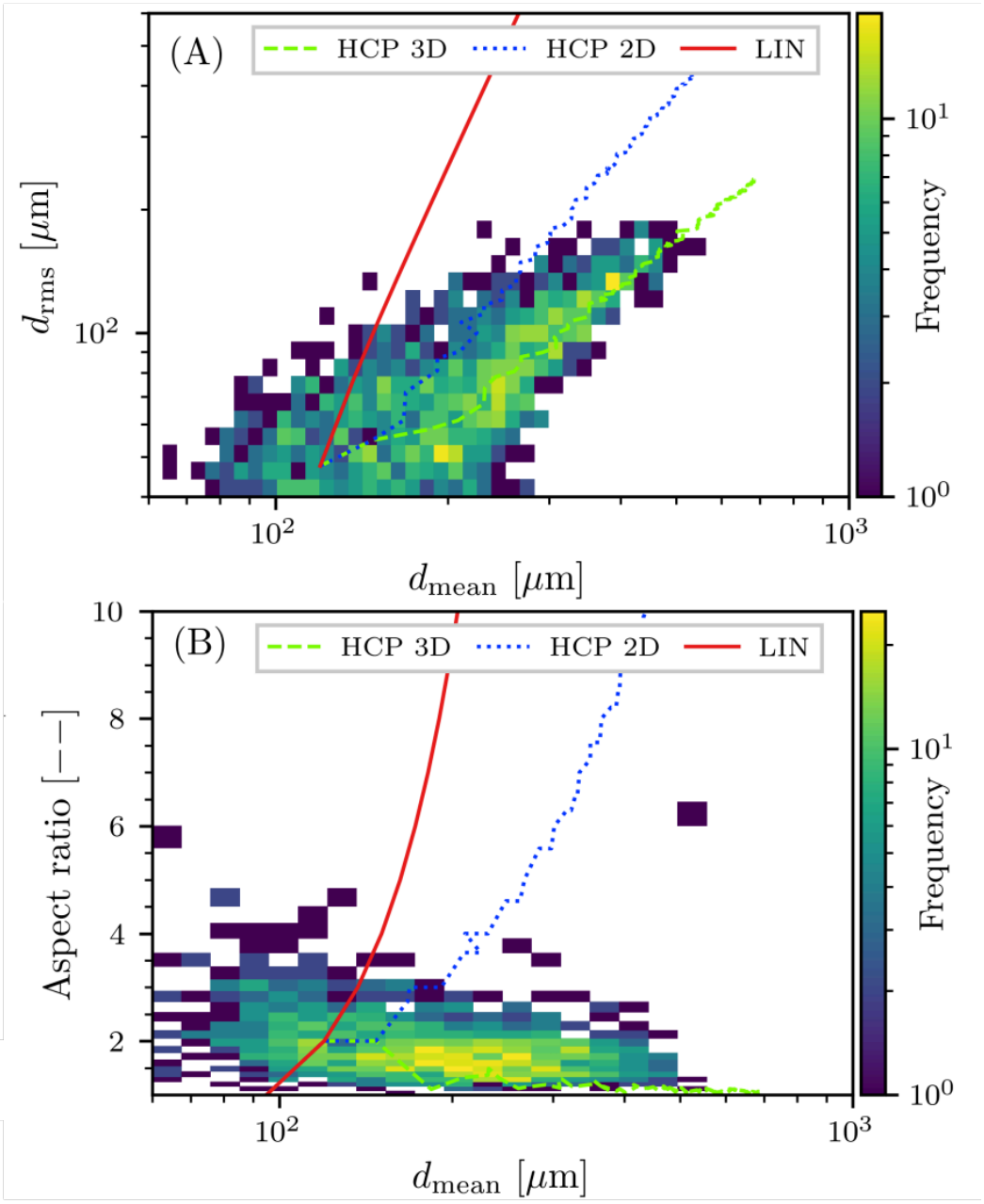

Figure 4.13: Number of nearest neighbours and intra-floc domain surface area as a function of floc volume

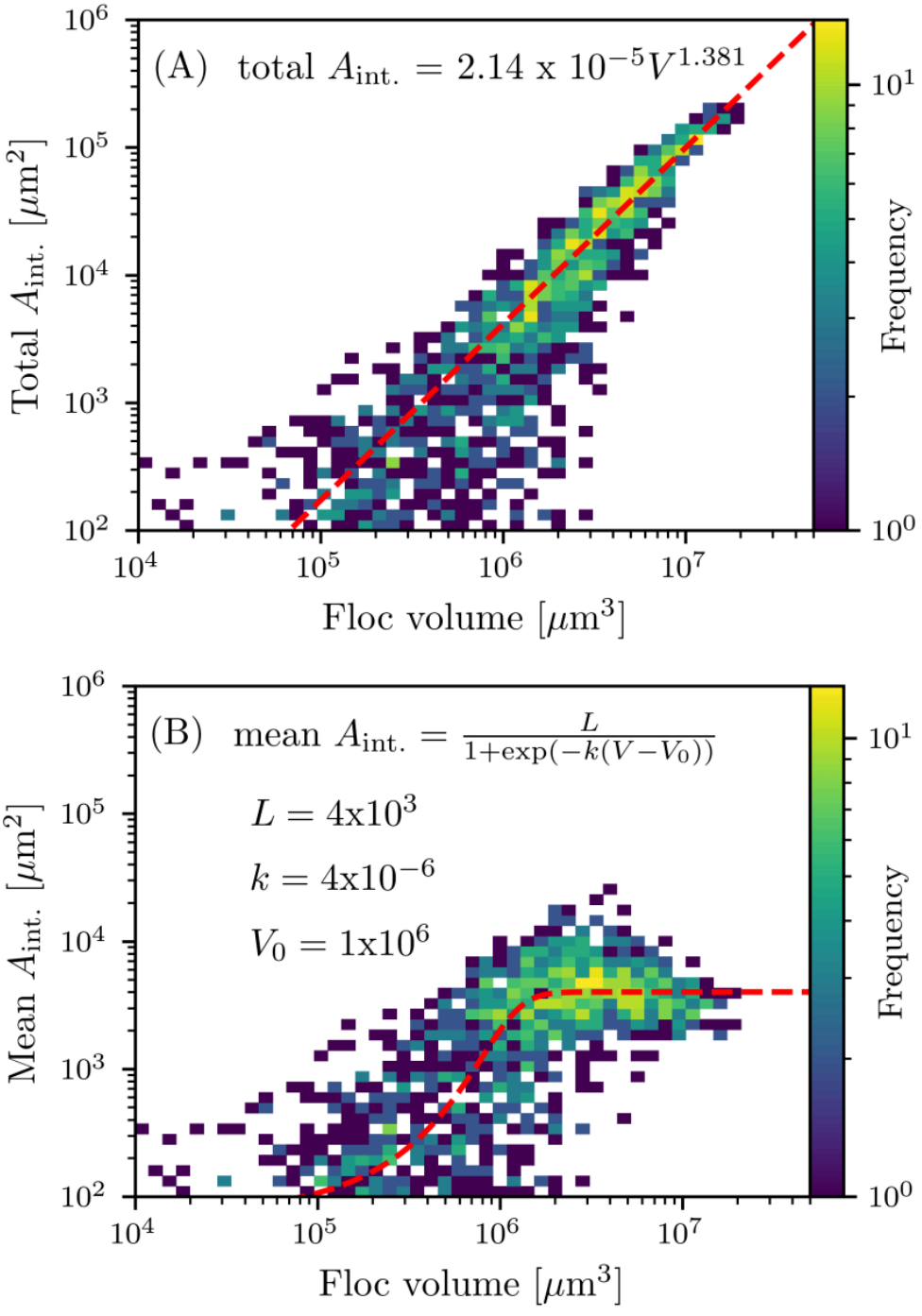

Figure 4.14: Total and mean surface area, $A_{\text{int.}}$, shared between sub-units as a function of floc volume.

Chapter 5

A floc structure perspective on sediment consolidation in thickened tailings

5.1 Introduction

This chapter demonstrates that aggregate breakage and structural re-organization during mixing in the thickening process can account for some of the experimentally measured changes in solids volume fraction that have been until now attributed to aggregate densification in the literature. Based on the X-ray CT measurements of aggregate macro-structure and compressive dewatering tests described in Chapters 3 and 4, a simple model was described to relate the aggregate volume fraction, φ_{agg}, to the aggregate size before, $d_{\text{agg},0}$, and after applied shear, d_{agg}. The results show that floc breakage and sediment re-organization can account for a substantial amount of the increase in ϕ_{s} that has been observed in pilot thickening experiments (Farrow et al., 2000).

5.2 Procedure for shared surface area

The calculations and results in this chapter are based on the database of 3D floc images described in Chapter 4, measured at 3.6 μm, with synchrotron-sourced X-ray CT. Here, a simulated breakage of the macro-structure of flocs in the database was carried out. In the set of flocs, 1615 of 8146 had a macro-structure with at least two connected sub-units, whereas the remaining flocs were

comprised of single sub-units. It was assumed that flocs would break along their macro-structure, which was identified in Chapter 4 to be along low ϕ_s regions of the floc structure. This approach permits the size distribution before and after simulated breakage to be compared to determine the potential effect of floc breakage on the floc size distribution.

A consideration of floc connectivity was made here on the basis of the shared surface area and distance to centroid of the floc sub-units in each floc. Intra-aggregate surface area was briefly considered in Chapter 4, but details on the method of calculation and importance of the result were not evaluated. Each floc with a macro-structure has a shared surface area between connected sub-units. The external surface of each sub-unit was fitted with triangular mesh, and neighbouring sub-units share some facets of the mesh. As such, the surface area can be calculated by simply calculating the surface area of shared facets. The value produced by this method should be considered in relative terms, considering the CT image resolution (3.6 μm), because the actual connectivity of the floc structure is on the sub-micron scale.

5.3 Observations of floc structure from X-ray CT data

The pertinent observations that support a floc breakage mechanism from X-ray CT data are: that there is a significant potential for breakage along the weak bonds that hold together the macro-structure of flocs; and that there is an insignificant change in ϕ_{agg} during sediment bed compression in the low applied pressure regime (< 3 kPa).

Floc macro-structure is formed by the aggregation of individual smaller flocs, so it can be observed in medium- and large sized flocs. In Figure 5.1, six example flocs are shown where each sub-unit of the macro-structure is labelled by a different color. This segmentation was carried out based on the procedure described Chapter 4. Briefly, the sub-regions of the ϕ_s-calibrated CT images of each floc were separated along low-ϕ_s boundaries, which divides the 3D flocs into its component sub-units.

In Figure 5.2, the floc size distribution (in terms of the volume-weighted floc diameter, d_{mean}) is shown before and after the simulated breakage of the macro-floc structure. The volume-weighted

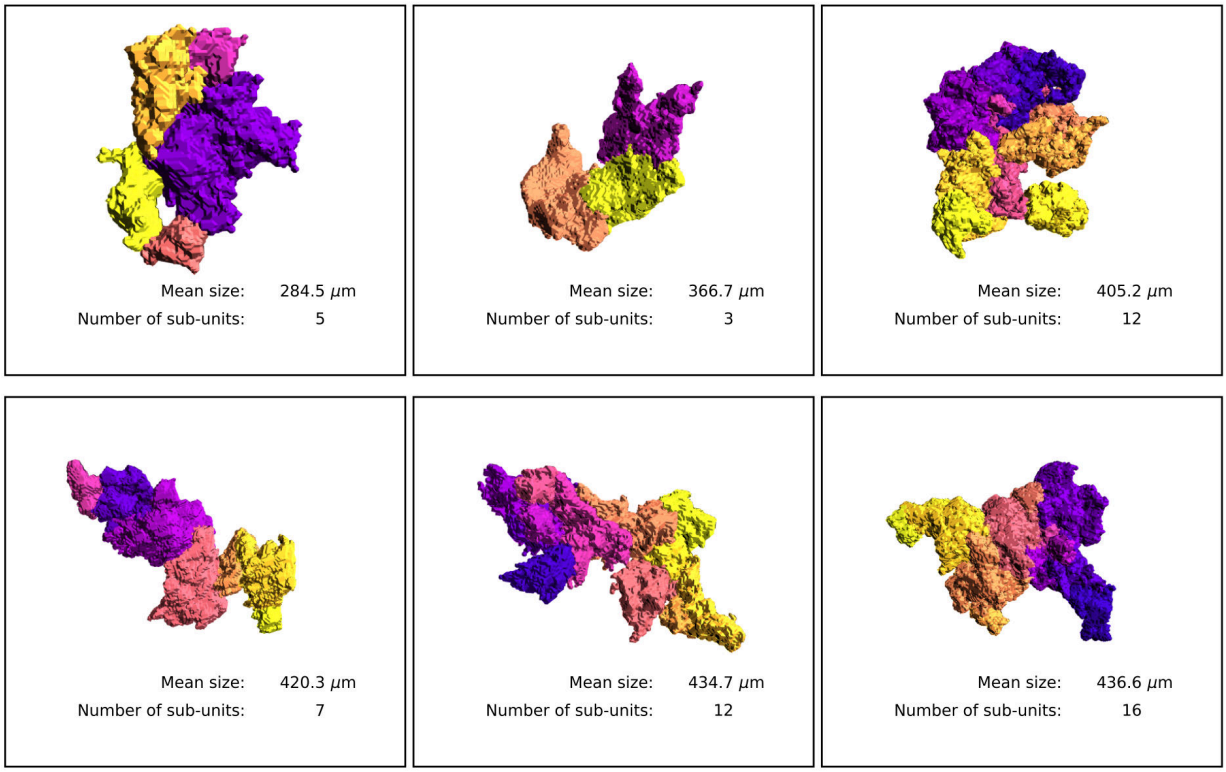

Figure 5.1: Macro-structure of quartz flocs where each sub-unit is labelled with a different color in the floc structure.

average floc size in Figure 5.2 was calculated from the two histograms as $d_{agg,0}$ = 270 μm, before simulated breakage, and d_{agg} = 177 μm, after simulated breakage. For comparison, the characteristic length of the aggregate phase of this system was also measured in a networked bed (240 μm) using a 3D chord length distribution method directly on 7.4 μm resolution micro-CT images (MacIver et al., 2018).

In Figure 5.3, the shared surface area between sub-units in flocs was plotted as a function of sub-unit distance from the floc centroid. For this analysis, all sub-units from the floc dataset were combined. There were 8146 flocs total that contained 12 716 sub-units, and 1615 flocs had more than one sub-unit. The results in Figure 4.14 showed that the total surface area between sub-units increased as a power law function of floc size. Here, the spatial distribution of the shared surface area is also considered. The trend of decreased shared surface area with increased distance from the centroid indicates that the outer regions of larger flocs are held together by fewer connections

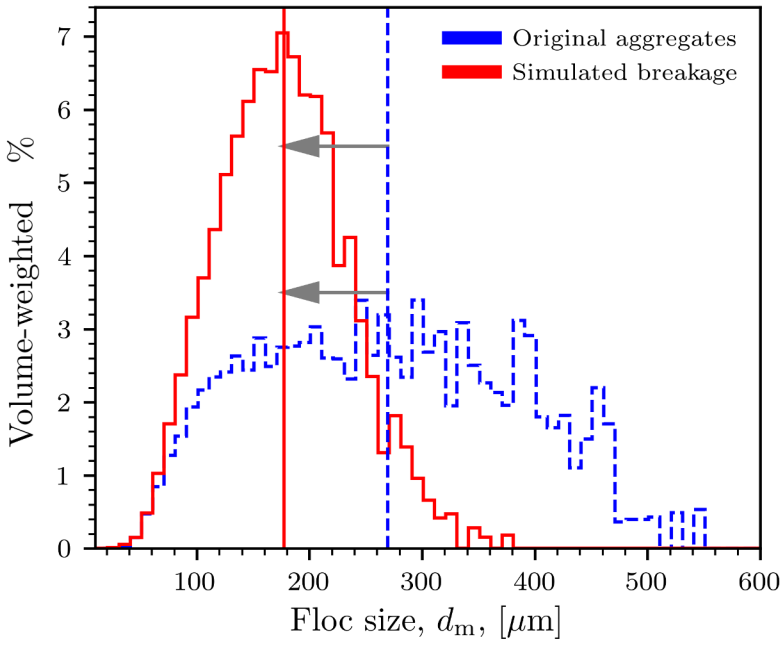

Figure 5.2: Volume-weighted floc size distribution before and after simulated breakage of floc macro-structure along low-ϕ_s boundaries between floc sub-units.

or bonds. Thus, if floc strength is proportional to the number and type of bonds, then the largest flocs are also the weakest and the outer sub-units should tend to break off first.

This inverse correlation between floc size and strength has become somewhat common knowledge (Glasgow, 2003; Yukselen and Gregory, 2004; Klimpel and Hogg, 1991), but is typically explained on the basis of a radial floc density distribution which leads to an inverse correlation between floc size and density. Figure 5.3 suggests that it is rather the radial distribution in number of connections between sub-units of a "spatially clumpy" structure (Bache, 2004) that causes the observed correlation between floc size and strength. This result supports the large-scale deformation or fragmentation breakage mechanism (Jarvis et al., 2005b), rather than surface erosion or the step-wise peeling off of smaller fragments from the floc structure.

It has been shown that flocs are one to two orders of magnitude stronger under compression than shear (Buscall et al., 1987), yet tests of flocculated sediments beds in Figure 3.5 indicated that a negligible change in aggregate solids concentration, ϕ_{agg}, occurred at applied pressures below 3

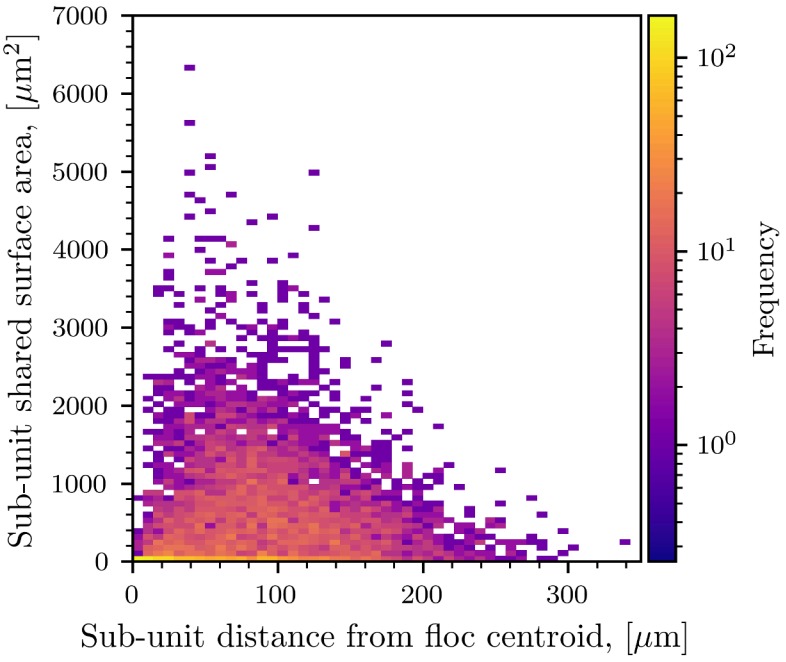

Figure 5.3: Shared surface area of sub-units versus distance from floc centroid.

kPa. In a typical compressive yield stress experiment, the change in ϕ_s of the sample of flocs is measured as a function of applied pressure in a compression dewatering device. Measurement of the sediment structure with ϕ_s-calibrated X-ray CT, however, permits changes in φ_{agg} and ϕ_{agg} to be observed as a function of applied pressure.

In Figure 5.4, the compressive yield stress is plotted for a series of quartz floc compression data obtained from Chapter 3. That study measured the sediment structure after each pressure step using micro-CT to permit a detailed investigation of ϕ_{agg}, φ_{rmagg} and ϕ_s as a function of applied pressure. Figure 5.4 shows the average ϕ_s values for gravimetric measurements overlaid with ϕ_s, φ_{agg}, and ϕ_{agg} obtained from calibrated micro-CT images for a series of flocculated quartz compression tests. The data in Figure 5.4 were fitted with the following equation for the compressive yield stress (Usher et al., 2009):

$$P_y(\phi) = \left(\frac{a(\varphi_{cp} - \phi)(b + \phi - \phi_g)}{\phi - \phi_g} \right)^{-k}, \tag{5.1}$$

where a, k and b were fit parameters (8.5, 1.6, 0.005 , respectively), ϕ_g is the gel point and φ_{cp} is

the close-packing limit (0.8 used here).

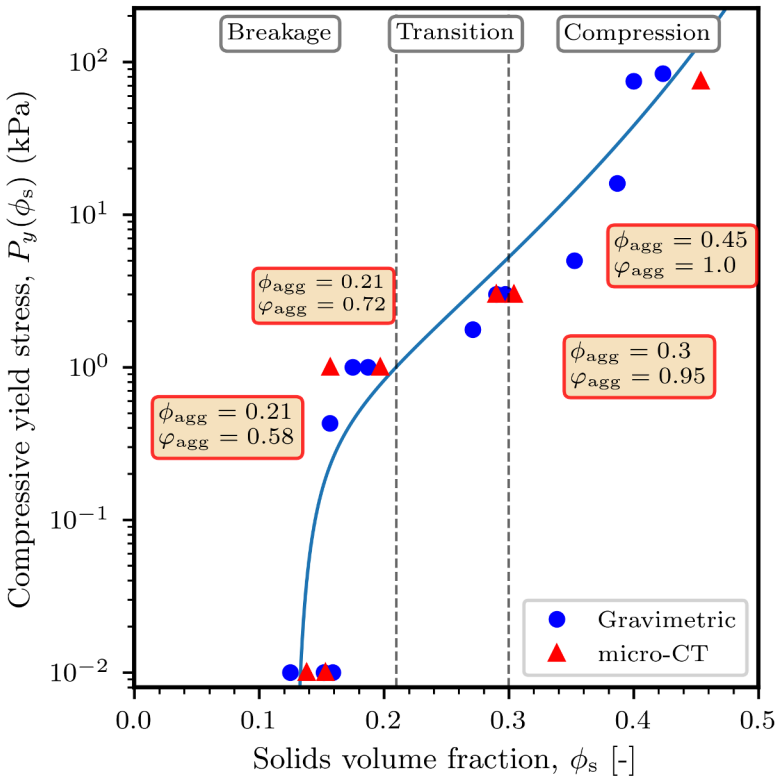

Figure 5.4: Compressive yield stress as a function of solids volume fraction, ϕ_s, for compression tests using the gravimetric method and correlated with tests using the ϕ_s-calibrated X-ray CT images to determine ϕ_{agg} and φ_{agg} properties of the sediment.

The unstressed samples (as prepared in the compression cell) and after 1 kPa of applied pressure, had on average ϕ_{agg}=0.21. This indicates that the increase in ϕ_s at low applied pressure was due to the increase in φ_{agg}, from 0.58 to 0.72, rather than by an increase in ϕ_{agg}. Between 1 and 3 kPa applied pressure, ϕ_{agg} begins to increase from 0.21 toward 0.3, after which only a small fraction of inter-aggregate volume remains. At higher applied pressures, the increase in ϕ_s occurs by an increase in ϕ_{agg} via floc rupture and compression.

Based on the forgoing observations of floc macro-structure and changes in sediment composition as a function of applied pressure, the curve in Figure 5.4 was divided into three regions: breakage, transition, and compression. Breakage of the macro-structure and structural re-organization are the dominant consolidation mechanism in the low pressure regime. This occurs because the

contacts of the sub-units in the macro-structure represent the weakest point in the sediment bed. As such, the energy input by the piston will rupture the connections between the macro-structure first. Between the breakage and compression zones, both φ_{agg} and ϕ_{agg} are changing, so consolidation occurs by a blend of floc breakage, sediment bed re-organization, expulsion of fluid, and floc compression. At the onset of the compression zone in Figure 5.4, the φ_{agg} has been significantly reduced, the macro-structure is broken, and compression of the sediment phase becomes the dominant consolidation mechanism, which increases ϕ_s by increased ϕ_{agg}, ostensibly by the destruction of the primary and secondary layers of floc structure, which require a higher energy input than that required to break the floc macro-structure.

5.4 Effect of floc breakage mechanism on consolidation in a thickener

Although the sediment response to shear cannot be inferred from the compression test and floc structure measurements alone, it is worthwhile to speculate to what extent floc breakage may contribute to enhanced consolidation in a thickener. A comparison is made here of the extent to which the aggregate densification and aggregate breakage mechanisms may contribute to enhanced consolidation in a mixed suspension.

As described in Chapter 2, Section 2.2, aggregates are assumed to have a spherical shape in the CR model. Enhanced consolidation due to applied shear is attributed to aggregate densification which increases ϕ_{agg} and decreases aggregate size according to Equation 2.3. However, in the floc breakage mechanism, ϕ_{agg} is constant and applied shear breaks flocs into smaller sub-units which are re-organized on mixing to increase ϕ_s through increased φ_{agg} (i.e. decreased void spaces in the sediment bed or increased packing efficiency).

In Usher et al. (2009), a case study of the effect of aggregate densification on thickener throughput was presented where the initial values for ϕ_s, φ_{agg}, and $\phi_{agg,0}$ were 0.1, 0.6, and 0.1667, respectively, while the maximum values achieved by applied shear were ϕ_s=0.23 and ϕ_{agg}=0.4. Yet Farrow et al. (2000) reported increases of only ϕ_s=0.06 and ϕ_{agg}=0.1 in two separate systems.

Farrow et al. (2000) measured ϕ_s at various heights in a pilot thickener and extrapolated the expected value at the base to ϕ_s=0.13. However, a value of ϕ_s=0.19 was measured and the increase of ϕ_s=0.06 was attributed to aggregate densification by applied shear. Assuming φ_{agg}=0.6, this is approximately an increase in ϕ_{agg} from 0.22 to 0.32 (using Equation 2.2)). In the second pilot plant, floc density was measured with a floc density analyzer directly after the flocculation feedwell (1.06 g/cm^3, ϕ_{agg}=0.04) and after shear but before the underflow pump (1.22 g/cm^3, ϕ_{agg}=0.15).

Assuming that no change in ϕ_{agg} occurred before the shear zone and that φ_{agg}=0.6, this equates with an increase in ϕ_s=0.066. A distinction between the forgoing studies is that increases of ϕ_s=0.06 and ϕ_s=0.066 were attributed to shear-induced aggregate densification by Farrow et al. (2000), whereas Usher et al. (2009) appear to attribute an increase in ϕ_s of up to 0.12 by applied shear. The ϕ_s and ϕ_{agg} values of Farrow et al. (2000) are perhaps more suitable, in part because they were experimentally obtained; but also because some of the increase in ϕ_s would have been caused by self-weight consolidation, and should not have been attributed only to shear.

In the floc breakage model of consolidation, the range of values of φ_{agg} as a function $d_{agg}/d_{agg,0}$ may be informed from the data presented in Section 5.3 and theoretical studies. In the floc breakage mechanism, it was assumed that floc breakage produces fragments that are more regularly shaped such that the smaller fragments exhibit an improved packing efficiency, or φ_{agg}. As pointed out by Weitz (2004), the packing factor increases by a "surprisingly large amount" when the members of the packing structure are non-spherical. A bed of floc fragments is well-suited for high packing efficiency as non-sphericity and a mixture of different sized particles are critical to achieving high φ_{agg} without an increase in ϕ_{agg}. Estrada (2016) showed that high packing factors can be achieved when three features are present: disorder, a large span between smallest and largest aggregate size, and sufficient small particles to fill the voids in the structure.

Throughout the initial stages of consolidation, φ_{agg} can vary between $\varphi_{agg,0}$ (initial volume fraction of the aggregates) and 1. While $\varphi_{agg,0}$ represents the initial packing efficiency, breakage and re-organization can increase the packing efficiency up to the jammed packing limit. In the case of porous, compressible aggregates, the jammed packing limit may be exceeded by the deformation

of aggregates, which permits an enhanced packing efficiency. Gan et al. measured and simulated packings of irregular particles and found that particle distribution and shape caused initial packing efficiency (φ_{agg} here) to vary between 0.2 and 0.6 (Gan et al., 2004). In Figure 5.4, φ_{agg} in the uncompressed sample was between 0.5 and 0.55. It is unlikely that breaking and mixing alone can achieve values of $\varphi_{agg} > 0.8$, based on the results in Figure 5.4; although this is significantly higher than the case of a model using poly-disperse spheres, which can reach up to φ_{agg} = 0.64 (Baranau and Tallarek, 2014b). In Figure 5.4, φ_{agg} was 0.72 at the beginning of the transition zone (before an increase in ϕ_{agg}) and 0.95 after the transition zone; thus, it is not unreasonable to take the maximum value of φ_{agg} to be between 0.75 and 0.8.

Alternatively, if the fractal dimension, D_f, and aggregate size are obtainable by image analysis of the aggregates, the equation provided by Kranenburg (1994), may be used to estimate φ_{agg} as

$$\varphi_{agg} = \varphi_p \left(\frac{r_a}{r_p} \right)^{3-D_f}, \tag{5.2}$$

where φ_p is the volume fraction occupied by primary particles, r_a and r_p are the radius of the aggregate and primary particles, respectively.

To express how consolidation is increased by shear-enhanced floc breakage, a modified version of Equation 5.3 was used to relate floc size and φ_{agg} with

$$\phi_B = \phi_{agg,0} \varphi_{agg}, \tag{5.3}$$

where ϕ_B is the increase in ϕ_s caused by floc breakage and re-organization, $\phi_{agg,0}$ is the original aggregate solids volume fraction (constant), and φ_{agg} is replaced with a linear model:

$$\varphi_{agg} = a \left(\frac{d_{agg}}{d_{agg,0}} \right) + b, \tag{5.4}$$

where a and b are fit parameters. It is noted that a linear model was chosen here for the sake of simplicity in this semi-quantitative model to produce a trend that relates change in aggregate size (as a result of breakage) and packing efficiency (φ_{agg}.) Additionally, the values selected from the

measured CT data and resulting relationships derived are expected to be specific to the current system under study.

In Figure 5.5, the relation between φ_{agg} and $d_{agg}/d_{agg,0}$ was modelled with Equation 5.4. Aggregate volume fraction, φ_{agg}, was modelled between 0.5 and 1, while $d_{agg}/d_{agg,0}$ was permitted to decrease from 1 to 0.8. Self-weight consolidation will increase ϕ_s between the top of the thickener (at ϕ_g) and the base of the thickener (ϕ_{base}). In the breakage model, this change was accounted for by decreased $d_{agg}/d_{agg,0}$ and decreased φ_{agg}. For this reason, the point at D=0.925, φ_{agg}=0.65 is labelled, which indicates the values at the onset of applied shear in the case of the floc breakage consolidation mechanism.

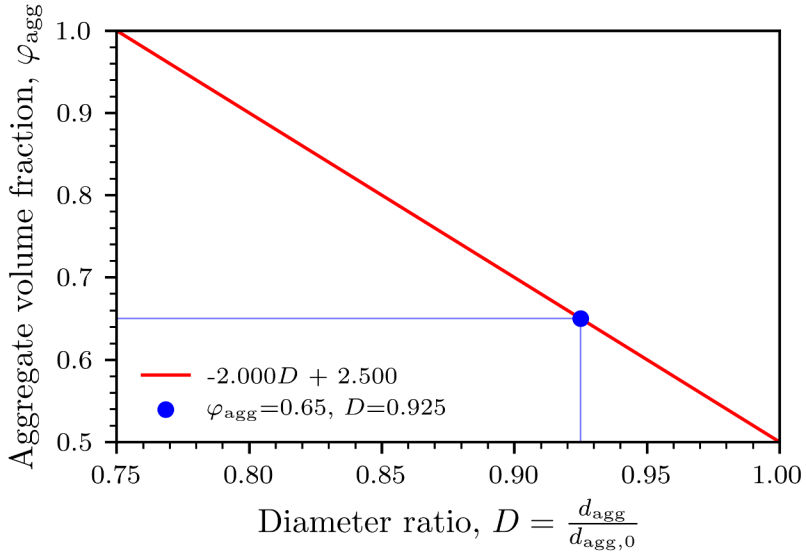

Figure 5.5: Change in packing fraction, φ_{agg} with change in aggregate diameter ratio, D, for power law and linear fits

In Figure 5.6, ϕ_{agg} and ϕ_g were calculated for various $d_{agg}/d_{agg,0}$ ratios for consolidation by the aggregate densification mechanism, using Eq. 2.3, and the breakage mechanism, using Equations 5.3 and 5.4. The key assumptions are that ϕ_g=0.1, φ_0=0.5, and ϕ_{base}=0.13 (solids volume fraction at the base of the thickener), from which the remaining values are calculated. At the base of the thickener, ϕ_{base}=0.13 for both consolidation mechanisms. In the case of the floc breakage mechanism, consolidation due to shear proceeds from $d_{agg}/d_{agg,0}$=0.925 to 0.8 as the sediment

solids volume concentration increases from ϕ_s=0.13 to 0.18 (due to an increase in φ_{agg} from 0.65 to 0.8). By the aggregate densification mechanism, a reduction in aggregate diameter factor from 1 to 0.8 causes an increase in ϕ_s from 0.13 to 0.25 and is accompanied by an increase in $\phi_{agg.}$ from 0.2 to 0.39.

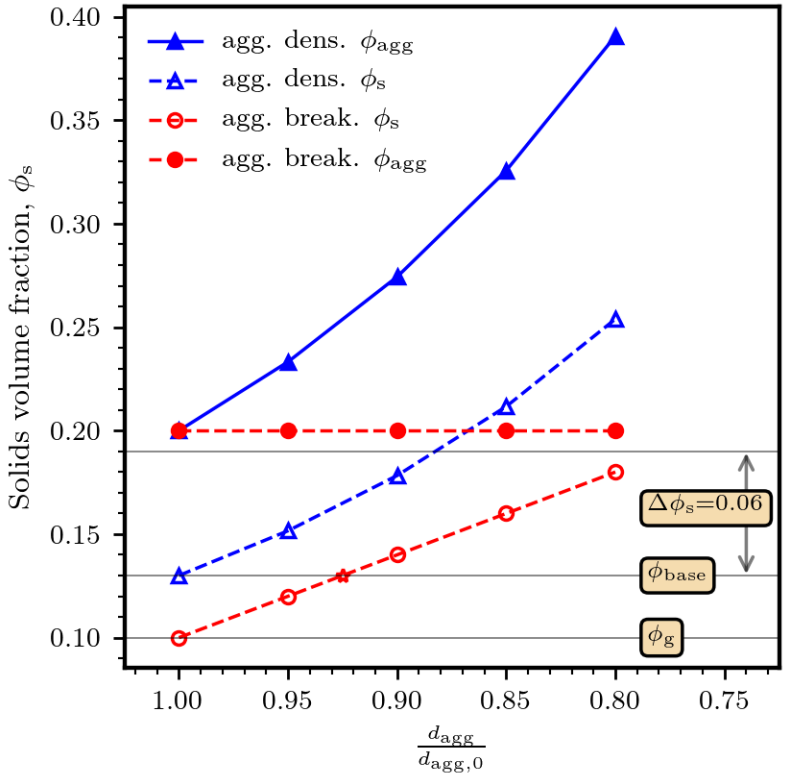

Figure 5.6: Aggregate densification and breakage consolidation pathways and their effect on the average ϕ_s value.

5.5 Conclusions

The objective of presenting this simple, semi-quantitative model of sediment consolidation by aggregate breakage was to highlight the range of ϕ_s increase that could be attributed to floc breakage and re-organization due to applied shear in a thickener. In Figure 5.6, the increase from breakage is $\Delta\phi_s$=0.05 (from 0.13 to 0.18), which is in the same range measured in two separate experiments by Farrow et al. (2000), where an increase of $\Delta\phi_s$=0.06 due to applied shear was measured in the base of a pilot thickener. However, the increase in ϕ_{agg} required to increase ϕ_s by the aggregate

densification mechanism is far higher. Such a large increase in ϕ_{agg} has not been supported by experimental results to date.

Nonetheless, the mechanism of aggregate densification provides a powerful model to explain increased thickener throughput due to applied shear in the lower region of a thickener. Conceptually, an increase ϕ_{agg}, increases the suspension gel point and the settling rate of the aggregates in the suspension (Usher et al., 2009). Yet enhanced sedimentation will also be observed when an irregularly shaped floc is broken into fragments, because no change in ϕ_{agg} can be attributed to the breakage event, and the resultant fragments will experience less hydrodynamic drag.

The results in Figure 5.3 indicate that control of floc structure will also have an impact on the subsequent consolidation process. Flocs with lower connectivity between floc sub-units are more likely to have more extended structures, which would make their initial packing efficiency (φ_{agg}) lower. Additionally, assuming the strength is correlated with the cross-sectional area of connected regions in the floc, the strength of such flocs would be weaker. Thus, flocculation strategies that targeted the production of a more extended floc structure would result in a larger overall volume of flocs (to contain the same amount of solids), but the sediment would break down quicker. Such a strategy could be desirable to increase the amount of stratification in high-throughput thickeners.

It is acknowledged that the mechanics of consolidation in the shear zone of a thickener are quite complex and that the present analysis greatly simplifies the problem in an attempt to gain insight. Further research into the mechanics of shear-induced consolidation would be useful because this understanding would allow researchers and practitioners to develop improved flocculation and dewatering design strategies. For example, if an aggregate densification mechanism turns out to be dominant, perhaps flocs should have a compact structure that would withstand breakage by shear in order to undergo aggregate densification. However, if an aggregate breakage mechanism is dominant, perhaps flocs should have a more extended structure. That would allow them to settle initially at a low packing efficiency (which would allow higher fluid flux in the upper regions of the sediment bed), but also permit them to break easily in the presence of shear stress so the fragments could re-organize with mixing to a higher packing efficiency.

The next chapter, Chapter 6, demonstrates how measurements of floc volume using 2D images can be improved when information about floc structure from 3D information is available.

Chapter 6

Floc volume from 3D images and 2D projections

6.1 Introduction

Flocs are highly porous, irregularly structured, fine particulate aggregates encountered widely in natural and engineered systems (Jarvis et al., 2005b). Mass flux models in these systems depend on the measurement of floc volume and density, which are often obtained from 2D images, including from settling columns or under the microscope. Yet flocs are 3D structures and their representation in 2D images has been shown theoretically (Hunt and Kaloshin, 1997) and experimentally (Orhan et al., 2016) to cause the loss or distortion of spatial information contained in the 3D image of the object. An understanding of this distortion is important to improve models based on the floc properties obtained from 2D measurements.

Although floc properties are routinely calculated from 2D images, there is no general method for recovering the properties of an irregularly shaped 3D object from a single projection in 2D. Methods for the conversion of 2D images or video to 3D typically rely on one of two methods: the combination of information from projections obtained from multiple perspectives (e.g. stereoscopic image pairs or photogrammetry) or the concurrent acquisition of a 2D and depth image on the same image volume (Ramesh and Letitia, 2019). A method for conversion of single 2D images

to 3D has been demonstrated (Konrad et al., 2013), but requires a priori knowledge of the 3D scene in the form of a machine learning model that permits localization of 2D images in the 3D space. A method of general moments has been devised to recover a 3D object shape using the 2D image intensity, but it is subject to several constraints on object shape and only works for a narrow range of parameters (Salzman, 1990).

An alternative to recovering the 3D object from 2D images is to instead estimate the properties of the 3D object from 2D images. This approach has been demonstrated through direct measurements for convex shapes, such as tissue cells (Sharp et al., 2019) and sand particles (Xie et al., 2020), but has not been demonstrated for irregular shapes with concave geometry, such as flocs. Theoretically, for spheroidal shapes, it has been shown that a relatively accurate estimate of 3D properties can be made from a single 2D projection (Piccinini et al., 2015). It has been suggested that floc properties in 2D images are likely to be an overestimate of the true 3D values (Jarvis et al., 2005b), and this has been demonstrated by Orhan et al. (2016) in a study of soot aggregates, where a significant difference was found between the volume and surface area measured from 3D images compared with estimates obtained from the 2D image data.

This chapter compares the estimation of floc volume from 2D and 3D images to identify how insights from 3D floc structure measurements can be used to improve floc volume estimates from 2D image data. X-ray computed tomography (CT) and settling videos of polymer-flocculated quartz flocs were measured. An experimental approach was taken by comparing the floc volume measured from 3D images to the value obtained by calculating floc volume from 2D projections of the 3D flocs. The relationship determined between the 2D and 3D floc properties was then applied to 2D images obtained in settling column experiments, to demonstrate an improved approach to calculating floc volume from 2D images. While 3D images may provide valuable insight into floc structure, instrumentation and methods for 2D image acquisition and analysis are far more popular, easier to operate, and at least an order of magnitude less expensive. For this reason, this chapter may at least serve to raise awareness of the limitations of floc volume estimations from 2D images and how such estimates may be improved.

6.2 Background

Two definitions of floc volume are the encased volume and the volume occupied by solids (Logan et al., 1991). The encased volume may be considered the volume obtained by fitting a convex hull around the floc and is typically approximated with the equation of a sphere,

$$V_{\mathrm{e}} = \frac{\pi}{6} d^3 \tag{6.1}$$

where d is the 2D floc diameter. Equation 6.1 has been widely applied in the literature to estimate floc volume from floc settling videos (Sun et al., 2016; Curran et al., 2007; Syvitski and Hutton, 1997; Medalia, 1970; Bache, 2004). When the Ferret diameter or major axis length is chosen, the volume is the exclusion volume. However, other measures may be used, including the equivalent diameter,

$$d = \sqrt{\frac{\pi}{4A}}, \tag{6.2}$$

and mean diameter,

$$d_{\mathrm{mean},2} = \sqrt{d_1 d_2}, \tag{6.3}$$

where A is the floc area in 2D, and d_1 and d_2 are the major and minor axis lengths of the ellipse that encloses the floc. A simple

The floc volume occupied by solids may be considered the volume obtained by fitting a concave hull, or tight-fitting surface mesh, to the regions in the floc that contain a mixture of solids and water. This occupied volume can be obtained by dividing the volume of solids by floc porosity,

$$V = \frac{V_{\mathrm{s}}}{1-\varepsilon}, \tag{6.4}$$

where V is the floc volume, ε is the porosity (which is related to the solids volume fraction by 1-ϕ_{s}), and V_{s} is the volume of solids. In this definition of floc volume, all of the porous phase

material is enclosed in the floc and can be related to the bulk density, ρ_f, by

$$\rho_f - \rho_w = \phi(\rho_s - \rho_w), \tag{6.5}$$

where ρ_s and ρ_w are the bulk density of the solid primary particles and water.

Equation 6.4 requires the floc porosity and total solids volume of the floc to calculate volume. While floc porosity estimates can be obtained from 2D images, the method is restricted to optically transparent flocs or to tomograms, rather than 2D projections. The direct measurement of floc mass is destructive, and time consuming, so most estimates in the literature come from the application of Stokes' Law (and its various modifications) to calculate floc mass.

An alternative to the preceding definitions of floc volume is to use an equation that incorporates fractal mathematics to account for the non-spherical, irregular geometry of flocs. A more detailed description of the application of fractal geometry to flocs was made in Chapter 2 (background), so the following discussion proceeds directly to the estimation of floc volume using 3D fractal dimension.

Floc volume has been calculated using the 3D fractal dimension according to (Logan et al., 1991):

$$V_f = \psi^{\frac{D_3}{3}} \xi_0 d_0^{3-D_3} d^{D_3}, \tag{6.6}$$

where $\psi = \zeta \frac{\xi}{\xi_0}$, ζ is the packing factor, ξ and ξ_0 are the shape factors of the aggregate and primary particles, and $\psi^{\frac{D_3}{3}}$ is the pre-factor or structure factor, which along with D_3 is a measure of the space-filling ability of the floc, and hence, its compactness.

It has also been shown that the 2D projection of floc area is a function of the 2D fractal dimension, D_2, according to (Serra and Casamitjana, 1998):

$$A = \xi_2 d_0^{2-D_2} d^{D_2}, \tag{6.7}$$

where ξ_2 is the 2D shape factor and A is the projected area in 2D. This allows the volume and 2D

area to be related through the 2D and 3D fractal dimensions, D_2 and D_3 as follows:

$$V \propto A^{\frac{D_3}{D_2}} \tag{6.8}$$

6.3 Methods

For X-ray CT imaging and settling column video-recordings, quartz flocs were prepared according to the flocculation method described in Section 3.2.1. The procedures and equipment used to embed flocs in agar, obtain CT scans, and reconstruct the CT images and extract a dataset of almost 9000 floc images were described in Section 4.2.1 and Section 4.2.2. In this study, the Weka machine learning framework (Frank et al., 2016) was used for the secondary segmentation of floc structure in place of the MBWT.

To produce simulated 2D projections from various viewing angles points on the floc, a sequence of elemental, extrinsic rotations about the floc centroid were applied, followed by orthographic projection along the z-axis of the rotated floc. Each floc was rotated around its x-axis by θ_x-degrees and y-axis by θ_y-degrees, from 0 to 179 degrees, in 5 degree increments, to obtain a reasonable sampling of all possible orientations in 3D. Figure 6.1 illustrates the extraction of a projection (along the z-axis onto the xy-plane) and a slice (in the xy-plane at the floc centroid) at θ_x=0, θ_y=0 and Figure 6.2 indicates the view points obtained.

Images of settling quartz flocs were recorded in a water-filled square-based column setup described in (Shakeel et al., 2021). The column was 10 cm x 10 cm x 30 cm, with glass front and rear panels, and acrylic plastic sides. Images were recorded at 30 frames-per-second, in a bright-field setup illuminated by a directional LED light source, with a camera and telecentric lens combination that produced a pixel size of 8.6 μm. Flocs were introduced through a miniature conical feedwell with a 5mm x 5mm mesh to distribute flocs and prevent large clumps from entering the settling column.

Videos were analyzed with Sedimentation and Floc Analysis Software (SAFAS, v0.1), a custom software for the analysis of floc images and videos. The software includes a graphical user

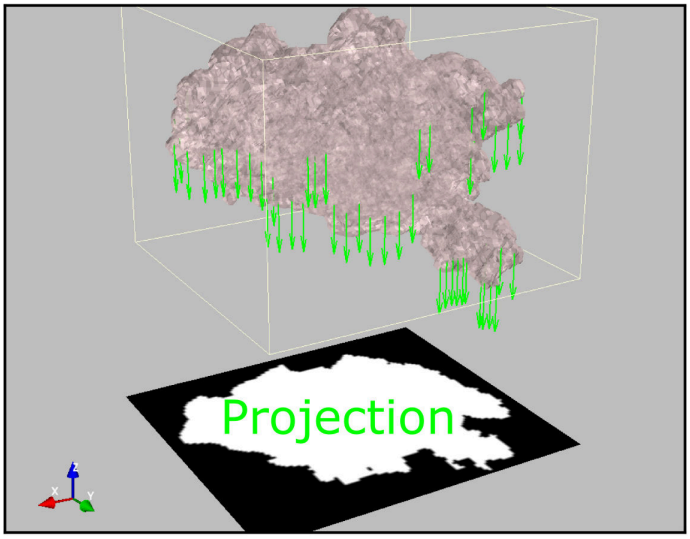

Figure 6.1: Projection and slice of a 3D floc onto a 2D plane.

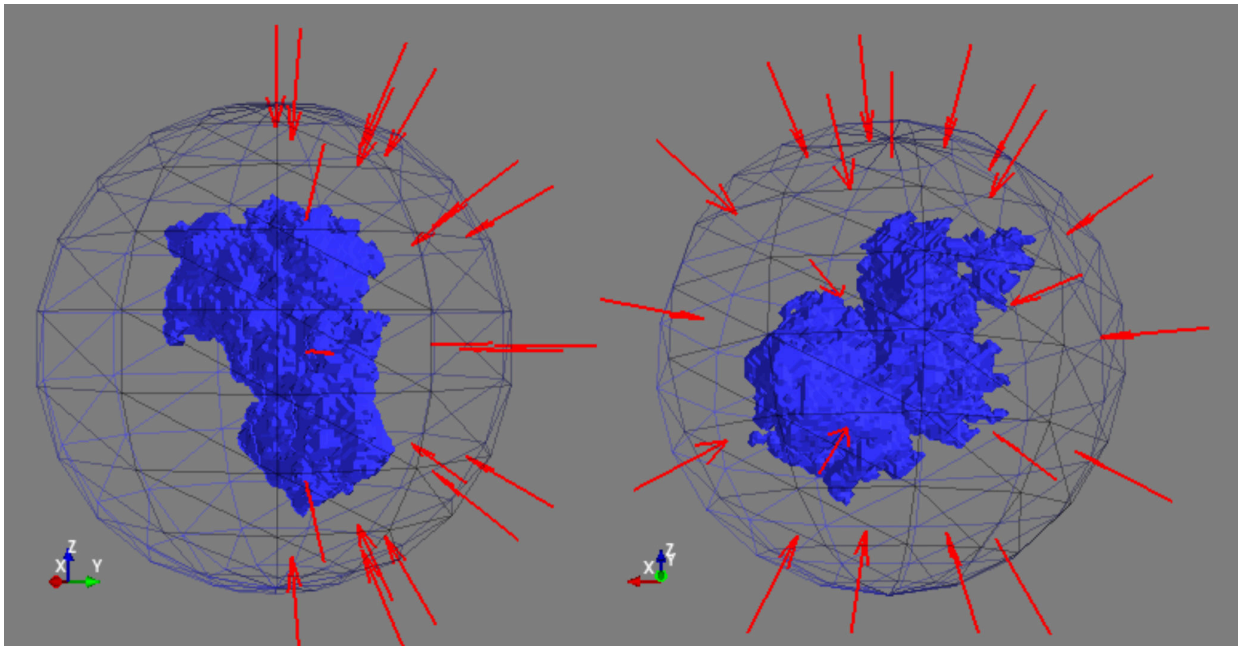

Figure 6.2: The red arrows indicate the location and direction of projections simulated on the 3D floc.

interface and uses OpenCV and Python packages (Scikit-Image, SciPy, Numpy, and Pandas) to permit the user to quickly and accurately segment and track flocs through a time-series of images.

6.4 Calculations

In addition to the mean diameter in 2D, $d_{\text{mean},2}$ (Equation 6.3), the 3D floc size was calculated according to (Jarvis et al., 2005b):

$$d_{3,\text{mean}} = (d_1 d_2 d_3)^{1/3}, \tag{6.9}$$

where d_1 (minor), d_2, and d_3 (major) were the three principal axes lengths of the 3D floc.

Floc shape was estimated using the aspect ratio for 2D flocs as (Syvitski and Hutton, 1997):

$$AR_2 = d_2/d_1 \tag{6.10}$$

and for 3D flocs as:

$$AR_3 = d_3/d_1. \tag{6.11}$$

To calculate the box-counting dimension of an object (in 2 or 3 dimensions) it is required to determine the minimum number of tiles (in 2D) or cubes (in 3D) N of size d required to cover the object in the binary image. The slope of a log-log plot of $N(d)$ versus $1/d$ is the box-counting dimension, $D_{\text{bc},2}$ or $D_{\text{bc},3}$. For this study, a box-counting method was implemented using Python. A more complete description of box-counting was given by Bushell et al. (2002).

For the results in this chapter, floc volume was measured directly from 3D images of flocs. This allowed the floc volume to be calculated with Equations 6.1, 6.6, and 6.8, using the simulated 2D projection measurements, and compared with the actual values measured from the 3D flocs.

6.5 Results

Figure 6.3 shows the cumulative size distribution of quartz flocs from 3D images (from 8485 X-ray CT image sub-volumes), 2D images (simulated projections on the 3D images), and settling column images. From the 3D images, almost all flocs (> 99 %) were between 20 μm and 800 μm

in size. The settling column data had a larger mean floc size (150 μm) compared with the simulated 2D images (103 μm) and 3D images (92 μm). Sample preparation may have contributed to this difference to some extent. For example, some floc breakage may have occurred when the flocs were mounted in agar for CT scanning, which helps to explain the occurrence of the shift to larger floc sizes in the settling column data, because the sample handling requirements are less invasive for that method.

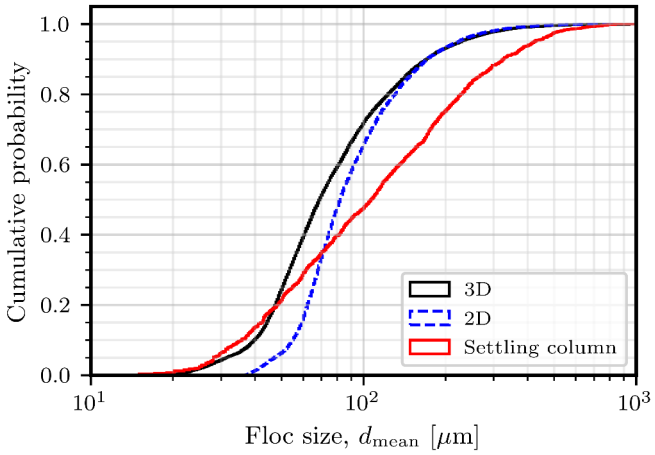

Figure 6.3: Cumulative size distribution of mean 3D floc size, $d_{\mathrm{mean},3}$.

Surface models of three flocs are shown in Figure 6.4. The purple plane inserted in each model corresponds to the tomogram shown in the lower part of the figure. The x- and y- axis orientation in the sub-figures are similar, but in the 2D slices, the z-axis is perpendicular to the page.

6.5.1 3D images and 2D projections

For each 3D floc image, 2D projections were generated from 46 different viewing angles. Taking the mean value of the floc properties measured from the set of 2D projections permits a direct comparison to the properties calculated from each 3D floc. In Figure 6.5 (A), the mean 2D D_{mean} values are plotted against the 3D D_{mean} value for all flocs. Note that the plots on this figure are 2D histograms with an associated frequency colormap shown at the right of the figure. The solid black line in each plot represents a 1:1 correspondence between measured 2D and 3D values. In general, the mean of 2D D_{mean} values overestimates the 3D D_{mean} value at small floc sizes (< 200 μm),

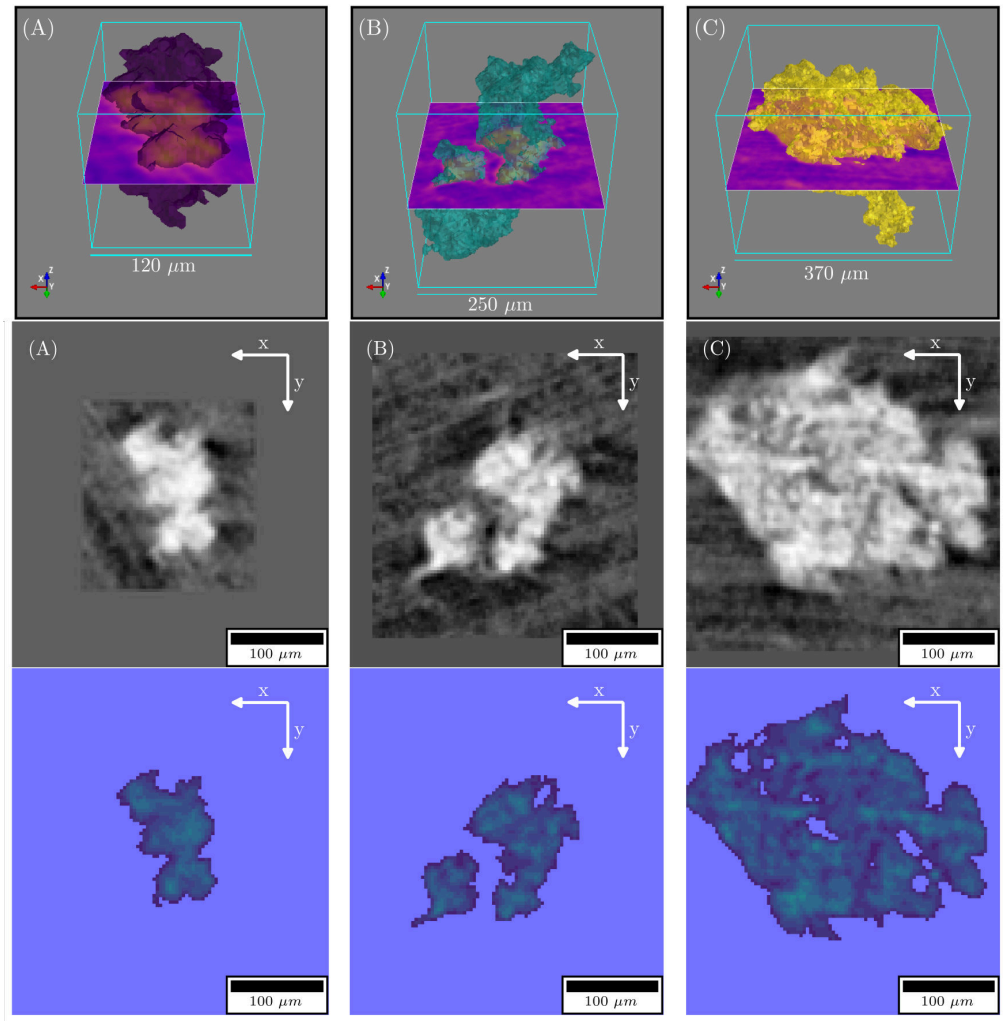

Figure 6.4: Flocs in 3D images from X-ray computed tomography.

but underestimates 3D floc size at larger floc sizes (> 200 μm). This is inline with observations elsewhere, that diameters based upon 2D images tend to be larger than those based upon 3D images (Jarvis et al., 2005b).

The histograms of the 2D D_{mean} values obtained from four exemplary 3D flocs are shown in Figure 6.6. In each plot, the solid vertical line represents the mean of the 2D floc size values and the dashed vertical line represents the 3D floc size value. Thus, the differences observed in Figure 6.6 are representative of that trend, with 2D and 3D values showing good correspondence in (B) at 162 μm versus 164 μm and in (C) at 240 μm versus 232 μm, while in (A) the relative overestimate of the value produced from the 2D images is much higher, at 70 μm versus 54 μm.

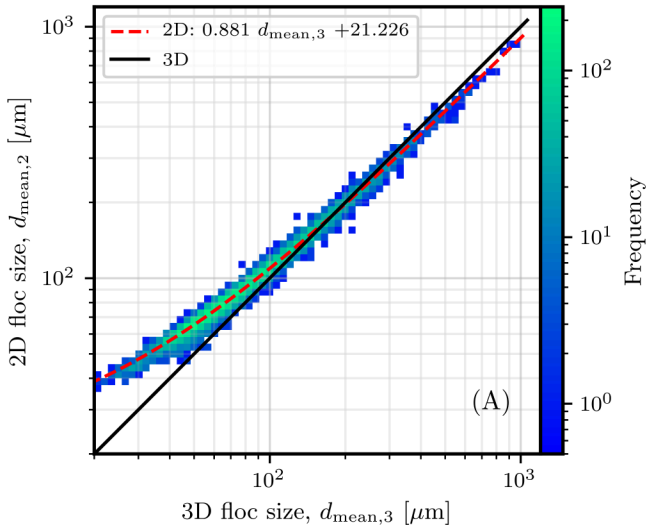

Figure 6.5: Comparison of floc size, radius of gyration and aspect ratio measured from 3D images versus the mean value from a set of 2D projections.

In (D) the underestimate of D_{mean} is almost 70 μm, with a value of 431 μm from the 2D images compared to 509 μm in the 3D image.

The trends in D_{n} shown in Figure 6.7 indicate that the flocs are taking on a more extended structure from the smallest floc sizes up to 110 μm, then becoming more regular again at larger flocs sizes. To model the observed trend, box counting dimension, $D_{\text{bc,n}}$, versus floc size, d_{mean}, values were fitted with a linear model up to 110 μm, while a power fit was applied between 110 μm up to the largest floc sizes. The dashed horizontal line at $D_{\text{n}} = 2$ represents the upper limit permissible for D_2. The box counting dimensions decrease from the maximum permissible values, 3 for $D_{\text{bc,3}}$ and 2 for $D_{\text{bc,2}}$, starting from the smallest floc sizes, then rebound slightly with increasing floc size. Similarly, Gorczyca found that a piece-wise linear fit was the most suitable to model fractal dimension as a function of floc size (Gorczyca and Ganczarczyk, 1999), because a single power law model produced worse results over all size ranges.

This result agrees with previous analysis of this dataset, which indicated that these flocs have a macro-structure comprised of smaller sub-units with mean size of 105 μm (Chapter 4). It was reasoned that medium- and large-sized flocs in the dataset were formed by cluster-cluster aggregation of smaller flocs or sub-units. Thus, one way to interpret the trend in Figure 6.7 is that during

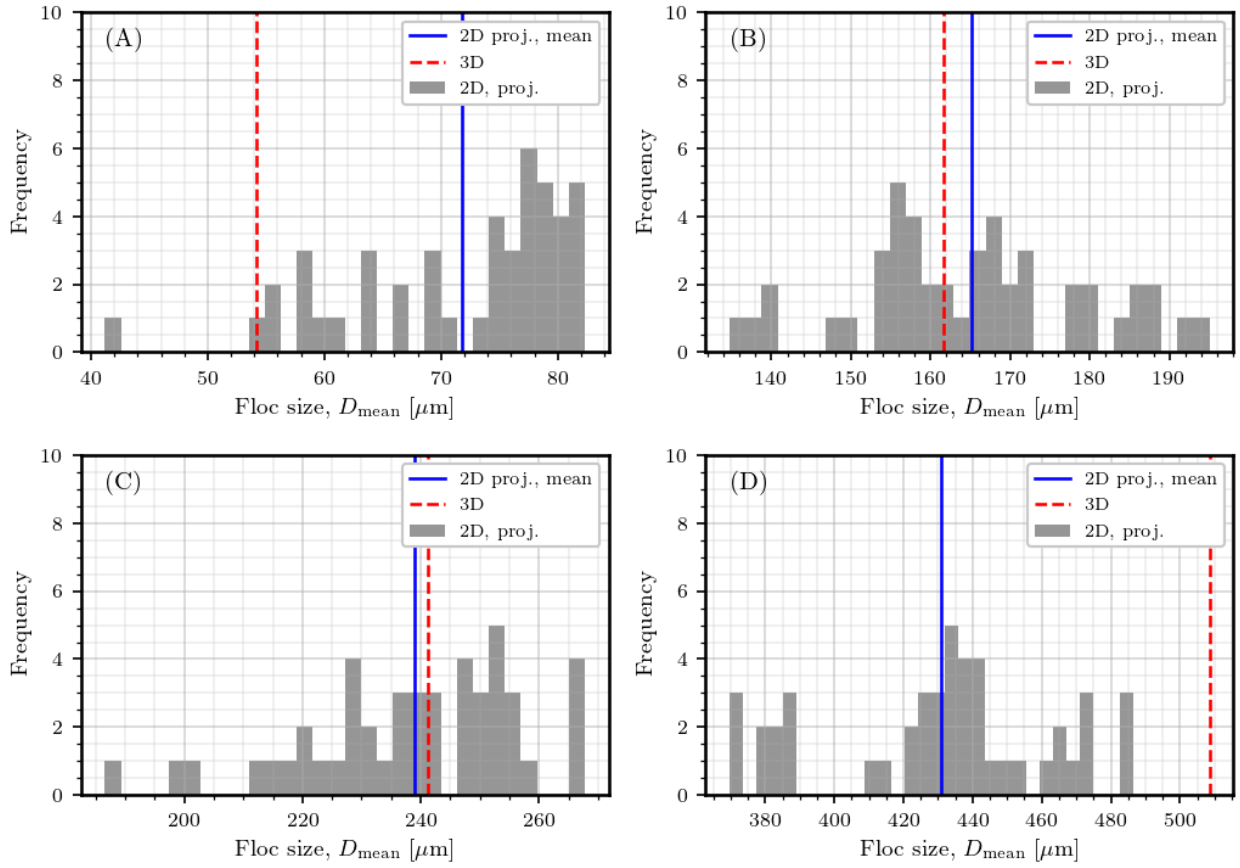

Figure 6.6: Histogram of floc size calculated from 2D projections compared with the value measured from the 3D image.

the formation of small flocs (sub-units), the floc structure becomes more irregular as floc size increases. However, the formation of larger flocs occurs by cluster-cluster aggregation of sub-units, so only sub-units with a sufficient amount of shared surface area will stay intact (i.e. poorly connected flocs will break very easily.) So, the largest flocs tend to have a more compact structure, more shared surface area between floc sub-units, and have a higher fractal dimension. This has been observed elsewhere in a study of floc structure densification where flocs became more compact by reducing their extended structure on application of shear (Mills et al., 1991). Thus, it may be concluded from this result that floc structure is dominated by primary and micro-floc aggregation at smaller floc sizes, while cluster-cluster aggregation of larger sub-units dominates the floc structure at larger floc sizes.

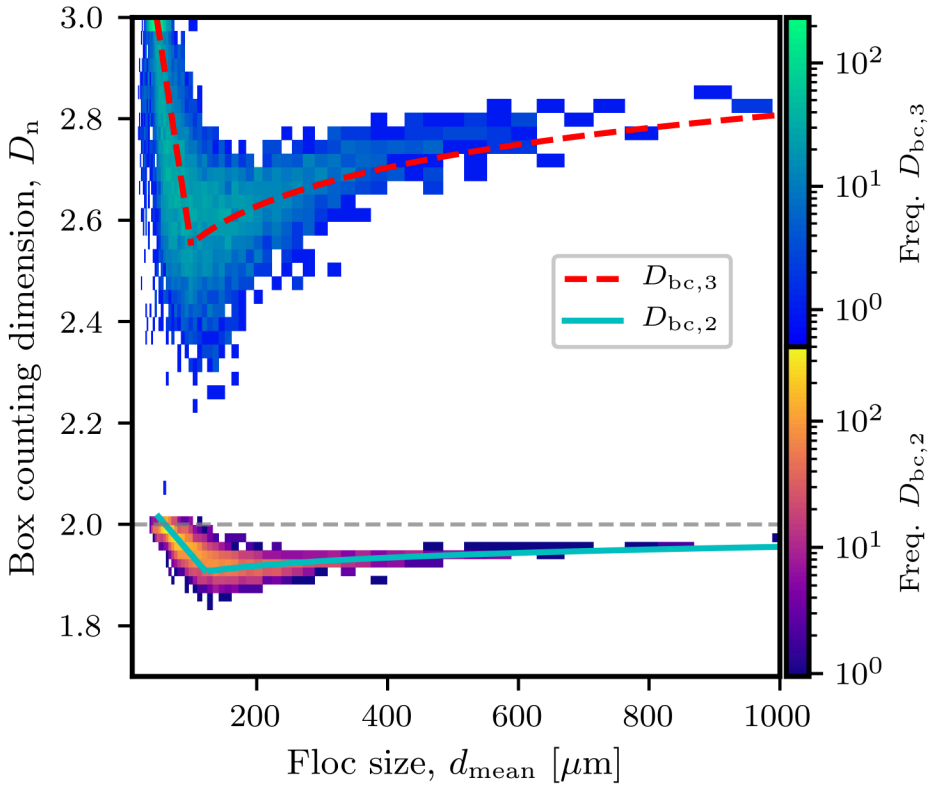

Figure 6.7: Relationship between fractal dimension with floc size for 3D images ($D_{bc,3}$) and 2D projections ($D_{bc,2}$).

It has been shown that only the 3D fractal dimension is appropriate for modelling the structural and settling properties of flocs (Vahedi and Gorczyca, 2010). Yet the direct determination of 3D floc fractal dimension typically requires a 3D image of the floc, so methods for obtaining D_3 indirectly have been pursued in the literature. Maggi and Winterwerp (2004) used simulated 3D flocs to relate D_3 to the $D_{2,lav}$ perimeter-area relationship observed in the 2D projections of simulated 3D flocs and Expósito et al. (2017) demonstrated a method for predicting D_3 from $D_{2,lav}$ using confocal laser scanning microscopy to measure 3D images of flocs. Vahedi and Gorczyca (2010) compared the mass fractal dimension (using settling rate and floc size data) to D_3 measured from using the box counting method on 3D floc images. However, there are few reports in the literature that compare 2D and 3D box counting dimensions directly.

In the case of a 2D cross-section of a fractal object, D_2 and D_3 have been related by Thill et al.

(1998):

$$D_2 = D_3 - 1 \tag{6.12}$$

and Lee and Kramer (2004) determined the relationship between D_3 and D_2 as:

$$D_3 = 1.391 + 0.01\mathrm{e}^{2.164\mathrm{D}_2}. \tag{6.13}$$

In Figure 6.8, the relationship between $D_{\mathrm{bc},3}$ and $D_{\mathrm{bc},2}$ for the current data is compared to two estimates from the literature. The red dot-dash line represents the line of best fit to the data measured in this study. Although the data in Figure 6.8 display quite a lot of scatter, a distinct linear relationship between $D_{3,\mathrm{bc}}$ and $D_{2,\mathrm{bc}}$ is evident. The slope of the fit between $D_{3,\mathrm{bc}}$ and $D_{2,\mathrm{bc}}$ values is higher than Equation 6.12 predicts (i.e. slope = 1). Equation 6.13 does not fit the data well because it was an empirical fit for values of $D_{\mathrm{bc},2}$ between 1.3 and 2 and the 3D fractal dimension did not converge on 3 as the 2D values tended toward 2.

6.5.2 Floc volume estimates from 2D data

This section demonstrates how the 2D image data can be used to estimate the floc volume. In Figure 6.9, the relationship between measured and predicted floc volume from 2D and 3D size is shown for Equations 6.1, 6.6, and 6.8.

Using the 2D $d_{\mathrm{mean},2}$ values directly in the equation of a sphere produces an overestimate of floc volume across all floc sizes. Although the volume estimates using the 2D floc size, $d_{\mathrm{mean},2}$, and 3D floc size, $d_{\mathrm{mean},3}$, fall on the same trend line, the 2D values actually produce a greater overestimate of floc volume than observed in Figure 6.9, due to the relationship between 2D and 3D $d_{\mathrm{mean},3}$ shown in Figure 6.5(A). For example, if the 2D $d_{\mathrm{mean},2}$ is 100 μm, a volume of $\approx$ 524x10^3 μm^3 is obtained, compared to the volume estimated from the 3D d_{mean}, $\approx$ 394x10^3 μm^3. Values thus converted will fall along the same trend line, but be shifted to larger or smaller volumes, depending on floc size. Nonetheless, the result of applying Equation 6.1, even with adjustment of floc size,

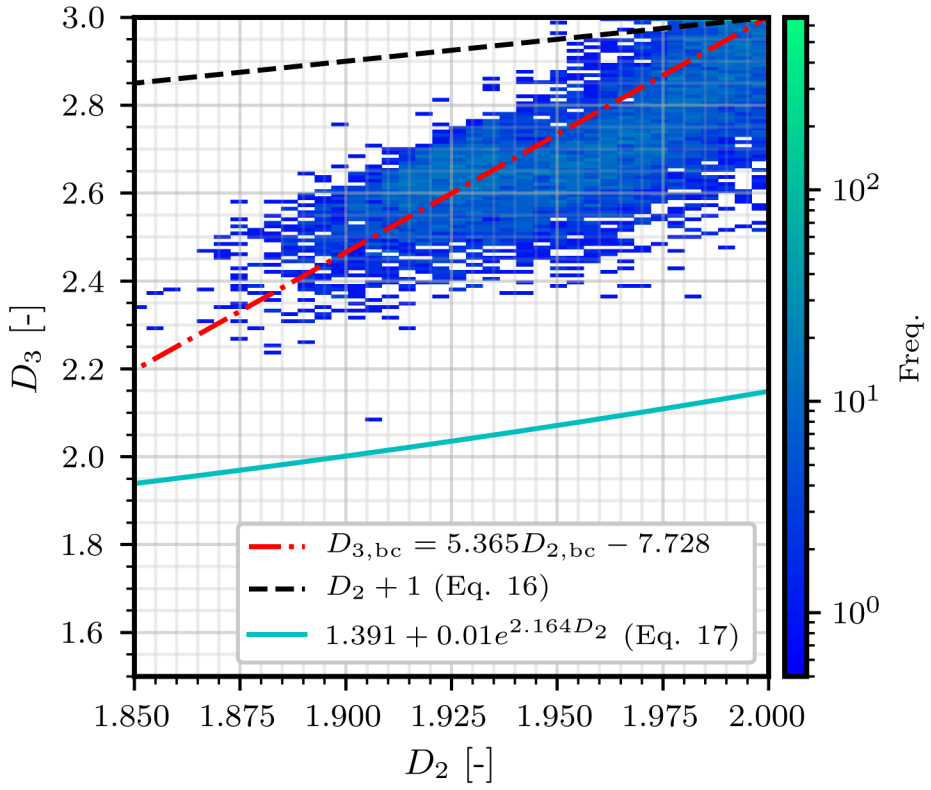

Figure 6.8: Relationship between box counting with floc size for 3D images ($D_{\mathrm{bc},3}$), 2D projections ($D_{\mathrm{bc},2}$), and settling column images (settling $D_{\mathrm{bc},2}$).

produces nearly an order of magnitude overestimate of floc volume at larger floc sizes.

Equation 6.8 works well for floc sizes above 1x10^6 μm^3, based on the closeness of the data fit, but is much worse than using the simple equation of a sphere below that value. This is due to the clustering of box counting dimension values at small floc size near 2 (in 2D) and 3 (in 3D). As a result, it is expected that Equation 6.8 would predict floc volume more accurately at smaller floc sizes when the slope of the relationship between $d_{\mathrm{mean},3}$ and $d_{\mathrm{mean},2}$ is smaller.

Equation 6.6 can be used to calculate floc volume from the 2D data as follows. The diameter d is obtained by transforming the 2D $d_{\mathrm{mean},2}$ to the 3D $d_{\mathrm{mean},3}$ using the fit shown in Figure 6.5(A) and the linear relationship between D_2 and D_3 is obtained from the fit shown in 6.8. The shape factors are assumed to be 0.8 for flocs (from aspect ratio) and 1.0 for primary particles (roughly spherical). The packing factor, ζ, is assumed to be 0.64 or a fitting parameter. Equation 6.6 models

the data very well above floc volumes of 10^5 μm^3 or greater. Nonetheless, at smaller floc sizes Equation 6.6 still produced a much better estimate of the 3D floc volume than either of Equations 6.8 or 6.1. It is noted that the fit quality of Equation 6.6 was not very sensitive to the parameters ζ, ξ and ξ_0, because an improved fit was not obtained after an informal parameter sweep (results not shown).

6.5.3 Estimation of floc volume from settling video images

In Figure 6.10, floc size measured from the settling videos are used to calculate floc volume using Equations 6.1 and 6.6. As noted above, the floc volume calculated using $d_{\text{mean},2}$ directly with the equation of a sphere will produce a much greater estimate than when using the 3D $d_{\text{mean},3}$, although they will be on the same trend line. It was assumed that the linear relationship between 2D and 3D floc size determined from Figure 6.5 could be used to estimate the 3D floc size from the 2D settling video data. Similarly, the 3D box counting dimension was calculated from the 2D values by applying the linear fit obtained in Figure 6.8.

While the floc volume estimates between Equations 6.1 and 6.6 appear to be small for smaller floc sizes in the log-log plot in Figure 6.10, there is approximately a 50 % relative differences at 10 μm floc size, which grows exponentially at larger floc sizes. Above 100 μm floc size, Equation 6.1 estimates the volume to be 10 times higher than with Equation 6.6. These differences are not negligible, and should be taken into consideration when calculating floc volume from 2D images. However, the conversion between the 2D and 3D properties was known in this case, and the question may be asked, why not just measure floc volume directly? While it would be impractical to measure the 3D properties of flocs for every sample that passes through the lab, characterization of representative samples to understand the 2D-3D relationship seems worthwhile considering the enormous impact such information can have on calculated floc volume, and thus any downstream calculations that require floc volume as an input.

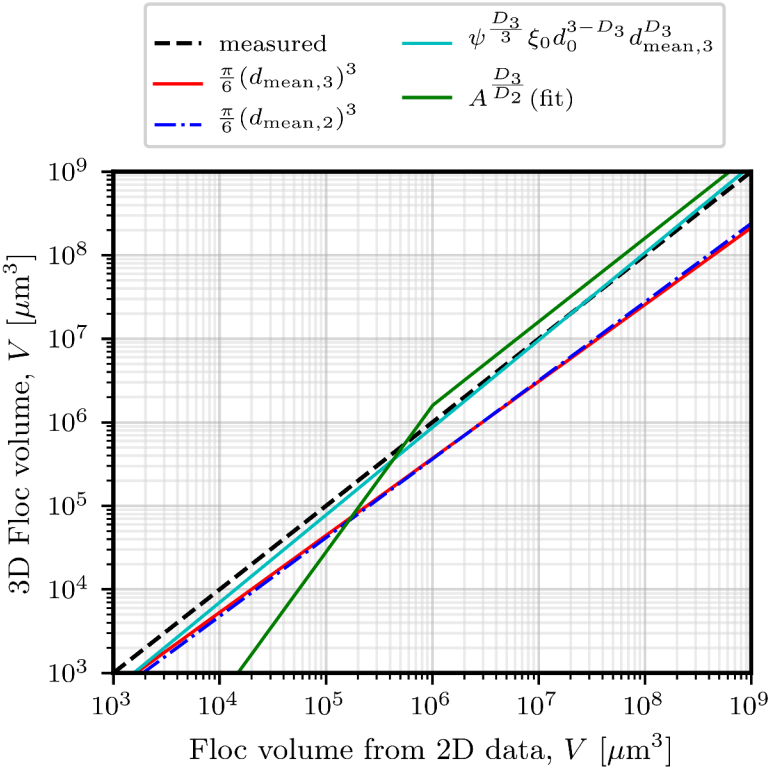

Figure 6.9: Quartz floc volume measured from 3D computed tomography images and compared with volume predictions from 2D measurements. The series labelled $A^{\frac{D_3}{D_2}}$ (fit), (Eq. 6.12) and Eq. 6.13 refer to the method by which the values for D_3 were determined from the 2D data.

6.6 Conclusions

The calculation of floc volume from 2D image data can be improved if the relationship between the 2D and 3D floc properties are known. In this study, a direct relationship between the 2D and 3D floc size and box counting dimension could be determined from the 3D images of flocs and simulated 2D projections. This permitted an improved floc volume estimate by incorporating the box counting dimension into the floc volume calculation (Equation 6.6), rather than using the most common method in the literature, which is to calculate floc volume with the equation of a sphere. Although the approach used in this study requires that relationship between the 2D and 3D floc properties is known, the magnitude of the volume estimate improvement (50 % at smaller floc sizes up to a 10-fold improvement at larger floc sizes) indicates that the effort to make such

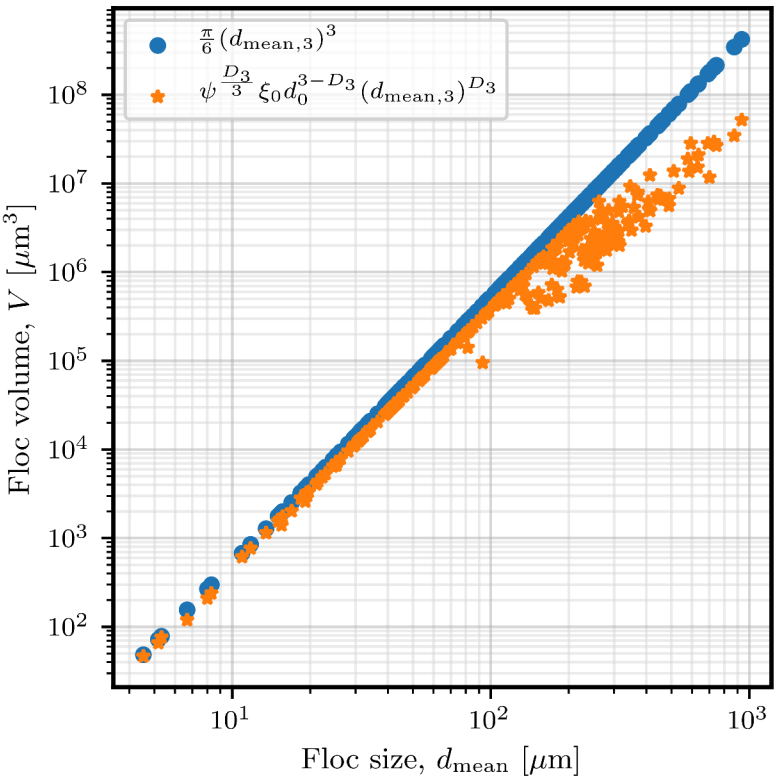

Figure 6.10: Floc volume estimates from floc settling images using the equation of a sphere and Equation 6.6.

measurements is worthwhile.

This chapter presented an auxiliary study to the main results in Chapters 4, 5, and 6. The approach to volume estimation helps to demonstrate how 3D measurement of floc properties can improve traditional settling column determinations of floc volume.

Chapter 7

Contributions to knowledge and future direction

7.1 Contributions to knowledge

This section describes the aspects of this thesis that may be considered original contributions to knowledge. The core developments of this thesis relate to methods for preparing flocculated systems on which calibrated X-ray computed tomography data can be acquired and interpreted in a quantitative manner. Once obtained, the data could be used to reveal novel insights about the structure and composition of flocculated systems.

1. **Polymer-stabilized quartz suspensions for X-ray CT calibration**. In Chapter 3, a method for the preparation of polymer-stabilized, watery quartz suspensions was described. This method permits the calibration of a CT for solids content in flocs. The method developed produced suspensions that showed negligible sedimentation over a two-hour period, which was sufficient to permit the acquisition of a CT scan ($\approx$ 1 hr) on the calibration specimens. It is foreseeable that this method could be used for other mineral in water calibration systems. For example, clay in water samples could be prepared; although it would be preferable to use a synthetic clay sample that does not absorb water. This contribution is critical to the use

of micro-CT in flocculated systems; because, despite correction factors, the output values of micro-CT are not always linearly related to linear attenuation. As such, a calibration is required for physically meaningful results.

2. **Measurement of changes in solids concentration distribution in floc beds as a function of applied pressure**. In Chapter 3, it was demonstrated by direct measurements that under low applied pressures, changes in the average solids content of a floc bed are caused by re-organization of the floc bed and expulsion of inter-floc water, rather than changes in floc density or solids content. This result is significant because it is counter to the mechanism of aggregate densification, as described in Chapter 5. As shown in Chapter 5, increased density of the aggregate phase (i.e. aggregate densification) does not occur until the inter-aggregate voids have mostly disappeared, which indicates that significantly higher force is required to trigger aggregate densification than assumed in the modified CR model.

3. **Quantitative approach to measurement of macro-floc structure**. In Chapter 4, a method was described for the quantitative assessment of the size and connectivity of sub-units within macro-flocs. While floc macro-structure has been described qualitatively from images in the literature, Chapter 4 represents the first attempt to quantitatively segment macro-floc structure from 3D images. A post-processing algorithm for the existing MBWT algorithm was developed, which can be applied to significantly improve the segmentation of touching components in 3D images with weak contrast. This may be seen as a critical development in the understanding of polymer-flocculated floc structures, because it shows that strength of medium- and large-sized flocs is related to floc macro-structure, and that breakage of such flocs likely occurs on low-ϕ fault lines that delineate the structure.

4. **Demonstration of the possible role of floc breakage in an industrial thickener.** In Chapter 5, the results from compressive rheology theory were reviewed with respect to the experimental results obtained in this thesis. The results suggested that consolidation in a thickener during the application of shear could be partially explained by aggregate breakage. This is an

important outcome for two reasons. First, it permits the introduction of another consolidation mechanism into the theory of compressive rheology; such that a mixture of aggregate breakage and aggregate densification are considered to contribute to consolidation. Second, the outcome permits a different conceptualization of the role of floc structure in the thickening process. If thickening is partially driven by breakage and re-organization of flocs, then flocculation strategies that produce flocs with desirable structural and breakage characteristics should be considered.

7.2 Future directions

Suggestions for future study based on the outcomes of this thesis are:

1. **Study floc macro-structure with higher resolution CT**. The use of $\leq 1\mu$m resolution CT would enable a clearer distinction between sub-units in a macro-floc structure. This research demonstrated a method for separating sub-units based on the available data, but higher resolution images may reveal a more nuanced structure. Nonetheless, the trade-off of reduced FOV must be considered.

2. **Study of floc bed compression at higher applied pressures**. In Chapter 3, pressures between 1 and 75 kPa were applied to obtain a maximum average solids content in the floc bed of ϕ=0.45. Yet, the breakage and permeability of the floc bed up to much higher solids content ($\phi > 0.8$) would be of interest, where increased solid content in the bed is more likely to occur by increases in the floc phase density. Representative samples could be obtained with high resolution CT ($\leq 1\mu$m). Although the FOV is significantly decreased at higher resolution, it is expected that the sediment bed is more homogeneous at higher ϕ, so a representative sample can be obtained with a smaller FOV.

3. **Study the relation between floc density measurements obtained from CT and calculated floc density measurements from settling experiments**. An attempt was made to do this

during collection of data for Chapter 6, but the results were not systematic. A direct comparison of CT and floc density values from settling experiments (by application of Stokes' Law) would be of interest to test widely reported trends of decreasing floc density with increasing floc size. Based on the CT measurements of floc density in this thesis, there did not appear to be a clear correlation between floc size and density.

4. **Experimentally confirm the occurrence of aggregate densification and breakage**. Measure ϕ-calibrated CT scans of samples of that are freshly flocculated, lightly sheared, and subjected to prolonged shear. Alternatively, optical image analysis of settling flocs (for ϕ estimate) or confocal laser scanning microscopy of immobilized flocs (for detailed structural analysis) could be used to support such a study.

5. **Discrete element sediment structure model**. Incorporating the concept of floc macrostructure into a model of the thickening process would help to demonstrate the link between floc structure, sediment bed structure, and consolidation due to applied shear. The inputs could be based on a combination of parameters measured from CT data, batch flocculation, and bench or pilot thickening experiments.

7.3 Limitations

A few limitations of this research are stated in this section. Compression experiments were carried out on a small scale, to permit the compression cell to fit into the X-ray CT equipment. It would be preferable to have had a compression cell with a larger radius (relative to the floc size) to reduce size wall effects. Nonetheless, the trends in the compressive behaviour of the flocs would be unchanged.

7.4 Conclusions

CT measurements may provide novel and deep insights into flocculated structures and other mineral systems if suitable calibrations are made and a quantitative approach to data measurement and

analysis is taken. That approach has been demonstrated throughout this thesis, with the direct conclusions from those studies written in each chapter.

Use of CT measurements in an experimental program is not without drawbacks, especially when applied to fragile, porous structures like flocs. As may be noted by the three different calibration methods applied in this thesis (one each in Chapter 3, Chapter 4 and Appendix A), a suitable calibration must exist or be developed to permit quantitative evaluation of composition from CT. Stability of flocs against breakage and degradation during sample preparation and X-ray CT scanning was an ongoing concern. This was mitigated with careful handling procedures, but introduces an almost unavoidable change in floc structure before measurements are even taken. Degradation of polymer-flocculated sediment beds was evident after prolonged exposure to X-ray energy during CT scanning. In the case of micro-CT measurements, it was possible to measure flocculated sediment beds (reported in Chapter 3). However, in the case of synchrotron-source CT, the amount of X-ray energy was significantly higher, and the sediment bed samples degraded much more rapidly. Although this meant that the original experimental plan to measure step-wise compression experiments of flocculated sediment beds with synchrotron CT would not succeed, it led to embedding of flocs in agar, which significantly stabilized flocs against degradation. This approach led to the evaluation of the macro-structure of quartz flocs presented in Chapter 4 and provided important evidence in the mechanism of floc breakage described in Chapter 5.

While the original contributions and future directions of this research are outlined in Section 7.1 and Section 7.2, a few points can be made about the new areas of research opened by this thesis. First, the demonstration of CT calibration and quantitative analysis encourages a more direct use of image analysis to elucidate the mechanisms of structural change. This contributes to the trend described in the background (Chapter 2), that improved knowledge of floc structure and composition has historically been linked to novel measurement technology and analytical methods. In the present work, flocs and flocculated sediment beds were studied but the methods demonstrated could be extended to other particulate systems.

The measurement procedures and analytical methods described in this thesis may be overly-

complicated for routine characterization work. Nonetheless, this thesis demonstrated the power of CT to help explain the micro-scale processes that contribute to macroscopically observable parameters. In the case of floc volume estimation, for example, Chapter 6 showed that volume estimates from 2D images can be improved, and significantly so for larger-sized flocs, by applying corrections from 3D measurements of the flocs. As such, CT may be considered as a method of augmenting traditional or routine measurements with micro-scale, 3D information about the system.

A widely repeated trend in floc research is that floc density decreases as floc size increases. Although not explicitly stated in this research, no such trend was observed in the CT data: flocs were more or less of similar ϕ content regardless of floc size. Such an observation challenges the widely accepted relationship of floc size and density and is a ripe topic for further investigation (indicated in Section 7.3 Item 3). The concept that floc density does not change much with size would be in line with a much earlier work by Wong et al. (1988), which showed that polymer-flocculated flocs have a highly ordered local micro-structure. By extension, aggregates of such flocs would have the same mass density at all scales, although the drag coefficient of larger flocs would be radically different, which would produce the commonly observed trend of decreased density with increased floc size.

Although the recommendation in Section 7.3 (1) seems to make the simple argument that a CT instrument with higher spatial resolution is better than CT measured at lower spatial resolution. There are two ways higher spatial resolution would contribute to the knowledge of floc structure. First, it could permit an improved segmentation of floc macro-structure. At 3.6 μm resolution (Chapter 5), the average floc sub-unit size was 90 μm and a macro-structure was identified in many, but not all flocs. With a higher resolution measurement, it may be possible to produce a more reliable segmentation of the macro-structure in a greater number of flocs. Second, with higher spatial resolution CT, it may be possible to observe and segment smaller scale structures that contribute to the overall floc structure. That could include the investigation of the micro-structure of individual micro-flocs, which could reveal new insights about floc formation and breakage.

Bibliography

Arinaitwe, E. and Pawlik, M. (2009). A method for measuring the degree of anionicity of polyacrylamide-based flocculants. *International Journal of Mineral Processing*, 91(1-2):50–54. 34

ASTM (1998). Standard test method for calibrating and measuring CT density E 1935 – 97. Technical report, United States.

Bache, D. H. (2004). Floc rupture and turbulence: A framework for analysis. *Chemical Engineering Science*, 59(12):2521–2534. 47, 83, 95

Baker, D. R., Mancini, L., Polacci, M., Higgins, M. D., Gualda, G. A. R., Hill, R. J., and Rivers, M. L. (2012). An introduction to the application of X-ray microtomography to the three-dimensional study of igneous rocks. *Lithos*, 148:262–276. 24

Baranau, V. and Tallarek, U. (2014a). On the jamming phase diagram for frictionless hard-sphere packings. *Soft Matter*, 10(39):7838–7848. 41

Baranau, V. and Tallarek, U. (2014b). Random-close packing limits for monodisperse and polydisperse hard spheres. *Soft Matter*, 10(21):3826–3841. 88

Berger, M., Hubbel, J., Seltzer, S., and Cousey, J.S. Zucker, D. (1999). XCOM: Photon Cross Sections Database. 25, 26, 56

Beyerer, J., León, F. P., and Frese, C. (2015). *Machine vision: Automated visual inspection: Theory, practice and applications*. Springer. 154

Burnett, T. L., McDonald, S. A., Gholinia, A., Geurts, R., Janus, M., Slater, T., Haigh, S. J., Ornek, C., Almuaili, F., Engelberg, D. L., Thompson, G. E., and Withers, P. J. (2014). Correlative tomography. *Scientific Reports*, 4(1):1–6. 131

Buscall, R., Mills, P. D. A., Stewart, R. F., Sutton, D., White, L. R., and Yates, G. E. (1987). The rheology of strongly-flocculated suspensions. *Journal of Non-Newtonian Fluid Mechanics*, 24(2):183–202. 16, 83

Buscall, R. and White, L. (1987). The Consolidation of Concentrated Suspenions: Part 1. - The Theory of Sedimentation. *Journal of the Chemical Society, Faraday Transactions 1: Physical Chemistry in Condensed Phases*, 83(3):873–891. 5, 11

Bushell, G. C., Yan, Y. D., Woodfield, D., Raper, J., and Amal, R. (2002). On techniques for the measurement of the mass fractal dimension of aggregates. *Advances in Colloid and Interface Science*, 95(1):1–50. 18, 21, 72, 99

Chakraborti, R. K., Gardner, K. H., Atkinson, J. F., and Van Benschoten, J. E. (2003). Changes in fractal dimension during aggregation. *Water Research*, 37(4):873–883. 16, 19, 20

Chu, C. P., Lee, D. J., and Peng, X. F. (2004). Structure of conditioned sludge flocs. *Water Research*, 38(8):2125–2134. 20

Cnudde, V. and Boone, M. N. (2013). High-resolution X-ray computed tomography in geosciences: A review of the current technology and applications. *Earth-Science Reviews*, 123:1–17. 22, 23

Concha, F. A. (2013). *Solid-Liquid Separation in the Mining Industry*. Springer International Publishing. xiv, 6, 12

Curran, K. J., Hill, P. S., Milligan, T. G., Mikkelsen, O. A., Law, B. A., Durrieu de Madron, X., Bourrin, F., Madron, X. D. D., and Bourrin, F. (2007). Settling velocity, effective density, and mass composition of suspended sediment in a coastal bottom boundary layer, Gulf of Lions, France. *Continental Shelf Research*, 27(10-11):1408–1421. 18, 95

Davis, G. R., Evershed, A. N. Z., and Mills, D. (2015). Characterisation of materials: determining density using X-ray microtomography. *Materials Science and Technology*, 31(2):162–166. 26

de Kretser, R. G., Boger, D. V., and Scales, P. J. (2003). Compressive rheology: an overview. *Rheology Reviews*, pages 125–165. 29

de Kretser, R. G., Usher, S. P., Scales, P. J., Boger, D. V., and Landman, K. a. (2001). Rapid filtration measurement of dewatering design and optimization parameters. *American Institute of Chemical Engineers Journal*, 47(8):1758–1769. 72

Dong, J., Lin, C. L., and Miller, J. D. (2018). Simulated permeability of flocculated kaolinite sediments from X-ray tomographic images. *Minerals & Metallurgical Processing*, 35(1):13–18. 11, 26

Droppo, I. G., Flannigan, D. T., Leppard, G. G., Jaskot, C., and Liss, S. N. (1996). Floc stabilization for multiple microscopic techniques. *Applied and Environmental Microbiology*, 62(9):3508–3515. 22, 52

Duchesne, M. J., Moore, F., Long, B. F., and Labrie, J. (2009). A rapid method for converting medical computed tomography scanner topogram attenuation scale to Hounsfield Unit scale and to obtain relative density values. *Engineering Geology*, 103(3-4):100–105. 25

Eisma, D., Schuhmacher, T., Boekel, H., Van Heerwaarden, J., Franken, H., Laan, M., Vaars, A., Eijgenraam, F., and Kalf, J. (1990). A camera and image-analysis system for in situ observation of flocs in natural waters. *Netherlands Journal of Sea Research*, 27(1):43–56. 9

Estrada, N. (2016). Effects of grain size distribution on the packing fraction and shear strength of frictionless disk packings. *Physical Review E*, 94(6):062903. 87

Expósito, P. L., Blanco, A., and Negro, C. (2017). Estimating fractal dimension of microalgal flocs through confocal laser scanning microscopy and computer modelling. *Algal Research*, 28:74–79. 20, 104

Fan, H., Liu, X., Wang, H. H., Han, Y., Qi, L., and Wang, H. H. (2017). Oxygen transfer dynamics and activated sludge floc structure under different sludge retention times at low dissolved oxygen concentrations. *Chemosphere*, 169:586–595. 20

Farrow, J. B., Johnston, R. R. M., Simic, K., and Swift, J. D. (2000). Consolidation and aggregate densification during gravity thickening. *Chemical Engineering Journal*, 80(1-3):141–148. 13, 14, 15, 80, 86, 87, 90

Farrow, J. B. and Swift, J. D. (1996). A new procedure for assessing the performance of flocculants. *International Journal of Mineral Processing*, 46(3-4):263–275. 47

Feenstra, T. P. and de Bruyn, P. L. (1980). Light scattering studies on solutions containing calcium phosphates. *Journal of Colloid And Interface Science*, 73(2):431–437. 18

Florio, B. J., Fawell, P. D., and Small, M. (2019). The use of the perimeter-area method to calculate the fractal dimension of aggregates. *Powder Technology*, 343:551–559. 20

Frank, E., Hall, M. A., and Witten, I. H. (2016). The WEKA Workbench. In *Data Mining: Practical Machine Learning Tools and Techniques*, page Online Appendix. Morgan Kaufmann, fourth edition. 97

Franks, G. V. and Zhou, Y. (2010). Relationship between aggregate and sediment bed properties: Influence of inter-particle adhesion. *Advanced Powder Technology*, 21(4):362–373. 8

Gan, M., Gopinathan, N., Jia, X., and Williams, R. A. (2004). Predicting packing characteristics of particles of arbitrary shapes. *KONA Powder and Particle Journal*, 22:82–93. 88

Ganczarczyk, J. J., Zahid, W. M., and Li, D. H. (1992). Physical stabilization and embedding of microbial aggregates for light microscopy studies. *Water Research*, 26(12):1695–1699. 23

Gillerman, V. S. and Bennett, E. H. (2011). Idaho Mining and Exploration S-11-1. Technical report, Idaho Geological Survey. 129

Gladman, B., de Kretser, R. G., Rudman, M., and Scales, P. J. (2005). Effect of shear on particulate suspension dewatering. *Chemical Engineering Research and Design*, 83(A7):933–936. 12

Gladman, B., Usher, S. P., and Scales, P. J. (2006). Compressive rheology of aggregated particulate suspensions. *Korea-Australia Rheological Journal*, 18(4):191–197. 29

Glasgow, L. A. (2003). Deformation of individual aggregates and flocs. *Journal of Dispersion Science and Technology*, 24(5):715–720. 29, 83

Glenn, C., Föllmi, K., Riggs, S., Baturin, G., Grimm, K., Trappe, J., Abed, A., Galli-Olliver, C., Garrison, R., Ilyin, A., and Jehl, C. (1994). Phosphorus and phosphorites: sedimentology and environments of formation. *Eclogae Geologicae Helvetiae*, 87(3):747–788. 138

Gmachowski, L. (2002). Calculation of the fractal dimension of aggregates. *Colloids and Surfaces A: Physicochemical and Engineering Aspects*, 211(2-3):197–203. 19

Goodarz-Nia, I. (1975). Floc simulation. Effect of particle size distribution. *Journal of Colloid And Interface Science*, 52(1):29–40. 17

Gorczyca, B. (2000). *Porosity and Structure of Alum Coagulation and Activated Sludge Flocs*. Ph.d., University of Toronto. 8

Gorczyca, B. and Ganczarczyk, J. (1999). Structure and porosity of alum coagulation flocs. *Water Quality Research Journal*, 34(4):653–666. 9, 102

Govedarica, A., Bacca, E. J. M., and Trifkovic, M. (2020). Structural investigation of tailings flocculation and consolidation via quantitative 3D dual fluorescence/reflectance confocal microscopy. *Journal of Colloid and Interface Science*, 571:194–204. 10, 21

Grady, L. (2006). Random walks for image segmentation. *IEEE Transactions on Pattern Analysis and Machine Intelligence*, 28(11):1768–1783. 36

Gulbrandsen, R. and Krier, D. (1980). *Large and rich phosphorus resources in the phosphoria formation in the Soda Springs area, Southeastern Idaho (no. 1496)*. US Government Printing Office. 130, 146, 148, 149

Hapca, S. M., Wang, Z. X., Otten, W., Wilson, C., and Baveye, P. C. (2011). Automated statistical method to align 2D chemical maps with 3D X-ray computed micro-tomographic images of soils. *Geoderma*, 164(3-4):146–154. 23, 27

He, W., Nan, J., Li, H., and Li, S. (2012). Characteristic analysis on temporal evolution of floc size and structure in low-shear flow. *Water Research*, 46(2):509–520. 16

Heinson, W. R., Chakrabarti, A., and Sorensen, C. M. (2015). Divine proportion shape invariance of diffusion limited cluster-cluster aggregates. *Aerosol Science and Technology*, 49(9):786–792. 19

Hiatt, E. E. and Budd, D. A. (2001). Sedimentary phospate formation in warm shallow waters: New insights into the palaeoceanography of the Permian Phosphoria Sea from analysis of phosphate oxygen isotopes. *Sedimentary Geology*, 145(1-2):119–133. 129

Hogg, R. (2000). Flocculation and dewatering. *International Journal of Mineral Processing*, 58(1-4):223–236. 7, 13

Hubbell, J. H. and Seltzer, S. M. (2004). Tables of X-Ray Mass Attenuation Coefficients and Mass Energy-Absorption Coefficients from 1 keV to 20 MeV for Elements Z = 1 to 92 and 48 Additional Substances of Dosimetric Interest. In *X-Ray Mass Attenuation Coefficients, NIST Standard Reference Database 126*. National Institute of Standards and Technology, Gaithersburg, MD. 56

Hunt, B. R. and Kaloshin, V. Y. (1997). How projections affect the dimension spectrum of fractal measures. *Nonlinearity*, 10(5):1031–1046. 21, 93

Iassonov, P., Gebrenegus, T., and Tuller, M. (2009). Segmentation of X-ray computed tomography images of porous materials: A crucial step for characterization and quantitative analysis of pore structures. *Water Resources Research*, 45(9):1–12. 154

Jarvis, P., Jefferson, B., Gregory, J., and Parsons, S. A. (2005a). A review of floc strength and breakage. *Water research*, 39(14):3121–3137. 9, 41, 47

Jarvis, P., Jefferson, B., and Parsons, S. A. (2005b). Measuring floc structural characteristics. *Reviews in Environmental Science and Biotechnology*, 4(1-2):1–18. 8, 55, 73, 83, 93, 94, 99, 101

Jiao, H., Wu, Y., Wang, H., Chen, X., Li, Z., Wang, Y., Zhang, B., and Liu, J. (2021). Micro-scale mechanism of sealed water seepage and thickening from tailings bed in rake shearing thickener. *Minerals Engineering*, 173:107043. 11

Johnson, B. D. and Wangersky, P. J. (1985). A recording backward scattering meter and camera system for examination of the distribution and morphology of macroaggregates. *Deep Sea Research Part A, Oceanographic Research Papers*, 32(9):1143–1150. 18

Jussiani, E. I., dos Reis, P. J., and Appoloni, C. R. (2016). Determining chemical composition of materials through micro-CT images. *Micron*, 89:9–15. 26

Kim, J. G., Jin, S. O., Cho, M. H., and Lee, S. Y. (2011). Inter-plane artifact suppression in tomosynthesis using 3D CT image data. *Biomedical engineering online*, 10(1):1–15. xiv, 24

Klein, S., Staring, M., Murphy, K., Viergever, M. A., and Pluim, J. P. (2010). Elastix: A toolbox for intensity-based medical image registration. *IEEE Transactions on Medical Imaging*, 29(1):196–205. 135

Klimpel, R. C. and Hogg, R. (1986). Effects of flocculation conditions on agglomerate structure. *Journal of colloid and interface science*, 113(1):121–131. xiv, 8, 9, 18, 19, 72

Klimpel, R. C. and Hogg, R. (1991). Evaluation of floc structures. *Colloids and Surfaces*, 55:279–288. 8, 73, 83

Knudsen, A. C. and Gunter, M. E. (2004). Life Cycle of the Phosphoria Formation: From Deposition to Post-Mining Environment. In Hein, J., editor, *Handbook of Exploration and Environmental Geochemistry*, volume 8, chapter 7, pages 169–187. Elselvier, B.V. 137

Knudsen, A. C., Gunter, M. E., Herring, J. R., and Grauch, R. I. (2002). Mineralogical characterization of weathered and less weathered strata of the Meade Peak phosphatic shale member of the Permian Phosphoria Formation; measured sections E and F, Rasmussen Ridge, and measured sections G and H. Technical report, US Geological Survey. 137, 148

Koivuranta, E., Stoor, T., Hattuniemi, J., and Niinimäki, J. (2015). On-line optical monitoring of activated sludge floc morphology. *Journal of Water Process Engineering*, 5:28–34. 18

Konrad, J., Wang, M., Ishwar, P., Wu, C., and Mukherjee, D. (2013). Learning-based, automatic 2D-to-3D image and video conversion. *IEEE Transactions on Image Processing*, 22(9):3485–3496. 94

Kranenburg, C. (1994). The fractal structure of cohesive sediment aggregates. *Estuarine, Coastal and Shelf Science*, 39(6):451–460. 88

Lagvankar, A. L. and Gemmell, R. S. (1968). A Size-Density Relationship for Flocs. *Journal American Water Works Association*, 60(9):1040–1046. 17

Landman, K. and White, L. (1994). Solid/liquid separation of flocculated suspensions. *Advances in Colloid and Interface Science*, 51:175–246. 11, 30, 41

Lapuerta, M., Martos, F. J., and Martín-González, G. (2010). Geometrical determination of the lacunarity of agglomerates with integer fractal dimension. *Journal of Colloid and Interface Science*, 346(1):23–31. 19

Latham, S., Varslot, T., and Sheppard, A. (2008). Image registration: enhancing and calibrating X-ray micro-CT imaging. In *Proceedings of International Symposium of the Society of Core Analysts*, pages 1–12, Abu Dhabi, UAE. Society of Core Analysts. 27

Lau, S. H., Miller, J., and Lin, C.-L. (2012). 3D mineralogy, texture and damage analysis of multiphase mineral particles with a high contrast, submicron resolution x-ray tomography system. In *26th International Mineral Processing Congress, IMPC 2012: Innovative Processing for Sustainable Growth - Conference Proceedings*, pages 2726–2736, New Delhi, India. 27

Lee, C. and Kramer, T. A. (2004). Prediction of three-dimensional fractal dimensions using the two-dimensional properties of fractal aggregates. *Advances in Colloid and Interface Science*, 112(1-3):49–57. 15, 105

Lessard, J., Sweetser, W., Bartram, K., Figueroa, J., and McHugh, L. (2016). Bridging the gap: Understanding the economic impact of ore sorting on a mineral processing circuit. *Minerals Engineering*, 91:92–99. 130

Lester, D. R., Usher, S. P., and Scales, P. J. (2005). Estimation of the hindered settling function from batch-settling tests. *American Institute of Chemical Engineers Journal*, 51(4):1158–1168. 1

Lewin, S., Barba, A., Persson, C., Franch, J., Ginebra, M.-P., and Öhman-Mägi, C. (2017). Evaluation of bone formation in calcium phosphate scaffolds with uCT-method validation using SEM. *Biomedical Materials*, 12(6):065005. 27

Li, D. H. and Ganczarczyk, J. J. (1990). Structure of activated sludge flocs. *Biotechnology and Bioengineering*, 35(1):57–65. 22

Liss, S. N., Droppo, I. G., Flannigan, D. T., and Leppard, G. G. (1996). Floc architecture in wastewater and natural riverine systems. *Environmental Science and Technology*, 30(2):680–686. 22

Liu, Q., Zhang, Y., and Laskowski, J. S. (2000). The adsorption of polysaccharides onto mineral surfaces: an acid/base interaction. *International Journal of Mineral Processing*, 60(3-4):229–245. 7

Logan, B. E., Jiang, Q., and Logan, B. E. (1991). Fractal Dimensions of Aggregates Determined from Steady-State Size Distributions. *Environmental Science and Technology*, 25(12):2031–2038. 95, 96

Lorensen, W. E. and Cline, H. E. (1987). Marching cubes: A high resolution 3D surface construction algorithm. *ACM SIGGRAPH Computer Graphics*, 21(4):163–169. 162

Löwer, E., Makowlew, C., Leißner, T., and Peuker, U. A. (2021). Wetting behavior of porous structures: Three-dimensional determination of the contact angle after filter cake dewatering using X-ray microscopy. *Advances in Water Resources*, 151:103894. 11

MacIver, M. R. and Pawlik, M. (2017a). Analysis of in situ microscopy images of flocculated sediment volumes. *Chemical Engineering and Technology*, 40(12):2305–2313. 41

MacIver, M. R. and Pawlik, M. (2017b). Measurement of optical backscattering height scans from flocculated mineral sediments. *Colloids and Surfaces A: Physicochemical and Engineering Aspects*, 514:38–46. 41

MacIver, M. R., Pawlik, M., Hamza, H., and Malin, L. (2018). Networked structure analysis with micro-CT method. In *30th International Mineral Processing Congress Proceedings*, pages 1–8, Moscow, Russia. 82

Maggi, F. and Winterwerp, J. C. (2004). Method for computing the three-dimensional capacity dimension from two-dimensional projections of fractal aggregates. *Physical review. E, Statistical, nonlinear, and soft matter physics*, 69(1):11405. 20, 104

Mandelbrot, B. B. (1975). *Les objets fractals: forme, hasard et dimension*. Flammarion, Paris. 18

Mandelbrot, B. B. (1982). *The fractal geometry of nature*, volume 1. WH freeman, New York. 20

Mandelbrot, B. B., Passoja, D. E., and Paullay, A. J. (1984). Fractal character of fracture surfaces of metals. *Nature*, 308(5961):721–722. 20

Mashiatulla, M., Ross, R. D., and Sumner, D. R. (2017). Validation of cortical bone mineral density distribution using micro-computed tomography. *Bone*, 99:53–61. 25, 26

Maughan, E. (1984). Geological setting and some geochemistry of petroleum source rocks in the Permian Phosphoria Formatoin. In Woodward, J., Meissner, F., and Clayton, J., editors, *Hydrocarbon Source Rocks of the Greater Rocky Mountain Region*, pages 281–294. Rocky Mountain Association of Geologists, Denver, USA. 137

McArthur, J. M. (1985). Francolite geochemistry — compositional controls during formation, diagenesis , metamorphism and weathering. *Geochimica et Cosmochimica Acta*, 49(1):23–35. 148

McClellan, G. H. and Van Kauwenbergh, S. J. (1990). Mineralogy of sedimentary apatites. *Geological Society, London, Special Publications*, 52(1):23–31. 129, 130, 138, 148

Meakin, P. (1987). Fractal aggregates. *Advances in Colloid and Interface Science*, 28(C):249–331. 20

Medalia, A. I. (1970). Morphology of aggregates VI. Effective volume of aggregates of carbon black from electron microscopy; Application to vehicle absorption and to die swell of filled rubber. *Journal of Colloid And Interface Science*, 32(1):115–131. 17, 95

Mendez, R., Romanski, F. S., and Tomassone, M. S. (2011). Density behavior of cohesive granular materials. *Powder Technology*, 211(2-3):189–198. 25

Miller, H., Zhou, Z., Hell, S. W., Sahl, S. J., Bates, M., Laine, R. F., Kaminski, G. S., Pujals, S., and Albertazzi, L. (2018). The 2018 correlative microscopy techniques roadmap. *Journal of Physics D: Applied Physics*, 51(44):443001. 26

Mills, P. D. A., Goodwin, J. W., and Grover, B. W. (1991). Shear field modification of strongly flocculated suspensions - aggregate morphology. *Colloid and Polymer Science*, 269(9):949–963. 13, 103

Mueller, G. E. (2005). Numerically packing spheres in cylinders. *Powder Technology*, 159(2):105–110. 48

Mueller, J. A., Morand, J., and Boyle, W. C. (1967). Floc sizing techniques. *Applied Microbiology*, 15(1):125–134. 17, 22

Mulder, L., Koolstra, J. H., and Van Eijden, T. M. (2004). Accuracy of microCT in the quantitative determination of the degree and distribution of mineralization in developing bone. *Acta Radiologica*, 45(7):769–777. 26, 149

Munro, D., Goodall, A. R., Wilkinson, M. C., Randle, K., and Hearn, J. (1979). Study of particle nucleation, flocculation, and growth in the emulsifier-free polymerization of styrene in water by total intensity light scattering and photon correlation spectroscopy. *Journal of Colloid And Interface Science*, 68(1):1–13. 17

Nasser, M. S. (2014). Characterization of floc size and effective floc density of industrial papermaking suspensions. *Separation and Purification Technology*, 122:495–505. 15

Neubert, P. and Protzel, P. (2014). Compact watershed and preemptive SLIC: On improving trade-offs of superpixel segmentation algorithms. In *22nd International Conference on Pattern Recognition*, pages 996–1001. IEEE. 54

Orhan, O., Haffner-Staton, E., La Rocca, A., and Fay, M. (2016). Characterisation of flame-generated soot and soot-in-oil using electron tomography volume reconstructions and comparison with traditional 2D-TEM measurements. *Tribology International*, 104:272–284. 21, 93, 94

Owen, A. T., Fawell, P. D., Swift, J. D., Labbett, D. M., Benn, F. A., and Farrow, J. B. (2008). Using turbulent pipe flow to study the factors affecting polymer-bridging flocculation of mineral systems. *International Journal of Mineral Processing*, 87(3-4):90–99. 47

Palubinskas, G. (2017). Image similarity/distance measures: what is really behind MSE and SSIM? *International Journal of Image and Data Fusion*, 8(1):32–53. 136

Pashminehazar, R., Ahmed, S. J., Kharaghani, A., and Tsotsas, E. (2018). Spatial morphology of maltodextrin agglomerates from X-ray microtomographic data: Real structure evaluation vs . spherical primary particle model. *Powder Technology*, 331:204–217. 21, 71

Piccinini, F., Tesei, A., Arienti, C., and Bevilacqua, A. (2015). Cancer multicellular spheroids: Volume assessment from a single 2D projection. *Computer Methods and Programs in Biomedicine*, 118(2):95–106. 94

Prevrhal, S. (2005). *Quantitative micro-CT*, volume 5923. SPIE. 26

Ramandi, H. L., Mostaghimi, P., and Armstrong, R. T. (2017). Digital rock analysis for accurate prediction of fractured media permeability. *Journal of Hydrology*, 554:817–826. 27

Ramesh, P. S. and Letitia, S. (2019). An evaluation framework for auto-conversion of 2D to 3D video streaming using depth profile and pipelining technique in handheld cellular devices. *Cluster Computing*, 22(5):11741–11753. 93

Rattanakawin, C. and Hogg, R. (2001). Aggregate size distributions in flocculation. *Colloids and Surfaces A: Physicochemical and Engineering Aspects*, 177(2-3):87–98. 32

Salzman, D. B. (1990). A method of general moments for orienting 2D projections of unknown 3D objects. *Computer Vision, Graphics and Image Processing*, 50(2):129–156. 94

Scales, P., Kumar, A., Van Deventer, B. G., Stickland, A. D., and Usher, S. (2012). Compressional dewatering of flocculated mineral suspensions. In *26th International Mineral Processing Congress (IMPC)*, New Delhi, India. Indian Institute of Metals. 12

Schneider, C. A., Rasband, W. S., and Eliceiri, K. W. (2012). NIH Image to ImageJ: 25 years of image analysis. *Nature Methods*, 9(7):671–675. 154

Schroeder, W., Martin, K., and Lorensen, B. (2006). *The VTK: an object-oriented approach to 3D graphics*. Kitware. 154

Selomulya, C., Jia, X., and Williams, R. A. (2005). Direct prediction of structure and permeability of flocculated structures and sediments using 3D tomographic imaging. *Chemical Engineering Research and Design*, 83(A7):844–852. 11

Serra, T. and Casamitjana, X. (1998). Structure of the aggregates during the process of aggregation and breakup under a shear flow. *Journal of Colloid and Interface Science*, 206(2):505–511. 96

Shakeel, A., MacIver, M. R., van Kan, P. J., Kirichek, A., and Chassagne, C. (2021). A rheological and microstructural study of two-step yielding in mud samples from a port area. *Colloids and Surfaces A: Physicochemical and Engineering Aspects*, 624:126827. 97

Sharma, S., Lin, C. L., and Miller, J. D. (2017). Multi-scale features including water content of polymer induced kaolinite floc structures. *Minerals Engineering*, 101:20–29. 9, 11, 23, 26, 71

Sharp, T. A., Merkel, M., Manning, M. L., and Liu, A. J. (2019). Inferring statistical properties of 3D cell geometry from 2D slices. *PLOS ONE*, 14(2):1–18. 94

Shen, X. and Maa, J. (2016). A camera and image processing system for floc size distributions of suspended particles. *Marine Geology*, 376:132–146. 18

Shenker, O. R. (1994). Fractal geometry is not the geometry of nature. *Studies in History and Philosophy of Science*, 25(6):967–981. 19

Sis, H. and Chander, S. (2003). Reagents used in the flotation of phosphate ores: A critical review. *Minerals Engineering*, 16(7):577–585. 130

Slater, R. W. and Kitchener, J. A. (1966). Characteristics of flocculation of mineral suspensions by polymers. *Discussions of the Faraday Society*, 42:267–275. 17

Smellie, R. H. and La Mer, V. K. (1958). Flocculation, subsidence and filtration of phosphate slimes. VI. A quantitative theory of filtration of flocculated suspensions. *Journal of Colloid Science*, 13(6):589–599. 17

Snidaro, D., Zartarian, F., Jorand, F., Bottero, J.-Y., Block, J.-C., and Manem, J. (1997). Characterization of activated sludge flocs structure. *Water Science & Technology*, 36(4):313–320. 9

Soille, P. (1999). *Morphological Image Analysis Principles and Applications*, volume 2. Springer, Berlin. 154

Soille, P. and Vincent, L. M. (1990). Determining watersheds in digital pictures via flooding simulations. In *Visual Communications and Image Processing '90: Fifth in a Series*, volume 1360, pages 240–250. SPIE. 54

Somasundaran, P., Huang, Y. B., and Gryte, C. G. (1987). CAT scan characterization of sedimentation and floccs. *Powder Technology*, 53(1):73–77. 21

Spehar, R., Kiviti-Manor, A., Fawell, P., Usher, S. P., Rudman, M., and Scales, P. J. (2015). Aggregate densification in the thickening of flocculated suspensions in an un-networked bed. *Chemical Engineering Science*, 122:585–595. 1, 30, 73

Spencer, K. L., Wheatland, J. A., Bushby, A. J., Carr, S. J., Droppo, I. G., and Manning, A. J. (2021). A structure–function based approach to floc hierarchy and evidence for the non-fractal nature of natural sediment flocs. *Scientific Reports*, 11(1):14012. 11, 19

Spicer, P. T. and Pratsinis, S. E. (1996). Shear-induced flocculation: the evolution of floc structure and the shape of the size distribution at steady state. *Water Research*, 30(5):1049–1056. 20, 70

Stickland, A. D. and Buscall, R. (2009). Whither compressional rheology? *Journal of Non-Newtonian Fluid Mechanics*, 157(3):151–157. 11

Sun, W., Lam, K., and Li, X. (2016). Characterization of the deformable feature of bio-flocs and its impact on mass transport using laser-based imaging techniques. *Colloids and Surfaces A: Physicochemical and Engineering Aspects*, 509:166–173. 18, 95

Sutherland, D. N. (1967). A theoretical model of floc structure. *Journal of Colloid And Interface Science*, 25(3):373–380. 17

Syvitski, J., Asprey, K., and Heffler, D. (1991). *The Floc Camera: A three-dimensional imaging system of suspended particulate matter*. Springer, New York, NY. 18, 21

Syvitski, J. P. M. and Hutton, E. W. H. (1997). FLOC: Image analysis of marine suspended particles. *Computers and Geosciences*, 23(9):967–974. 18, 95, 99

Taguchi, K. (2013). *Image reconstruction algorithms for X-ray CT*. Taylor & Francis, 1st edition. 25

Tambo, N. and Watanabe, Y. (1978). Physical characteristics of flocs - I. The floc density function and alumnium floc. *Water Research*, 13:409–419. 18

Thill, A., Veerapaneni, S., Simon, B., Wiesner, M., Bottero, J. Y., and Snidaro, D. (1998). Determination of structure of aggregates by confocal scanning laser microscopy. *Journal of Colloid and Interface Science*, 204(2):357–362. 104

Thomas, D. (1963). Transport characteristics of suspensions VII. Relation of hindered-settling floc characteristics to rheological parameters. *American Institute of Chemical Engineers Journal*, 9(3):310–316. 17

Tran, D., Kuprenas, R., and Strom, K. (2018). How do changes in suspended sediment concentration alone influence the size of mud flocs under steady turbulent shearing? *Continental Shelf Research*, 158:1–14. 18

U.S. Geological Survey (2017). Mineral commodities summary. Technical Report 703, U.S. Survey Geological. 129

Usher, S. P. and Scales, P. J. (2005). Steady state thickener modelling from the compressive yield stress and hindered settling function. *Chemical Engineering Journal*, 111(2-3):253–261. 1, 5, 11, 72

Usher, S. P., Spehar, R., and Scales, P. J. (2009). Theoretical analysis of aggregate densification: Impact on thickener performance. *Chemical Engineering Journal*, 151(1-3):202–208. 1, 10, 12, 30, 84, 86, 87, 91

Vahedi, A. and Gorczyca, B. (2010). Application of fractal dimensions to study the structure of flocs formed in lime softening process. *Water Research*, 45(2):545–556. 104

van Deventer, B., Usher, S. P., Kumar, A., Rudman, M., and Scales, P. J. (2011). Aggregate densification and batch settling. *Chemical Engineering Journal*, 171(1):141–151. 1, 12

Van Grieken, R. and Markowicz, A., editors (1993). *Handbook of X-ray spectrometry: Methods and techniques*. Marcel Dekker, Incorporated, New York, 2nd edition. 24

Vogelgesang, M., Chilingaryan, S., dos Santos Rolo, T., and Kopmann, A. (2012). UFO: A scalable GPU-based image processing framework for on-line monitoring. In *2012 IEEE 14th International Conference on High Performance Computing and Communication & 2012 IEEE 9th International Conference on Embedded Software and Systems*, pages 824–829, Liverpool, United kingdom. IEEE. 25, 53

Vold, M. J. (1963). Computer simulation of floc formation in a colloidal suspension. *Journal of Colloid Science*, 18(7):684–695. 8, 17, 73

Wang, C., Harbottle, D., Liu, Q., and Xu, Z. (2014). Current state of fine mineral tailings treatment: A critical review on theory and practice. *Minerals Engineering*, 58:113–131. 1

Weitz, D. A. (2004). Packing in the Spheres. *Science*, 303(5660):968–969. 87

Wheatland, J. A. T., Spencer, K. L., Droppo, I. G., Carr, S. J., and Bushby, A. J. (2020). Development of novel 2D and 3D correlative microscopy to characterise the composition and multiscale structure of suspended sediment aggregates. *Continental Shelf Research*, 200:104112. 10, 22

Wildenschild, D. and Sheppard, A. P. (2013). X-ray imaging and analysis techniques for quantifying pore-scale structure and processes in subsurface porous medium systems. *Advances in Water Resources*, 51:217–246. 25, 39, 148

Wildenschild, D., Vaz, C. M. P., Rivers, M. L., Rikard, D., and Christensen, B. S. B. (2002). Using X-ray computed tomography in hydrology: systems, resolutions, and limitations. *Journal of Hydrology*, 267(3-4):285–297. 26

Winterwerp, J. C. (2002). On the flocculation and settling velocity of estuarine mud. *Continental Shelf Research*, 22(9):1339–1360. 15

Wong, K., Cabane, B., and Somasundaran, P. (1988). Highly Ordered Microstructure of Flocculated Aggregates. *Colloids and Surfaces*, 30(2):355–360. 19, 115

Wopenka, B. and Pasteris, J. D. (2005). A mineralogical perspective on the apatite in bone. *Materials Science and Engineering C*, 25(2):131–143. 148

Wysokinski, T. W., Chapman, D., Adams, G., Renier, M., Suortti, P., and Thomlinson, W. (2015). Nuclear Instruments and Methods in Physics Research A Beamlines of the biomedical imaging and therapy facility at the Canadian light source – part 3. *Nuclear Inst. and Methods in Physics Research, A*, 775:1–4. 52

Xie, W. Q., Zhang, X. P., Yang, X. M., Liu, Q. S., Tang, S. H., and Tu, X. B. (2020). 3D size and shape characterization of natural sand particles using 2D image analysis. *Engineering Geology*, 279:105915. 94

Ye, Y. and Shan, J. (2014). A local descriptor based registration method for multispectral remote sensing images with non-linear intensity differences. *ISPRS Journal of Photogrammetry and Remote Sensing*, 90:83–95. 142

Yukselen, M. A. and Gregory, J. (2004). The reversibility of floc breakage. *International Journal of Mineral Processing*, 73(2-4):251–259. 13, 83

Zhang, Y., Grassia, P., Martin, A., Usher, S. P., and Scales, P. J. (2015). Mathematical modelling of batch sedimentation subject to slow aggregate densification. *Chemical Engineering Science*, 128:54–63. 73

Zhang, Y., Martin, A., and Grassia, P. (2013a). Mathematical modelling of time-dependent densified thickeners. *Chemical Engineering Science*, 99:103–112. 11

Zhang, Y., Martin, A., and Grassia, P. (2013b). Prediction of thickener performance with aggregate densification. *Chemical Engineering Science*, 101:346–358. 12

Zhou Wang, Bovik, A. C., Sheikh, H. R., and Simoncelli, E. P. (2004). Image quality assessment: from error visibility to structural similarity. *IEEE Transactions on Image Processing*, 13(4):600–612. 135

Appendix A

Apatite content and distribution in organic-rich particles

A.1 Introduction

Phosphorus is a critical element for all life on earth and the majority of it is derived from non-renewable resources. In the United States, as of 2018, about 15 % of the annual 32.7 Mton phosphate rock was produced by four mines in Caribou County, Idaho, which extract an organic-rich black shale from the apatite-rich Meade Peak member of the Permian Phosphoria Formation (U.S. Geological Survey, 2017; Gillerman and Bennett, 2011). Apatite is a group of the most commonly mined phosphate-containing minerals, with different composition and end-members OH, F and Cl, of which the general chemical formula is $Ca_{10}(PO_4)_6(OH,F,Cl)_2$. It is generally accepted that the phosphorites in the Phosphoria region were the result of an increase in biological and biogeochemical activity that occurred in the Permian Sea that covered today's western USA during the Permian Era (Hiatt and Budd, 2001). Extreme oceanic and climactic conditions of this period accelerated the deposition of phosphorous by two key mechanisms: primary phosphogenesis and granular phosphorite deposition and concentration (McClellan and Van Kauwenbergh, 1990). Bacterial phosphogenesis is thought to involve the release of phosphorus through the bacterial breakdown of organic matter, and the subsequent precipitation of carbonate-rich fluorapatite (Hiatt and Budd,

2001). As a result, the apatite from this region is often closely associated with a significant amount of residual organic matter (OM) and it is not unusual for samples to contain phosphatic peloids, coated grains, intraclasts, and phosphatized invertebrate shells.

Historically, the phosphate head grade in Mead Peak region averaged 27.7 wt. % P_2O_5 (Gulbrandsen and Krier, 1980), which could be upgraded to an intermediate, economically viable product with $>$ 28 wt. % P_2O_5 just by washing and sizing the ore. Today, with phosphate reserves declining, operators consider processing ore with a head grade below 20 wt. % P_2O_5. Such low-grade sedimentary phosphate ore contains gangue in the form of quartz, clay, organic matter, calcite and dolomite, which must be removed to upgrade the P_2O_5 content (Sis and Chander, 2003). For low-grade ores, washing and sizing alone may not improve the P_2O_5 content sufficiently, so other processes must be considered. Flotation is used to beneficiate more than half of the world's phosphate supply. However, a poor flotation response in organic-rich phosphate ores has been attributed by McClellan and Van Kauwenbergh (1990) to non-specific adsorption of reagents on organic-coated ore and gangue minerals. Calcining works well for carbonate-containing sedimentary phosphates, but its environmental impacts, including the release of particulate matter, CO_2, and SO_2, make it a less acceptable option.

Pre-concentration of phosphate ore is an alternative to remove gangue and low-grade material before it enters the comminution circuit. An example of this approach is sensor-based particle sorting, where a diverter is used to selectively remove waste particles based on a correlation between the particle grade and a measured signal (Lessard et al., 2016). Another approach may be to chemically pre-treat the ore in a way that improves the liberation of the apatite-bearing phase from gangue and OM, which could improve the flotation response of the material. While such alternatives may be proposed, their development requires a more detailed understanding of the nature and distribution of the phosphate-containing phase in the low-grade ore. To date, the interest of miners in the Phosphoria region was on processing high grade phosphate ore, where the variation in phosphate content within and between particles of a sample would not be as significant as the variations expected from a sample of lower grade particles.

In this chapter, a method is described to measure local variations in apatite concentration within individual low-grade ore particles with X-ray CT images. By identifying the volume of the phosphorous-rich (P-rich) phase, φ_P, in the sample (by CT-SEM correlation) and applying a CT calibration for apatite concentration to that P-rich phase, C_A [g of apatite per cm^3], it is possible to fully describe the distribution of apatite in each particle. Additionally, the mass fraction of apatite in each particle, w_A, may be determined from φ_P and C_A by:

$$w_A = \frac{C_A \varphi_P}{\rho}, \tag{A.1}$$

where ρ [g/cm^3] is the bulk density of the particles. For a perfect apatite crystal, $\varphi_P = 1$, $C_A = 3.2$ g of apatite per cm^3, $\rho = 3.2$ g/cm^3, and $w_A = 1$. In a multi-phase particle, $w_A < 1$, because at least one phase other than apatite is present in the particle. When $C_A < 3.2$ g/cm^3, the apatite content in the P-rich phase is less than that of the perfect apatite; $\varphi_P < 1$ because the phase(s) other than the P-rich phase occupy the remaining $1 - \varphi_P$ of the particle volume. This permits a statement of the apatite content within particles in terms of the quantity of the apatite-bearing phase (by φ_P) and the quality of that phase (by C_A.)

The workflow described in this chapter included two main steps: (1) image correlation between CT and scanning electron microscopy-energy dispersive X-ray images (SEM-EDX), followed by (2) CT calibration for apatite content. These two steps have been reported separately in previous studies, but the authors are not aware of any reports where they have been implemented in the same workflow. While the scope of this study was to develop the workflow and demonstrate the information obtainable thereby, it is conceivable that the results here could be treated as a calibration and applied to a greater number of particles.

A.2 Methods

Image correlation was a key method used in this study. The alignment of two or more images obtained from different sensors on the same region in space is referred to as image registration (in general) or correlative tomography (for volumetric images) (Burnett et al., 2014). The registration

of X-ray CT images to other image types is often conducted because volumetric CT data contain rich spatial information, but no explicit chemical or mineral information. The objective of image registration is a point-to-point or pixel-to-pixel alignment of two or more images, which differentiates it from qualitative image correlation approaches that produce a description of the features or trends in two or more measurements.

An overview of the CT-SEM image registration and calibration workflow used in this study is shown in Figure A.1.

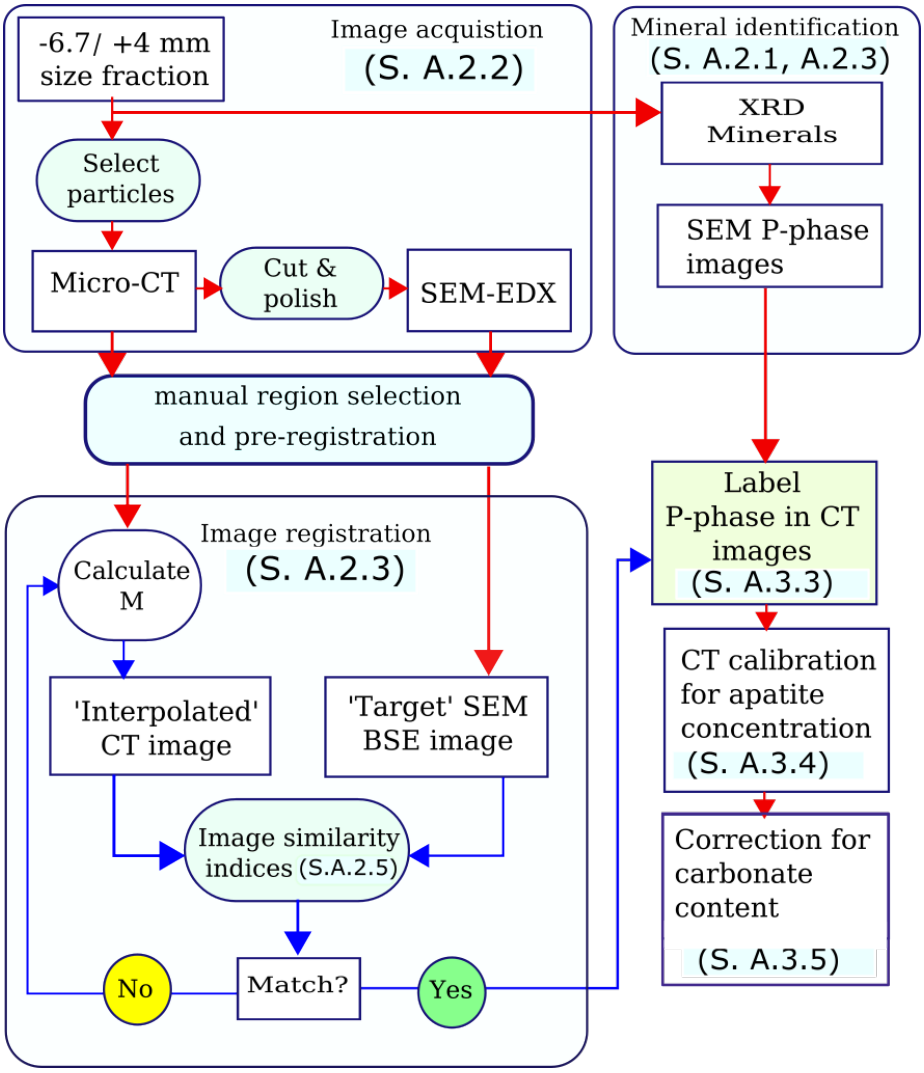

Figure A.1: Workflow to perform CT-SEM image registration and mineral phase assignment.

A.2.1 Sample characterization and preparation

A 20 kg sample of low-grade phosphate ore was received from an operating mine in Caribou County, Idaho, USA. The ore was split into 1 kg sub-samples, washed, deslimed, and classified by size. Five dark particles were selected from the - 6.7 mm/ + 4 mm size fraction of one of the sub-samples. This particle size range permitted the acquisition of CT images at the highest resolution (5 μm per voxel) the CT scanner was capable of. Only five samples were studied because the scope of this study was to develop the registration and calibration procedure.

Each particle was placed in a polyethylene (PE) sample vial for CT image acquisition. A narrow gauge PTFE tube (1/16" diameter) was placed vertically next to each particle in the sample vial, then the remainder of the PE tube volume was filled with epoxy and permitted to cure for 48 hours. A thin Al foil band was placed around each vial to delineate the region to be CT scanned. After CT scanning, each sample was ground with a fine grit metallurgical paper to the mid-point of the CT-scanned region.

The - 6.7 mm/ + 4 mm size fraction was assayed by quantitative X-ray diffraction (XRD) and by atomic emission spectroscopy with inductively coupled plasma (AES-ICP). Total organic carbon (TOC) was measured on the whole ore sample (all size fractions) by the Leco analysis method. TOC represents only part of the carbon in organic matter, so an estimate was made of the total organic matter in the samples from thermogravimetric analysis (TGA) and elemental analysis (EA) of the extracted organic matter (OM). OM was extracted from the sample by stirring a pulverized ore sub-sample in 1M NaOH, then centrifuging the slurry. The solids formed a sediment, while the OM-rich supernatant remained. Acidifying the suspension to pH < 2 with HCl caused the OM to flocculate, which permitted the recovery of OM by filtration and washing.

A.2.2 Image acquisition

A micro-computed tomography scanner (SCANCO $\mu CT100$, Switzerland) was used to record volumetric images with 5 μm voxel size, at 90 kVp and 200 μA with a 0.5 mm Al filter, over an approximately 2 mm height and a 10 mm x 10 mm horizontal field of view. The raw data was

obtained as scaled linear attenuation values in the 16-bit signed integer format. Samples measured with CT included: (1) the five particle samples; (2) hydroxyapatite and quartz crystal calibration specimens (Ward's Scientific); and (3) a hydroxyapatite calibration carousel with hydroxyapatite concentration between 0 and 0.8 g of apatite per cm^{-3} (HA-SCANCO).

After CT scanning, the samples were prepared for SEM imaging by polishing the sample to the mid-point of region scanned by CT. SEM backscatter electron (BSE) images were acquired at 0.5 μm resolution over the horizontal cross-section of the particles using an FEI Quanta 650 with large area energy dispersive X-ray (EDX). Elemental maps were recorded for Ca, Mg, Fe, O, Al, K, Si, Na, Ti, P, and F.

A.2.3 Image registration

Image registration is the sequence of image transformations (such as scaling, translation, rotation) required to align a target and source image. Here, the target image, I_T, was a sub-region selected from the SEM image, and the CT image was defined as the source image, I_S. Registration requires the successive interpolation of 2D images from I_S until a match with I_T is obtained. This is achieved by defining a set of indices, X, in the image space of I_S, then applying an affine transform, M, to obtain the interpolation indices, $X' = M(v)X$, where v represents the translation (t_x,t_y,t_z) and rotation (θ_x, θ_y, θ_z) about the $x-$, $y-$ and $z-$ axes. A simple depiction of this process is shown in Figure A.2. A manual pre-alignment was conducted to estimate θ_z, t_x, t_y,and t_z. Then, a user-guided alignment was carried out using a graphical user interface (to monitor image similarity statistics) to refine the parameters of v. Last, a grid-based search of the local parameter space was conducted to determine the optimal values of v.

A.2.4 Pre-alignment

The pre-alignment permitted an approximate match between I_T and I_S. The SEM image resolution was decreased from the 0.5 to 5 μm (scaling operation), which is the same resolution as the CT images, so a pixel-to-voxel comparison could be made. A 150 x 150 pixel region of interest was identified in the SEM image and set as the target image, I_T. Individual slices of I_S (i.e. the CT

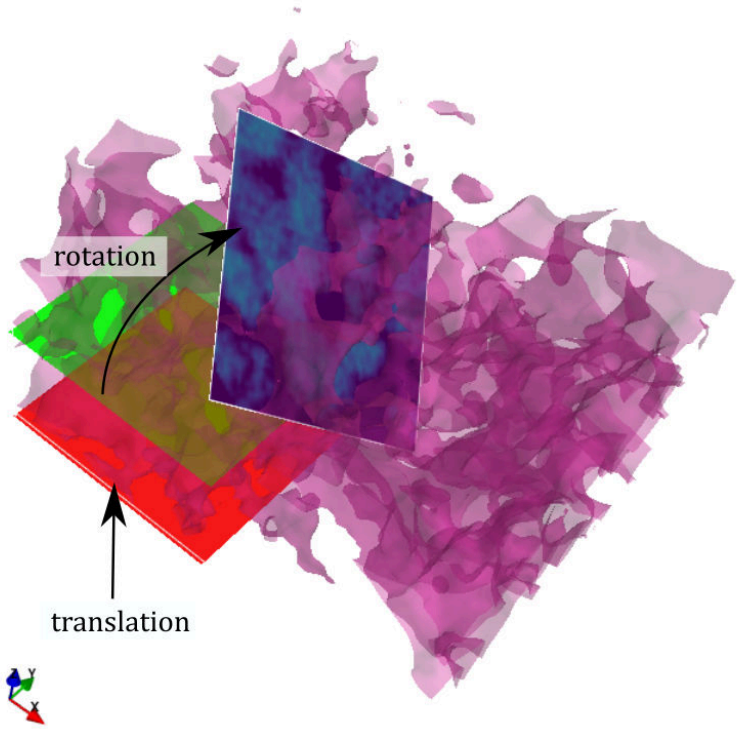

Figure A.2: Illustration of the translation and rotation of a plane in 3D.

z-stack) were visually inspected and compared with I_T. A rotation around the z-axis of I_S was applied so that the axial fiducials (PE tubes) in I_S and I_T had a similar orientation. The point in I_S that corresponded to the approximate centre of I_T was recorded, which concluded the pre-registration stage.

A.2.5 Image optimization

In the user-guided and grid registration steps, the objective was to refine the parameters of v such that $I_S(M(v))$ and I_T were aligned (Klein et al., 2010). The optimal alignment was achieved when the cost function, $C(M; I_T, I_S)$, was maximized, which was defined as the sum of two statistical properties of the images, I_T and $I_S(M(v))$: the mean structural image similarity error (MSSE), and the binary image fraction error (BFE). The method for calculating MSSE, a composite image distance measure based on the multiplication of the mean, standard deviation, and correlation coefficient of the image, has been described thoroughly in the literature (Zhou Wang et al., 2004;

Palubinskas, 2017).

BFE was calculated on the binary images of I_T and I_S, B_T and B_S. In a strict sense, the threshold value used to produce the binary images is also a parameter of C for the BFE metric. BFE was calculated as the sum of the intersection of B_T and B_S, $H = B_T \cap B_S$, divided by the sum of B_T,

$$BFE = \frac{\sum_{i=0}^{n} H(i)}{\sum_{i=0}^{n} B_T(i)}, \tag{A.2}$$

where i is the linear pixel index, used in place of referring to the (x,y) position of each pixel.

A.2.6 CT histogram analysis

Two parameters are determined with the linear attenuation histograms of the particles: the volume fraction of the phosphorous rich (P-rich) phase, φ_P, and the apatite concentration in the P-rich phase, C_A.

To estimate the volume fraction occupied by the P-rich phase, φ_P, the CT linear attenuation histograms were fitted with a mixture of Gaussian distributions, $f(x)$, which can be calculated according to:

$$f(x) = \sum_{i=1}^{n} \varphi_i p(x; \mu_i, \sigma_i), \tag{A.3}$$

where φ_i is the fractional weighting of probability distribution i, x is the histogram bin center [cm^{-1}], p is the Gaussian probability distribution function, μ_i is the distribution mean [cm^{-1}], and σ is the standard deviation. The initial estimate of the μ value of the peak that corresponds to the P-rich phase in the CT image, μ_P, was obtained during the image registration step, when the linear attenuation values of the P-rich phase were recorded for each particle. In a volumetric image, the weighting coefficient, φ_i is equivalent to the partial volume fraction of phase i in the image volume because each voxel, or volume element, represents a finite volume in the image. The μ_P value was then converted to C_A by the application of the calibration measured from the hydroxyapatite (HA)

carousel.

A.3 Results & Discussion

Accurate alignment of the CT and SEM-EDX image sets permitted the assignment of the P-rich regions in the CT images. From that result, an estimate of φ_P from the CT image histograms could be made and the CT calibration curve for apatite concentration, C_A, could be applied. These two parameters (φ_P and C_A) describe the distribution of apatite in the sample, while the bulk mass fraction of apatite, w_A, can be estimated from φ_P and C_A using Equation A.1.

A.3.1 Apatite and organic matter

Two components of interest were apatite and organic matter. According to XRD analysis, the major minerals present in the -6.7 / +4.0 mm size fraction were (by wt. %): fluorapatite (56 % and associated with carbonates), quartz (20 %), illite (5.6 %), K-feldspar (6.8 %), and dolomite (3.9 %). These values are consistent with other samples from the Meade Peak Member of the Phosphoria Formation (Knudsen et al., 2002), where the primary phosphate mineral is carbonate-rich fluorapatite (Knudsen and Gunter, 2004).

Based on visual appearance with the unaided eye and under the microscope, the particles were blackened by a uniform covering of OM. The organic matter content in the overall ore sample was 11.6 wt. %. This was determined by dividing the total organic carbon in the samples (6.1 wt. %) by the measured carbon content of the OM, which was determined with thermogravimetric analysis (51.5 wt. %). Such an OM content is not that unusual, as phosphate in ores from the Phosphoria Region has been found to occur with organic carbon contents with an average greater than 4 wt. % and as high as 30 wt. % (Maughan, 1984). While the apatite content was 56 wt. % (equivalent to 22 wt. % P_2O_5), the XRD result by weight does not account for amorphous phases such as the organic matter present in the samples. Thus, the XRD results were re-normalized to account for the OM in the samples, which reduces the fluorapatite content to 50.9 from 56.4 wt. % (19.6 from 21.7 wt. % P_2O_5). This adjusted P_2O_5 value (19.6 %) is in better agreement with the assay of

by AES-ICP (19.4 %). This sample may still be considered a phosphorite, defined as containing between 18 and 40 wt. % P_2O_5 (Glenn et al., 1994), but the inclusion of OM causes a modest reduction in the average grade.

In Figure A.3, the SEM images of three particle cross-sections are shown. The phosphorous EDX map was overlaid on half of each cross-section (indicated by the yellow dashed line). Each region bounded by a blue rectangle in Figure A.3 has a detailed mineral map shown in Figure A.4 and is the same SEM image registered in the corresponding CT image volumes, as shown in Figure A.5. The two sub-images in Figure A.3 correspond to the markers on the main image and provide a detailed view of the P-rich phase texture. The P-rich phase in these particles corresponds well with the granular phosphorites described by McClellan and Van Kauwenbergh (1990), as "usually dominated by pellets or peloids, which are spherical to sub-spherical, silt- to pebble-sized grains consisting [mainly] of carbonate-rich fluorapatite, but often containing some admixtures of siliciclastic or carbonate debris." The P-rich phase does not appear to be uniformly distributed in the particles. An estimate of the volume fraction of the P-rich phase, φ_P, was made by dividing the fraction of pixels in the P-containing area by the total number of pixels on the particle surface in the SEM images in Figure A.3. This estimate of φ_P from the SEM images varied between 0.07 and 0.94 for the images shown in Figure A.3, while the remaining two particles had φ_P of 0.42 and 0.58. These variations in φ_P appear to be caused by differences in P-rich phase grain texture and the fraction of gangue present. The P-rich phase in sample 1 occurs as porous 20 to 200 μm sized grains in a matrix of clay and quartz, whereas the P-rich phase in sample 5 appears highly homogeneous, with fewer void areas and grains 500 to 1000 μm in size.

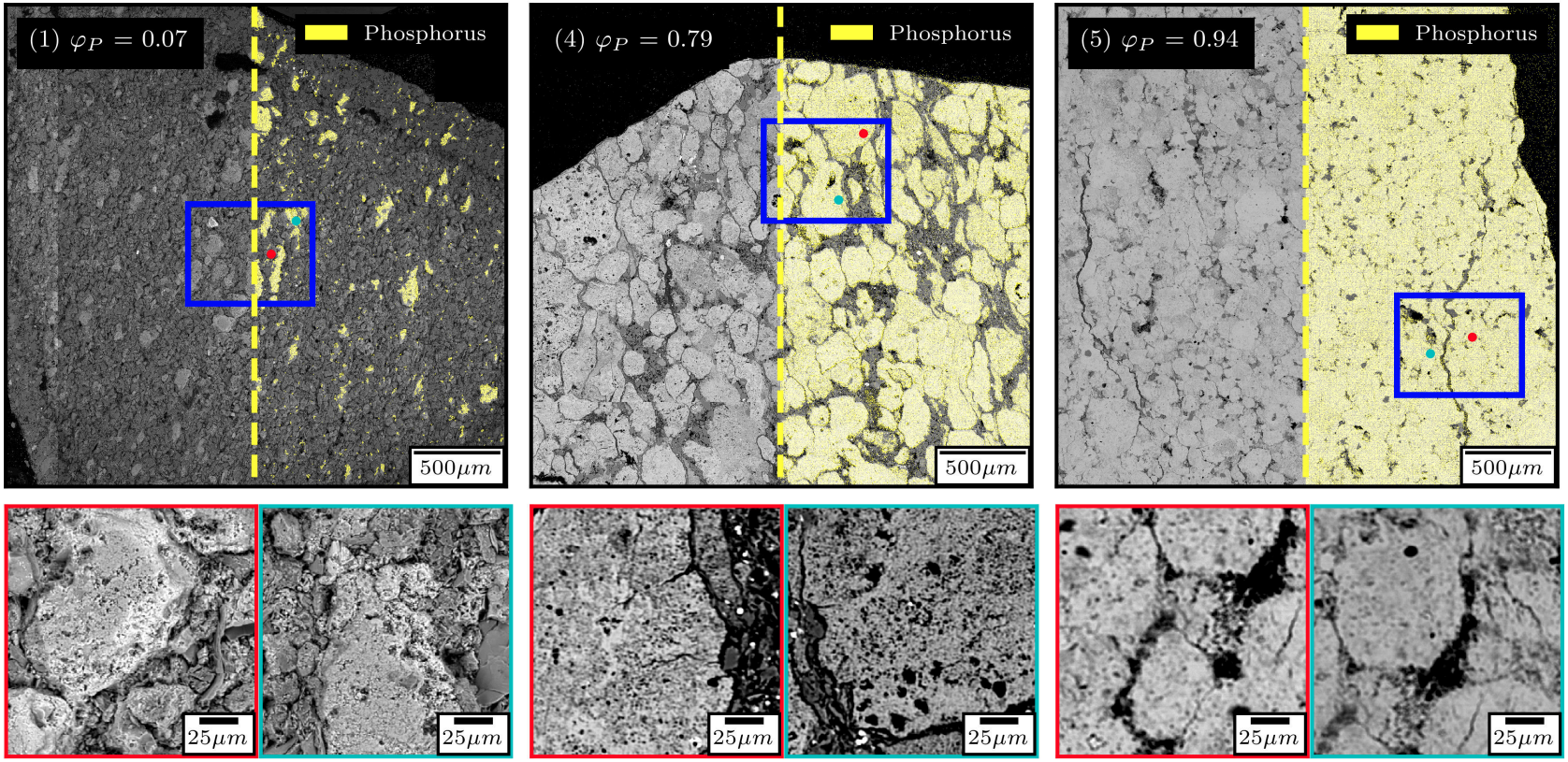

Figure A.3: Scanning electron microscopy (SEM) secondary backscatter images with elemental phosphorus (P) map overlaid on cross-sections of apatite-ore particles. The volume fraction, φ_P, of the P-rich phase was estimated from the fraction of the particle cross-section covered by P. Two sub-images at higher resolution are shown below each main image. The red- and cyan-framed sub-images correspond to the location of the red and cyan markers in the main image.

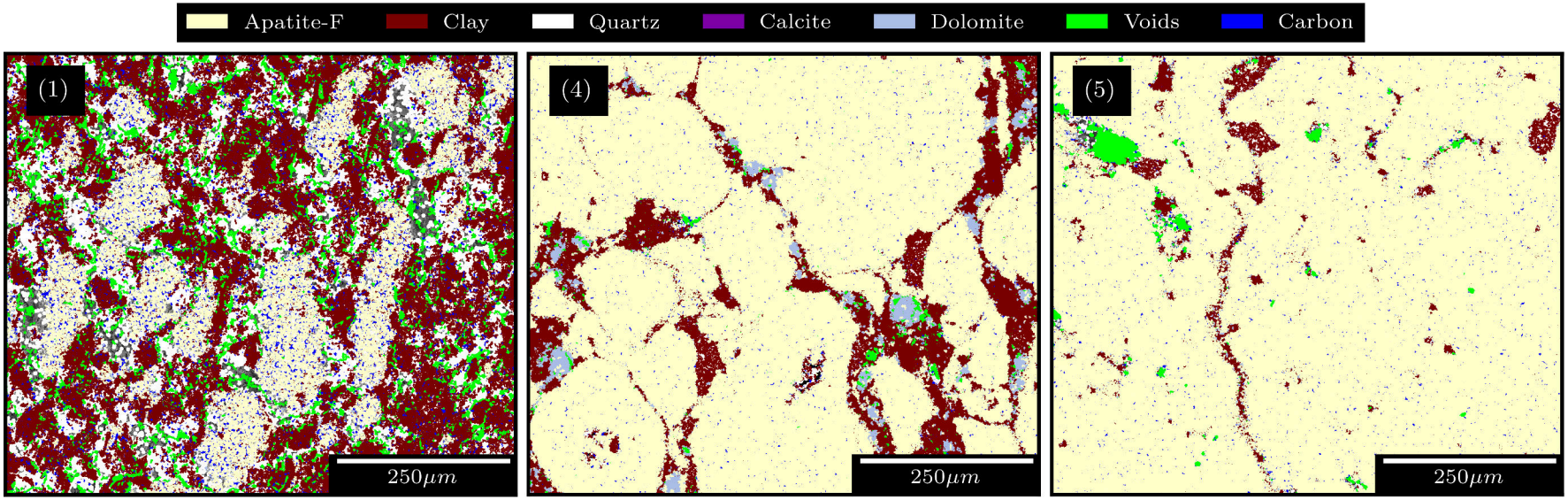

Figure A.4: Major minerals present in three representative regions of interest from scanning electron microscopy cross-sections. The numbers in the upper-left hand corner correspond to the sample number and the region of interest to the area outlined in solid blue in Figure A.3.

A.3.2 Image registration

A manual pre-registration of the CT and SEM images was conducted to estimate the initial affine transform parameters. In the five CT image volumes studied, it was possible to find an approximate match with the target SEM within about +/- 20 images (or +/- 100 μm) in the CT image stack. This step produced the initial parameters t_x, t_y, t_z, and θ_z, so the initial affine transform, M, could be estimated. Figure A.5 shows the final alignment, after user-guided and grid-search optimization, of the CT (source) and SEM (target) images for the regions outlined in Figure A.3. By visual inspection and based on the image similarity measures, the target and interpolated images in each of these sets are an excellent match. In most cases, the grid search step produced only small adjustments to the translation and rotation parameters.

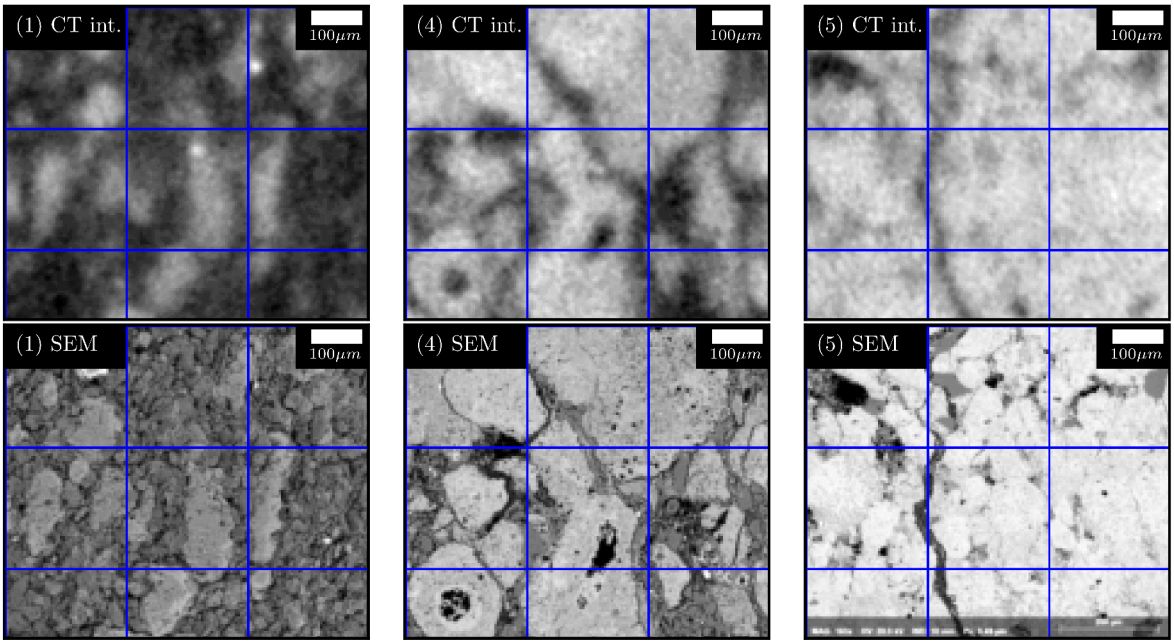

Figure A.5: Registration result for the three regions of interest highlighted in Figure A.3. The interpolated computed tomography image, CT int., and SEM image are shown for samples (1), (4) and (5).

After the best transform M was determined with the grid search, a series of images were calculated by independently modifying two of the six transform parameters to permit an observation of the signal response of the similarity statistics (BFE and MSSE) and cost function (C) for three of the samples. In Figure A.6, the effect of rotation around the $z-$axis, +/- 40 degrees or translation

in the $x-$direction, +/- 1000 μm , away from the best match, is shown. The choice to these vary parameters for demonstration purposes was arbitrary and any of the other parameters, t_y, t_z, θ_x or θ_z, could have been chosen.

The vertical line plotted in Figure A.6 shows the optimal value of the cost function, C, where the addition the of the MSSE and BFE values was maximized. An ideal similarity metric would have a very high (or low) value for a poor match, and gradually decrease (or increase) as the similarity between the interpolated and target images increased. In this case, an increase in BFE or MSSE was generally an indication of increased statistical similarity; although, this did not always equate with perceptual similarity (as judged by the unaided eye). For example, BFE contained noise, where the signal increase and decrease for small changes in t_x were not consistent with the perceived similarity. Also, MSSE was generally decreasing during convergence of the t_x parameter for Sample 1, which indicates a worse match, up to a relatively close position, at about 50 μm, then rapidly increases to the global maximum. Otherwise in samples 4 and 5, the response of BFE and MSSE generally had a well-defined symmetric shape. This observation of the BFE and MSSE signal response is a basic validation of the cost function chosen: local noise or changes in a single parameter would have led to a matching error, but the combination of signal values smooths the response and increases the likelihood of achieving the highest quality match.

The grid optimization step was useful to confirm and refine the user-guided result, but did not replace visual inspection by the user. As noted by Ye and Shan (2014), partially- or fully-automated systems are conceivable, but are more likely to result in matching errors unless a manual pre-registration step is conducted by the user. For the current study, the image registration strategy was able to find the optimal match between the CT and SEM datasets, which permitted the onward application of chemical data to the CT images.

A.3.3 Mapping the P-rich phase labels to CT

In Figure A.7, the μ histogram from the CT scan of each particle is shown. These histograms correspond to the entire volume scanned, which includes the P-rich phase and all other components

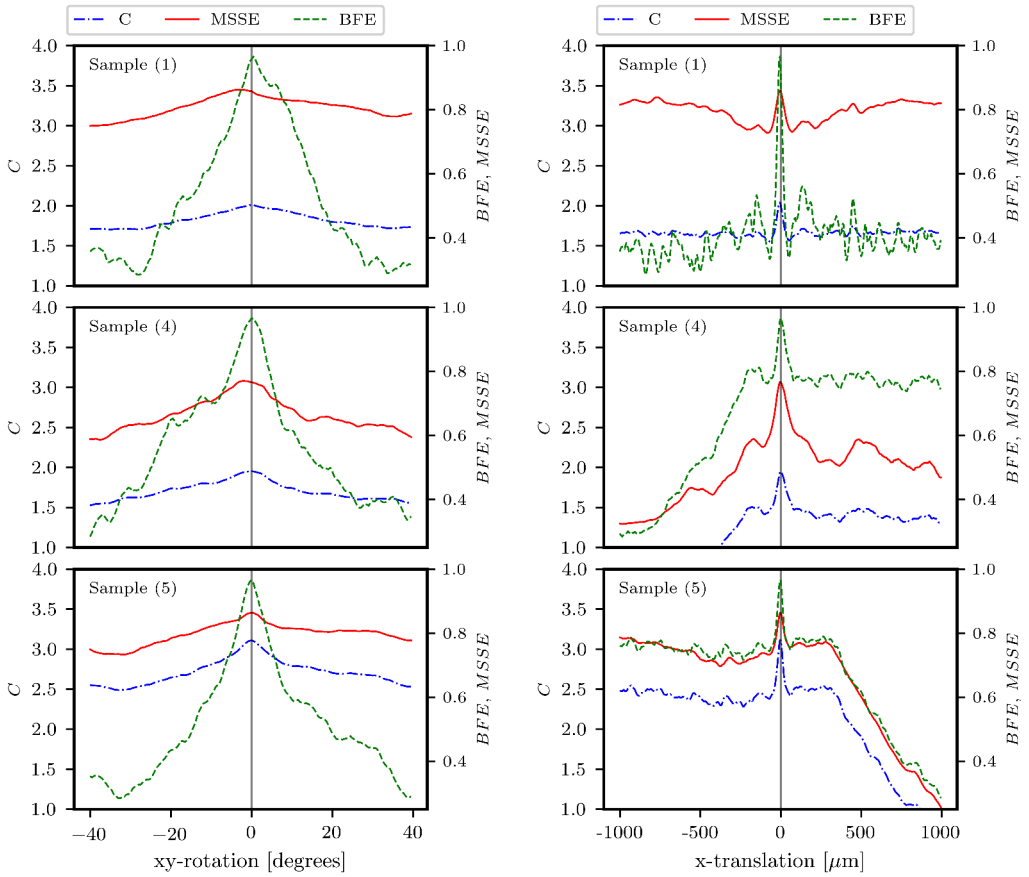

Figure A.6: Image similarity statistics (binary fraction error, BFE, and mean structural similarity error, MSSE) and cost function (C) are shown as a function of the change from the ideal transform along the z-rotation and x-translation axes. The three regions of interest for samples (1), (4) and (5) correspond to the regions identified in Figure A.3.

of the sample. Image registration permits the extraction of μ values that corresponded to the P-rich region of the sample. This was achieved by using the indices of the binary phosphorus elemental map of the registered SEM-EDX image to extract the μ values at the corresponding location in the CT image. The array of μ values corresponding to the P-rich phase of each sample are plotted as histograms in Figure A.8. The mean μ (5.02 cm^{-1}) of the pure apatite crystal was added as a reference.

In these samples, the linear attenuation of the P-rich phase, μ_P, was much lower than the mean μ (5.02 cm^{-1}) value of the pure apatite crystal. This is an indication that, although the P-rich regions contained apatite, the apatite was mixed with lower attenuation material on the sub-voxel

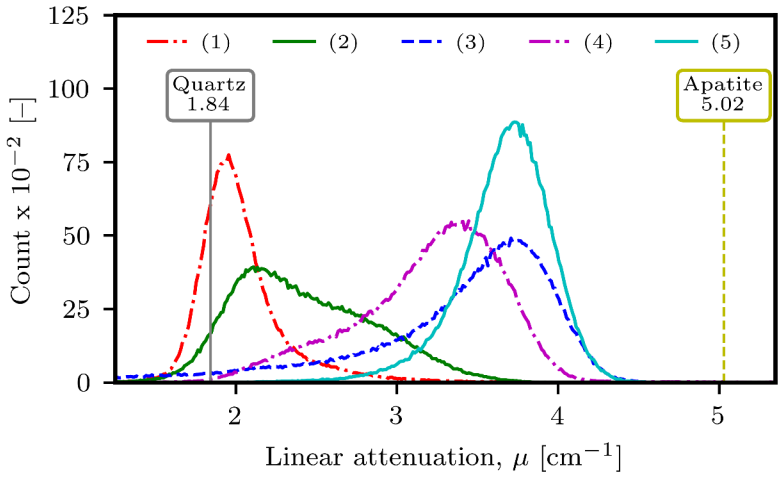

Figure A.7: Linear attenuation (μ) histograms of the CT image volumes of five-apatite containing ore particles. The mean μ value of the quartz and apatite standards are indicated at 1.84 and 5.02 cm^{-1}, respectively.

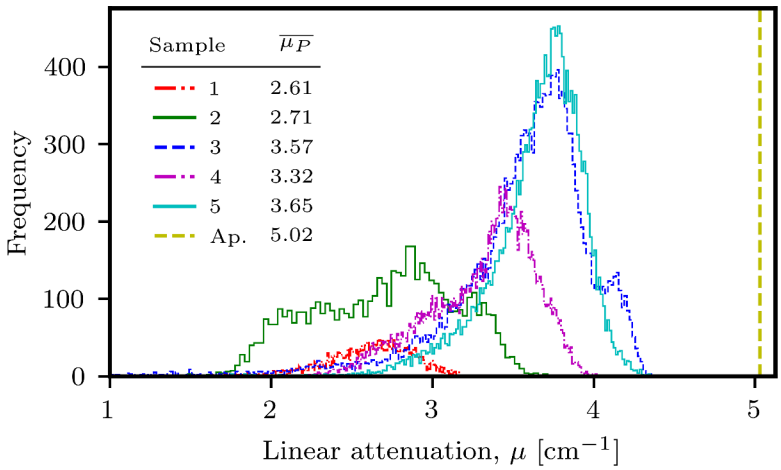

Figure A.8: Histograms of the linear attenuation values associated with the P-rich phase in the interpolated computed tomography images

scale. By the partial volume effect, the proportion and type of lower attenuation material present (gangue, pores, OM) would shift the μ values associated with the P-rich phase to lower attenuation values.

A.3.4 Apatite distribution

Two features apparent from Figure A.8 are that the total number of voxels (integral of frequency histogram) of P-rich phase varies and so does the average μ value range. In the next two sub-sections, A.3.4 and A.3.5, these features of the P-phase histograms (i.e. phase peak height and location) are related to the P-phase volume fraction (φ_P) and concentration of apatite (C_A). In this way, a statement about the quantity (φ_P) and quality (C_A) of the P-rich phase in each sample can be made.

Volume fraction

The histograms in Figure A.7 were fitted with two Gaussian distributions to determine the volume fraction of the P-rich phase, φ_P, and gangue phase, φ_g, in each sample. The mean μ-values of the P-rich phase, μ_P, tabulated in Figure A.8, were used as the initial estimate of the Gaussian distribution fit to the higher attenuation phase in each histogram. The fitting results are shown in Figure A.9. The phase weights, φ_P and φ_g, also represent the volume fraction of each phase. The higher attenuation peak in each histogram corresponds to the P-rich phase, with parameters φ_P and μ_P. An excellent fit of $\varphi_P + \varphi_g$ to the raw histograms was observed in all samples, except sample 3 where a slight deviation below 2 cm^{-1} was observed.

Sub-figures (1), (4) and (5) in Figure A.9 correspond to the samples shown in Figure A.3 and A.4. The φ_P trend (from 0.0.07 to 0.94) in Figure A.3 follows the trend in φ_P from histogram deconvolution (from 0.28 to 0.72) in Figure A.9, although the values are not equal. It is likely that the values from histogram deconvolution are closer to the actual φ_P in the samples, because the CT measurement was obtained over a layer 2 mm thick in the 4 - 6 mm sized particles, whereas the SEM fraction estimate of φ_P was localized to a nearly planar volume within the particle.

Apatite concentration

The apatite concentration, C_A, in the P-rich phase of each sample was assessed by the application of the apatite CT calibration curve, shown in Figure A.10, to the voxels in the P-rich region of each sample. This approach to applying a hydroxyapatite calibration to a sample containing fluorapatite

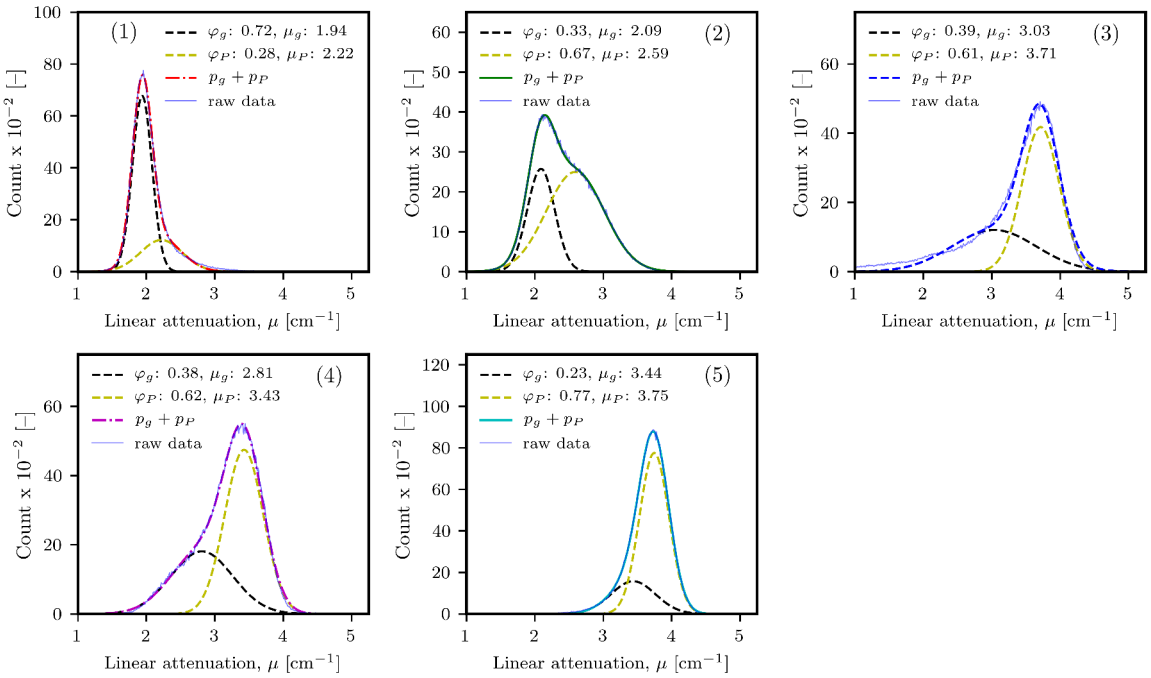

Figure A.9: Histogram deconvolution results for five apatite-containing ore particles. Sample numbering (1) to (5) is consistent with other figures and tables in this section. The combined histogram $p_g + p_P$ was fitted with two Gaussian distributions with weighting or volume fraction parameter, φ_g or φ_P, and mean linear attenuation, μ_g or μ_P.

was considered reasonable because the theoretical values, from the NIST XCOM cross-section database tool, for hydroxyapatite and fluorapatite agree within 0.1 % at 30 keV.

Calibration standards were composed of a mixture of synthetic hydroxyapatite (HA) and epoxy resin (ER), with between 0 and 0.8 g of apatite per cm^3. A pure apatite crystal was measured to extend the calibration range to 3.2 g of apatite per cm^3, or volume fraction of apatite equal to one, $\varphi_P = 1$. Ideally the calibration samples would be evenly spaced from 0 to 5 cm^{-1}, but they are clustered below 2 cm^{-1} with one point at 5.02 cm^{-1}. Nonetheless, the calibration fit quality was excellent, with a mean-square-error of 1 x 10^{-4} g apatite per cm^3 and a coefficient of correlation, $R^2 > 0.999$.

The hydroxyapatite-epoxy resin calibration system is a reasonable approximation of the heterogeneous composition of the apatite phase in the particles in this study. Gulbrandsen and Krier (1980) calculated the bulk porosity of ore samples from the Conda Region of the Phoshoria Com-

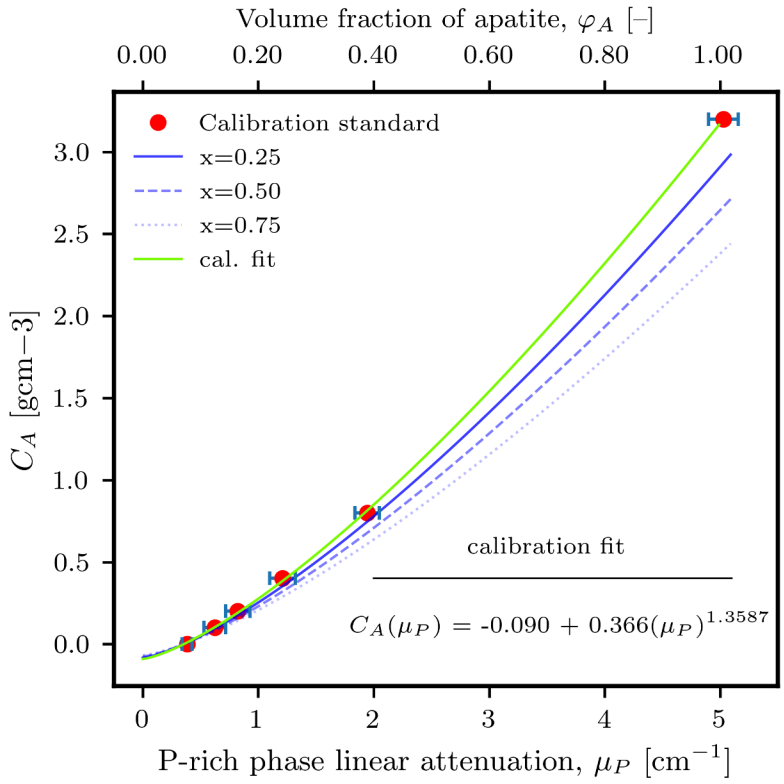

Figure A.10: Calibration curve for CT linear attenuation versus hydroxyapatite content using a series of standards of mixed synthetic hydroxyapatite and epoxy resin. The data point at φ_P = 1 corresponds to the apatite crystal. The theoretical effect of carbonate substitution level (between x= 0 and 0.75) is shown (refer to Section A.3.5

plex at 4.4 vol. % and demonstrated that a complete removal of OM and carbonates would create a rock porosity of 35 vol. %. In Figure A.3, in the higher resolution images, the apatite phase of sample (5) appears to be much more homogeneous, with fewer voids or pores, than either sample (1) or (2); while in Figure A.4, sample (1) appears to have more carbon and voids interspersed in the apatite phase. Based on the large amount of OM (11.6 wt. %) present in the samples, it is likely that the pores are at least partially filled with OM. The P-rich phase of the lower grade samples seems to have a higher porosity, e.g. sample (1) in Figure A.4, and seems to be associated with a greater amount of carbon, which indicates that the pores contain OM. Thus, it is a reasonable suggestion that the P-rich phase in these samples is comprised mainly of a porous fluorapatite and OM. One drawback of the hydroxyapatite-epoxy resin calibration standards is that the epoxy mass

density (1.2 g/cm^3) was lower than the OM mass density of Gulbrandsen and Krier (1980) (1.5 g/cm^3), which would cause the apatite grade of the particle to be slightly over-estimated.

That there were no voxels with μ values close to the pure apatite crystal (5.02 cm^{-1}) indicates the presence of sub-voxel sized inclusions of lower attenuation, including OM-filled pores and likely voids. Equation 2.9 implies that the linear attenuation of each voxel in a CT image is proportional to the weighted sum of the linear attenuation values of the component materials. This is referred to as the partial volume effect, which causes voxels measured at the edge of a feature, between two phases, and those centred on a heterogeneous medium to have an intermediate linear attenuation value (Wildenschild and Sheppard, 2013). For this reason, the resolution (5 μm) used in this study is probably lower than the resolution required to delineate all of the features present in the P-rich phase, but it is a sufficient resolution for the application of the hydroxyapatite calibration curve because the P-rich phase can be separated reasonably well with histogram fitting.

A.3.5 Effect of carbonate substitution

Carbonate-rich fluorapatite occurs throughout the Meade Peak member of the Phosphoria Rock Complex. Carbonate substitution may also be associated with higher levels of calcium (Ca) which is a concern because the ratio of Ca/P must be below 1.6 for the ore to be commercially viable. Carbonate substitution lowers C_A, but will not have a significant impact on the measured μ_P values because of the similar X-ray scattering cross-sections of CO_3^{2-} and PO_4^{3-}. A correction to the calibration function shown in Figure A.10 can be applied if the carbonate content is known. In sedimentary apatites, substitution of $CO_3^{2-} + F^-$ for PO_4^{3-} occurs on a 1:1 basis in the structure of fluorapatite, from 0 to about 25 % of phosphate sites (Knudsen et al., 2002; McClellan and Van Kauwenbergh, 1990). The maximum degree of carbonate substitution is limited to about 6 wt. % CO_3, otherwise the apatite crystal structure will be disrupted (McArthur, 1985). Substitution can be accounted for by the following formula (Wopenka and Pasteris, 2005):

$$Ca_{10-x}[(PO_4)_{6-2x}(CO_3)_{2x}]F_2, \tag{A.4}$$

where values of x range from 0 to 0.75 for samples from the Phosphoria Rock Complex.

In Figure A.11, calculated μ values for apatite and quartz are plotted as a function of incident X-ray energy. These values were calculated using the XCOM cross-section database tool and the procedure described by Mulder et al. (2004) to estimate the effective incident energy of the micro-CT X-ray beam. For substitution x values between 0 and 1, μ values decrease from 5.07 to 4.95 cm^{-1}, which implies that the X-ray scattering cross-section of the substituted and un-substituted mineral are similar for values of x between 0 and 1. This indicates that the CT calibration for apatite concentration described above does not discriminate between samples of differing CO_3^{2-} substitution. In this case, a correction to the calibration curve, $C_A(\mu_P)$, can be made by multiplying the initial result from Figure A.10 by the ratio of P (6) in the perfect apatite, to P in the substituted apatite, 6 - 2x, which is equivalent to $C_A(\mu_P)\left(1-\frac{x}{3}\right)$.

For the present samples, the amount of carbonate substitution was not measured, but a simple example can be given to demonstrate the estimated effect of carbonate content correction if the carbonate content in the sample is known. If x=0.75 and C_A=2, the corrected C_A values is $2(1-\frac{0.75}{3}) = 1.5$, which is a 25% change in the apatite concentration. In Figure A.10, the estimated effect of carbonate substitution extent on the C_A calibration is shown for x=0.25, 0.5 and 0.75.

Apatite grade

The technique presented here is able to differentiate between particles with a small amount (φ_P) of low-grade apatite (C_A) (e.g. sample 1); and samples with a larger φ_P and C_A (e.g. samples 4 and 5). The bulk apatite weight fraction in each particle, w_A, was calculated from φ_P and C_A with Equation A.1 and summarized in Table A.1. The mass density of the particles, ρ, was set to 2.5 g/cm^3, in agreement with the range reported for samples taken from several underground sections of the Meade Peak member, which were between 2.48 and 2.57 g/cm^3 (Gulbrandsen and Krier, 1980). The P_2O_5 content ($w_{P_2O_5} = w_A/2.6$) also varies significantly between particles in Table A.1, from 4 to 40 wt. % P_2O_5. The average grade of the complete - 6.7 /+ 4 mm size fraction, was 51 wt. % fluorapatite, or 20 % P_2O_5.

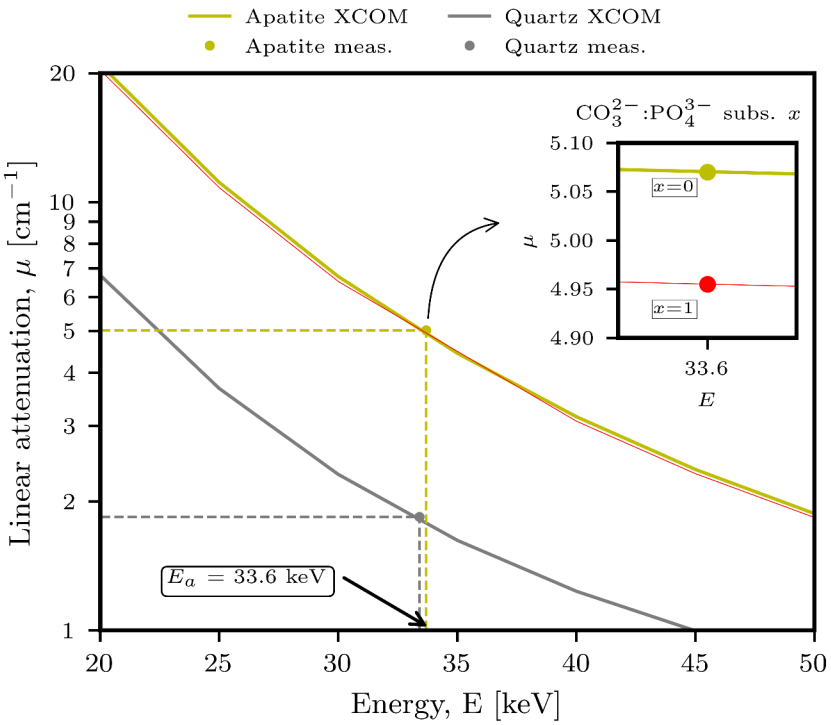

Figure A.11: Calculated linear attenuation values for fluorapatite, quartz, and carbonate-fluorapatite at various levels of CO_3^{2-}:PO_4^{3-} substitution. Calculated apparent micro-CT energy, E_a, was determined from the linear attenuation values measured for a quartz and apatite crystal.

Table A.1: Apatite and P_2O_5 grade for particles analyzed in this study. The values for the pure apatite crystal (Ap.) are given for reference

Sample	μ_P [cm^{-1}] (Figure A.9)	φ_P [–] (Figure A.9)	C_A [g/cm^3] (Figure A.10)	w_A [wt. %] (Equation A.1))	$w_{P_2O_5}$ [wt. %]
1	2.22	0.28	0.99	11	4
2	2.59	0.67	1.25	33	13
3	3.71	0.61	2.09	51	19
4	3.43	0.62	1.86	46	18
5	3.75	0.77	2.11	65	25
Ap.	5.02	1.00	3.20	100	39

The apatite grade of individual particles was between 11.1 and 65.1 wt. %, which indicates that the average head grade of 50.9 wt. % apatite, or 19.6 wt. % P_2O_5 (of the -6.7/+4.0mm size fraction) represented a mixture of particles that contain a smaller φ_P and low C_A and particles that contain a higher φ_P and high C_A. The P-rich phase was estimated to occupy between 30 and 80 % by volume of the particles and the apatite concentration, C_A, of this P-rich phase varied between 1

and > 2 g of apatite per cm^3. Taking the average grade of these five particles (41 wt. % apatite or 16 wt. % P_2O_5) results in an under-estimate of the bulk value for the -6.7/+4.0mm size fraction (51 wt. % apatite, or 20 wt. % P_2O_5). Nonetheless, it is a reasonable, but cautious result, considering that only five particles were selected and that synthetic calibration standards were used to derive this result. Perhaps in a later study a greater number of particles or improved calibration standards would refine the grade estimate obtained by XRD and AES-ICP.

The results indicate that a significant variation in apatite grade exists between and within particles. This suggests that process strategies that target the selective removal of low grade (or barren) particles could be beneficial, especially if that step is conducted prior to crushing and grinding to avoid unnecessary dilution of the higher grade apatite particles.

A.4 Conclusion

It is a matter of convenience that the components of some systems can be differentiated based on a strong contrast in μ values. For example, at 30 keV, the μ/ρ contrast between cortical bone tissue (1.33 cm^2/g) and soft tissue (0.38 cm^2/g) allows the summary identification of bone from tissue in CT images. The very high attenuation of gold (27.5 cm^2/g) means that even sub-image resolution sized gold particles may be identifiable against siliceous mineral matrices as bright spots on a CT image or as a spike of high intensity values on the μ histogram. However, if the distinction between phases in the image or histogram is ambiguous or less clear than desired, it is necessary to correlate the CT data with an external measurement to confidently categorize the intensity range of the components of interest.

The two-step image registration and calibration approach described here was necessary to explicitly identify the apatite containing phase in low-grade phosphate particles and then to assess its concentration. This permitted the expression of apatite content in terms of the volume fraction (φ_P) and concentration (C_A) of the apatite-containing phase, respectively. This approach also permitted linking the X-ray CT values to the apatite fraction, w_A. The histogram-fitting results, using initial parameters based on the mean μ_P-values of the registered P-rich phase, indicate that it is a

reasonable approximation to treat these particles as a binary mixture of a P-rich phase and gangue phase.

The 3D distribution of apatite into granular, P-rich structures of varying size, porosity, and apatite concentration, could only be completely assessed with calibrated CT images. These results indicate that process development for this ore could focus on the selective removal of low-grade ore particles, or pre-concentration of the ore by an X-ray based sorting system, before the material enters the comminution circuit. That would require linking the average apatite grade of the particles to X-ray point or line measurements from an industrial scanner. Otherwise, the combined CT-SEM correlation and calibration workflow may be considered a lab scale tool to understand the link between the X-ray attenuation signal with the quantity and quality of a mineral at coarse particle sizes. Further study, with a larger number of particles, perhaps with improved calibration samples, and the direct measurement of carbonate content, is conceivable.

Appendix B

Introduction to X-ray CT image analysis pipelines

It is a challenge to begin learning how to do quantitative image analysis. Several fundamental analytical and computer programming skills are required to load, handle, and apply existing analysis algorithms to images. Still, other skills, including how to setup a development environment and the use of software package managers, are outside the scope of this chapter. The purpose here is to familiarize the reader with the typical processing steps required to conduct analyses similar to those reported in the body of this thesis. An understanding of image indexing and commonly used image transforms provide the basic skills required to form the inputs of more advanced transformations including segmentation. In most cases, an intuitive understanding of the principles can be obtained through experimentation with sample images inside an image processing software or interactive programming shell.

Sub-sections B.2 to B.3.2 include the functions required to create simple image processing pipelines. The scripts assume the user has setup a Python environment and has installed the NumPy (numpy) Sci-Kit Image (skimage), Matplotlib (matplotlib), and numpy-stl packages via a package manager such as pip or conda. It was preferred to illustrate the implementation of simple functions based on openly available source code, even at the risk that the explicit function calls provided

may be deprecated when the software is updated. Note that the Python programming language is only used by way of example, and that similar functions are available in Matlab, ImageJ, the Visualization Toolkit (VTK), OpenCV and many commercial software packages.

It may be preferable to use a processing software with a graphical user interface (GUI) for some or all steps. Notable GUI-focused image analysis software packages including ImageJ variants (Schneider et al., 2012) (eg ImageJ, ImageJ2, FIJI) and Kitware open-source products (eg 3DSlicer (Iassonov et al., 2009), ITK, and Paraview), both of which can be extended using plug-ins, permit the application of custom processing scripts, and give interactive programming shell access to the data.

Of the many information sources available on image analysis, the following textbooks were found to be quite helpful when learning about quantitative image analysis. For an understanding of the basics of sensors, optics and image formation, "Machine vision: Automated visual inspection: Theory, practice and applications" by J. Beyerer et al (Beyerer et al., 2015) was quite helpful. A familiarity with the concepts of mathematical morphology, a theory for the analysis of spatial structures, can be found in "Morphological Image Analysis Principles and Applications" by P. Soille (Soille, 1999). The textbook "The VTK: an object-oriented approach to 3D graphics" by Schroeder et al (Schroeder et al., 2006) was helpful for understanding how to explore, transform, and visualize 3D data.

B.1 Formation of 3D images with X-ray computed tomography

Typically, a X-ray computed tomography instruments records a sequence of 2D X-ray projections, at small angular offsets, which are then re-constructed to form a 3D image by a mathematical procedure called back-projection. Commercial instrument vendors often supply the software for re-constructing the 3D image from X-ray projections. In some cases, a trained technician will carry out this processing step. At a minimum the user should be aware of the image data type and any calibrations applied during processing. In contrast, experimental X-ray computed tomography

instruments (e.g. custom-made or synchrotron facility instruments) may require the user to conduct the reconstruction process with the help of specialized software. In both cases, the output of the reconstruction process is a set of 2D images (often called "slices") stored in a directory, which is considered the starting point of the image analysis pipelines in this chapter.

B.2 Reading and indexing a 3D image

A 3D image is a set of values with an indexing convention that dictates the arrangement of the values in 3D space. In most cases, image data are in array format and the spatial reference is inherent in the array shape. For size-calibrated images such as an X-ray CT, a spatial frame of reference is provided in the form of voxel size. For example, an image, I with isotropic linear voxel size of 5 μm (i.e. each voxel is 5 μm x 5 μm x 5 μm), and 5 x 5 x 5 voxels in size, would be 25 μm x 25 μm x 25 μm. Voxels are not always of isotropic size and this must be take into account for some image transforms, although that is beyond the scope of this chapter.

One convention of labelling the indices of an image is "row-major", shown in Table B.1, where the row index represents the y-position, the column index represents the x-position, and the plane index represents the z-position. Thus, the first element of the image at x=1, y=2, and z=3 can be accessed by indexing into I as $I[3,2,1]$; and centroid of the image is located at $I[3,3,3]$. While row-major indexing appears less intuitive than the convention $I[x,y,z]$, row-major indexing makes more efficient use of computer memory and is thus widely encountered.

Table B.1: Row-major image indexing for 2D, 2D multi-channel, and 3D images.

Image type	Coordinates
2D grayscale	[row, column]
2D multichannel	[row, column, channel]
3D grayscale	[plane, row, column]

In Figure B.1, an example script for loading and cropping a 3D image is given in the Python programming language along with the output images associated with the code. For reference, a

stack of 200 2000 x 2000 UINT16 images (8 MB each) will consume about 1.6 GB of RAM memory when loaded, whereas a stack of 2000 2500x2500 FLOAT32 images (25 MB each) will consume about 50 GB of RAM memory.

```
"""
Load a 3D image from local files, crop, then display
"""
from pathlib import Path
import numpy as np
import skimage.io as sio
import matplotlib.pyplot as plt
from matplotlib.patches import Rectangle

files = Path("sli").glob("*.png") # get filenames
img = np.stack([sio.imread(file) for file in files]) # load into 3D array
z, y0, y1, x0, x1 = 10, 500, 1200, 500, 1000  # set crop indices
img_c = img[z, y0:y1, x0:x1]                  # crop image

f, ax = plt.subplots(1,2,dpi=150, figsize=(6.5, 3.5))
ax = ax.ravel()
ax[0].imshow(img[z], cmap='gray')
patch = Rectangle((x0,y0), (x1-x0), (y1-y0), fill=False, ec='g')
ax[0].add_patch(patch)
ax[1].imshow(img_c, cmap='gray')

print(f"img shape: {img.shape}")
>> img shape: (40, 2048, 2048)
print(f"img_c shape: {img_c.shape}")
>> img_c shape: (700, 500)
```

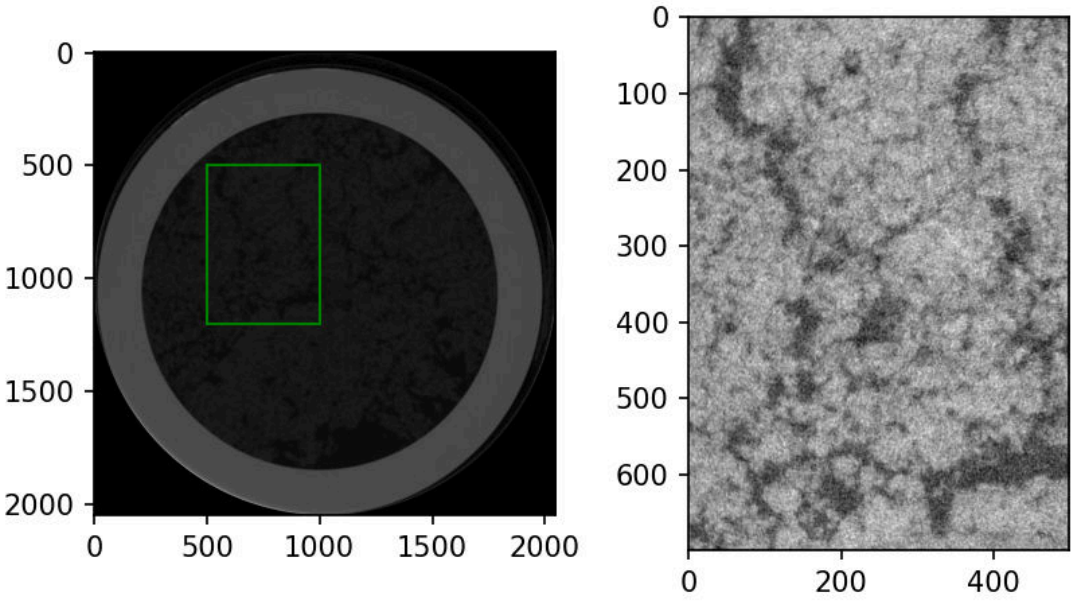

Figure B.1: Raw and cropped X-ray computed tomography images are shown to demonstrate image indexing.

B.3 Image transforms

Image transforms typically have an image as the input and an image as the output. Three types of transforms that were commonly used in the analysis pipelines in this thesis are point, statistical, and morphological operators.

Linear scaling is an example of a point operator applied on a pixel-wise basis to modify the values of an array. To calibrate CT images for mass density in Chapter 3, a calibration curve was obtained by measuring X-ray CT scans of samples of varying silica concentration in water. The calibration is applied as shown in the code excerpt in Figure B.2.

The image in Figure B.2 is still somewhat noisy image, so additional operations can be applied to improve the result. Due to the spread in grayscale intensity values recorded from water, there are some pixels with value < 1 g/cm^3, i.e. below the valid range of the calibration which is between 1 and 2.65 g/cm^3. At Line 8 and 9 of Figure B.3, the values below 1 are set to 1 (i.e. with a threshold point operator). A median filter, applied at Line 12 of Figure B.3, is an example of a statistical

operator that replaces each pixel with the median value of neighbouring pixels (a neighbourhood of 2 was used in this example). In Lines 17 to 24 of Figure B.3, a morphological operator is applied to remove small objects. This requires generating a label image (where each distinct object is assigned a unique integer value) so the algorithm can measure the size of the labels and filter out objects that are below the size cut-off criteria (a size of 9 was used in this example).

```
""" calibrate and display image """
img_md = (img_c+1702)/3501.7

f, ax = plt.subplots(1,1,dpi=150, figsize=(3.5, 3.5))
ax.imshow(img_md, cmap='viridis', vmin=1, vmax=1.5)
f.colorbar(h, ax=ax, label='Mass density $\\rho_m$')
```

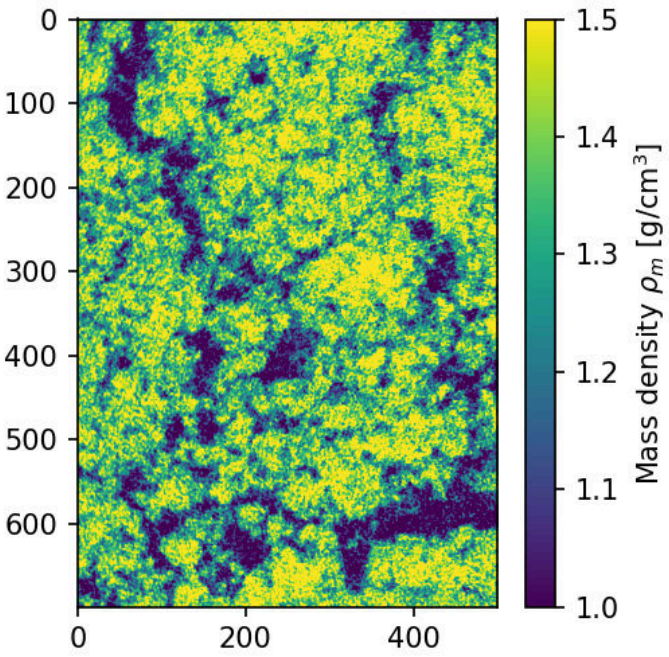

Figure B.2: X-ray computed tomography image calibrated for mass density [g/cm^3].

```
"""
mask <1, median filter, remove small objects
"""
from skimage.morphology import remove_small_objects
from skimage.filters import median
from skimage.measure import label

# ---- clip values to 1
mask = img_md < 1
img_md[mask] = 1

# ---- apply median filter
img_md = median(img_md, 2)

# ---- denoise by removing small objects
# 1 create thresholded image above 1
mask = img_md > 1
# 2 label separate componets of the mask
L = label(mask)
# 3 remove small objects and convert back to mask
L = remove_small_objects(L, 9)
mask = L > 0
# 4 set img pixels at inverse of mask to 1
img_md[np.bitwise_not(mask)] = 1 # replace
```

Figure B.3: Demonstration of image threshold, median filter, and morphological filtering of small objects to de-noise the sample X-ray computed tomography image.

B.3.1 Image segmentation

Segmentation is the process of assigning a categorical label to regions of an image. Perhaps the simplest segmentation is achieved by applying a binary threshold operator, where every pixel i of image I is converted to a pixel in image B according to:

$$B(i) = \begin{cases} 0, & I(i) > T \\ 1, & I(i) \leq T \end{cases} \tag{B.1}$$

where T is the threshold value. Similarly, multiple thresholds can be applied to the image to

produce multiple segments:

$$B(i) = \begin{cases} 0, & I(i) < T_1 \\ 1, & T_1 \geq I(i) < T_2 \\ 2, & I(i) \geq T_2 \end{cases} \tag{B.2}$$

However, this simplistic approach does not work in many cases where the image intensity histogram is non-binary, which would result in many pixels being misclassified with a single binary threshold operator. In fact, a variety of segmentation methods are available and it is often necessary to experiment to find the right one for the application at hand. In Chapter 3, it was noted that the non-finite width of of polychromatic micro-CT X-ray (i.e. higher and lower energies) causes a spread in the measured intensity values even for pure materials like water and crystalline material. This caused the intensity values of the fluid and sediment regions to overlap somewhat, which required a spatially-sensitive segmentation method to assign the pixels into each phase. There, the random walker algorithm was applied to successfully label the fluid and sediment regions of the images. In Chapter 4, a two-stage MBWT was applied to identify flocs from the background agarose gel. The first MBWT served to identify candidate regions in the images that could be flocs. That step served to reduce the image size in memory. Then a second marker-based watershed segmentation was applied to the candidate regions-of-interest using more accurate parameters based on the local intensity values of the image.

B.3.2 Surface rendering

Visualization of 3D images often requires the triangulation of a surface, or mapping some property in the image to a colormap or other representation in 3D. Perhaps the most popular method of triangulating a surface is by the Marching Cubes algorithm (Lorensen and Cline, 1987). In Figure B.4, a Python example for extracting a surface mesh from an image volume is given using the Marching Cubes implementation from Sci-Kit Image. This example includes a simplified pre-processing pipeline from loading the image to creating a mesh file in a format compatible with

many 3D viewers (stl).

```
from pathlib import Path
import numpy as np
import skimage.io as sio
from skimage.measure import marching_cubes, label
from skimage.morphology import remove_small_objects
from skimage.filters import gaussian
import stl

def triangulate_surface(img, step_size=1, isoval=0, spacing=(1,1,1)):
        """
        Extract a triangulated surface from an image using
          the marching cubes algorithm
        """
        img = np.pad(img,
                     pad_width=[[1,1],[1,1],[1,1]],
                     constant_values=0)
        verts, faces, _, _ = marching_cubes(img,
                                            isoval,
                                             step_size=step_size,
                                             spacing=spacing)
        return (verts, faces)

files = Path("sli").glob("*.png") # get filenames
img = np.stack([sio.imread(file) for file in files]) # load into 3D array
img_c = img[:, 750:1250, 750:1250] # crop
img_md = (img_c+1702)/3501.7     # calibrate
img_md[img_md<1] = 1 # clip
img_md = gaussian(img_md, 1) # denoise
# threshlold the sediment region (see above why this is less accurate.)
mask = img_md > 1.15
L = label(mask)
mask = remove_small_objects(mask, 25)
mask = mask > 0

vertices, faces = triangulate_surface(mask)

# create the mesh
mesh = stl.mesh.Mesh(np.zeros(faces.shape[0], dtype=mesh.Mesh.dtype))
for i, f in enumerate(faces):
    for j in range(3):
        mesh.vectors[i][j] = vertices[f[j],:]
mesh.save('mesh.stl') # save to stl format
```

Figure B.4: Example of a Marching Cubes function call using Sci-Kit Image marching cubes implementation and conversion to mesh format for visualization.